University of Trieste

Avalanche photodiodes for X-ray detectors based on GaAs/AlGaAs semiconductors

Tereza Steinhartová

supervisor: Dr. Giorgio Biasiol

Trieste 2019

Abstract: This thesis work is devoted to the development and performance assessment of avalanche photodiodes with separated absorption and multiplication region (SAM-APDs) based on GaAs/AlGaAs. These devices should form the basis of future fast and sensitive detectors for new generation light sources, especially then for energies at which silicon is not adequate anymore. The theoretical part (chapter 1) thoroughly explains principles of avalanche photodiodes, justifies the use of the selected materials and explains the principles and advantages of the device concept based on the separation of absorption and multiplication regions. Chapter one also introduces the staircase structure located in the multiplication region which is designed to enhance multiplication of electrons and suppress multiplication of holes. The instrumental part (chapter 2) describes in detail methods of fabrication and testing techniques used in this project, such as molecular beam epitaxy (MBE) which is used for the synthesis of the GaAs/AlGaAs multilayers and the lithographic fabrication techniques. The light sources used for the characterization of the SAM-APDs are also described in this chapter. In the third chapter the fabrication procedure which was developed to produce the SAM-APDs is described. The experimental setups which were prepared and used for testing are described too. In the fourth chapter the results of detector tests are presented and discussed. In this study, we optimized in particular the doping concentration of the p-doped separation layer between the absorption and multiplication region in order to improve device performances. We found that sub-monolayer separation layer with a planar concentration of 2.5×10^{12} cm^{-2} under a form of a delta-doped layer provides optimal device performance in terms of the charge collection and the multiplication gain. We also studied the influence of the number of steps in the staircase structure of the multiplication region. Samples with 6, 12 and 24 steps were prepared and tested. Comparison of the noise characteristics shows decrease in the noise associated with the multiplication process as the number of steps increases. An increase in the multiplication gain with the number of steps was observed as well. Time response measurement were performed using a green laser with a 10 ps-pulse-width and for the devices with 12 and 24 steps located in the multiplication region a rise time less than 100 and 80 ps was measured, respectively. Furthermore the time response experiments and the spectroscopic measurements performed under pulsed laser illumination are also alternative methods to assess the gain. The gains obtained by means of these two methods follow the trend with the number of steps observed with the noise setups, however are systematically smaller in absolute value. Finally, we tested the 12 steps device under X-ray illumination of photon energy 12.5 keV. Due to the different transmission and absorption of high energy photons and the resulting significant photon absorption also in the multiplication region, the gain under X-rays illumination appears smaller than the gain under laser illumination.

Keywords: solid state detector, avalanche photodiode, impact ionization, detector design, GaAs/AlGaAs

Abstract: Questa tesi è dedicata allo sviluppo e alla valutazione delle prestazioni di fotodiodi a valanga con regione di assorbimento e moltiplicazione separata (SAM-APD) basati su semiconduttori GaAs / AlGaAs. Questi dispositivi sono concepiti come la base per futuri rilevatori sensibili e veloci per sorgenti luminose di nuova generazione, soprattutto per energie in cui il silicio non è più adeguato. La parte teorica (capitolo 1) spiega a fondo i principi dei fotodiodi a valanga, giustifica l'uso dei materiali selezionati e spiega i principi e i vantaggi del concetto di separazione delle regioni di assorbimento e moltiplicazione nei dispositivi. Inoltre, introduce la struttura a scala nella regione di moltiplicazione, progettata per migliorare la moltiplicazione degli elettroni e sopprimere la moltiplicazione delle buche. La parte strumentale (capitolo 2) descrive in dettaglio i metodi di fabbricazione e le tecniche di test utilizzate in questo progetto, dall'epitassia a fasci molecolari (MBE) utilizzata per la sintesi dei multistrati GaAs/AlGaAs, alle tecniche di fabbricazione litografiche, fino alle sorgenti di luce usate per la caratterizzazione dei dispositivi. Net terzo capitolo è descritto il processo di fabbricazione che è stato sviluppato per produrre i SAM-APD. Sono descritte anche le configurazioni sperimentali che sono state messe a punto e utilizzate per i test. Nel quarto capitolo vengono presentati e discussi i risultati dei test dei rivelatori. In particolare, abbiamo ottimizzato il doping nello strato di separazione drogato p tra le regioni di assorbimento e moltiplicazione. Abbiamo stabilito che un drogaggio di $2.5 \times 10^{12}\,\mathrm{cm}^{-2}$ sotto forma di delta doping è quello che fornisce le prestazioni ottimali del dispositivo in termini di raccolta della carica e guadagno di moltiplicazione. In secondo luogo, abbiamo studiato l'influenza del numero di step nella struttura a scala della regione di moltiplicazione. Sono stati preparati e testati campioni con 6, 12 e 24 step. Un confronto delle caratteristiche di rumore mostra che il rumore associato al processo di moltiplicazione diminuisce all'aumentare del numero di step. Inoltre, abbiamo osservato che il guadagno della moltiplicazione aumenta con il numero di step. Sono state effettuate misure di risposta temporale utilizzando un laser verde con una larghezza di impulso di 10 ps; per dispositivi con 12 e 24 step nella regione di moltiplicazione è stato misurato un tempo di salita inferiore a 100 e 80 ps, rispettivamente. Inoltre, gli esperimenti di risposta temporale e le misure spettroscopiche eseguite sotto illuminazione laser pulsata costituiscono anche dei metodi alternativi per valutare il guadagno. I guadagni ottenuto con questi due metodi segue la stessa dipendenza dal numero di step osservata con le misure di rumore, tuttavia sono sistematicamente più bassi in valore assoluto. Infine, abbiamo testato il dispositivo a 12 step sotto illuminazione a raggi X con energia del fotone di 12,5 keV. A causa della differenza di trasmissione e assorbimento dei fotoni ad alte energie e del conseguente significativo assorbimento dei fotoni anche nella regione di moltiplicazione, il guadagno sotto l'illuminazione a raggi X risulta inferiore rispetto al guadagno sotto l'illuminazione laser.

Parole chiave: rivelatore a stato solido, fotodiodo a valanga, ionizzazione da impatto, design del rivelatore, GaAs / AlGaAs

Acknowledgement

At this place I would like to express my deep appreciation to all the people who helped me and supported me during this four years of collecting not only data but first of all priceless experiences, skills and knowledge.

First of all, a big thanks belongs to my supervisor Dr. Giorgio Biasiol who was for me a patient and kind mentor. He was always available for fruitful discussions and his advices were priceless.

I would like also to express my thanks to the whole research team collaborating in the frame of the PRIN project 2015WMZ5C8, funding this research. Namely to our collaborators from University of Udine - Alessandro Pilotto, Dr. Pierpaolo Palestri, Dr. Francesco Driussi, prof. Luca Selmi. I am glad that I had the chance to be part of such a productive and dynamic collective.

Special thanks belongs to my colleagues and friends Dr. Matias Antonelli and Camilla Nichetti who were spending their time with me improving the experimental setups and discussing the obtained results and to Dr. Simone Dal Zilio who was my teacher and guide in clean rooms.

Thanks for brilliant comments and suggestions belongs to Dr. Ralf H. Menk and to Dr. Giuseppe Cautero form the Electromagnetism group of Elettra Sincrotrone Trieste.

I would like also to thank all the people in the TASC Laboratory, CNR-IOM and Elettra Sincrotrone Trieste who were creating nice and friendly working atmosphere and especially to the laser group of Elettra who moreover kindly allowed us to perform many measurements in their laboratories. Especially to and to representative of SYRMEP beamline of Elettra Dr. Fulvia Arfelli, of laser lab of Elettra Dr. Miltcho Danailov and of BEAR beamline prof. Stefano Nannarone.

A special thanks goes to my family who is always a huge support for me.

Contents

Introduction

Single photon detectors (SPDs) represent the ultimate sensitivity limit for any quantum radiation sensors utilized in different fields of science, such as medical imaging, hazard and threat detection, (bio)-photonics, high energy and astrophysics, just to mention a few. Single-photon detection is generally achieved by means of avalanche photodiodes operating in a Geiger mode (single photon avalanche photodiodes (SPADs) or Si photomultipliers (SiPMs)). Using the devices in the Geiger mode, however, leads to high noise rates and some informations, like energy of photon, or number of photons (if multiple per cell) can not be extracted from the response. For this reason, Si avalanche photodiodes (APDs) operated in linear regime have became a field of interest and, although with some limitations, have been already successfully utilized in ultrafast experiments with X-rays generated by synchrotron radiation (SR) sources or free electron lasers (FEL's) [1, 2].

Ultra fast experiment in general focus on observation of processes of time scale down to tens of fs. Three general classes of such ultra fast experiments, which can be distinguished. The first class consists of experiments where the X-ray beam is used to probe the sample without modifying it, as done in most experiments at current synchrotron sources. In the second class, a (FEL or coherent synchrotron) X-ray beam is used to induce extremely fast non-linear photo-processes or to bring matter to extreme conditions [5]. In the third class the ultrafast nature of the FEL pulse is used to obtain a snapshot of the structure of the sample before the aftereffects of radiation damage set in [6]. These classes of experiments will govern the cutting edge of science in the next decades as the time scales are going down to time scale of the fastest vibrational periods of molecules and hence, for example, experiments complementary to the theoretical chemistry simulations will be accessible [3, 4]. However, the final success depends dramatically on the availability of new detector technologies. A continuously widening mismatch is present between the well-demonstrated ability of these sources to deliver very high photon fluxes in the sub-ps regime and the only modest abilities of fast detectors to record the results [7, 8].

These more stringent requirements put on APD detectors ask for a new choice of materials which must be able to operate in harsh environments, at high temperature and with good tolerance to radiation [10]. In consideration of these requirements $Al_xGa_{1-x}As$-based compounds have been suggested [11]. One other key points of GaAs is the higher atomic number compared to Si, which results in a general higher photon absorption compared to Si. This makes it possible to produce devices with a thinner active region and, consequently, to achieve shorter response time and better performance of the detector. Another advantage of GaAs is its relatively low electron-

hole pair creation energy 4.184 eV.

$Al_xGa_{1-x}As$ alloys have also relatively wide energy bandgap ranging from 1.42 eV (GaAs) to 2 eV ($Al_{0.45}Ga_{0.55}As$, i.e., the highest Al concentration with a direct bandgap). This makes the number of thermally generated carriers lower than that in narrow bandgap materials, resulting in a lower leakage current (noise), which allows X-rays to be detected even at room temperature [12]. Important is also the possibility to tailor the material properties, notably the bandgap at the nanoscale, which is the way to overcome the problem of the intrinsic similarity of the ionization coefficients of holes and electrons in GaAs, which leads to higher multiplication noise, as explained in first chapter.

This work focuses on the development of avalanche photodiodes with separated absorption and multiplication regions (SAM-APD) [13], based on GaAs/AlGaAs and grown by Molecular Beam Epitaxy (MBE). The first chapter explains the basic physical principles and the state of the art of silicon based APDs, followed by a detailed explanation of the advantages which are gained with the choice of AlGaAs instead of silicon. In addition, particular structures and the reason of their use are described. In the following chapter, the methods used to prepare the devices are described, starting from MBE, going through standard fabrication techniques up to methods for the characterization of the diode response. The third chapter describes the fabrication process which we developed to produce the devices and gives a detailed description of the experimental setups on which the devices were tested. In the last chapter, the experimental results focused on noise and multiplication characterization, time response, spectroscopic measurements and response to X-ray are presented.

1. Avalanche photodiodes

A special category of photodiodes, which are doped in a way that when a reverse bias is applied a region of high electric field ($> 10^5$ Vcm^{-1}) exists, is called avalanche photodiodes (APDs). APDs rely on the impact ionization and consequent avalanching of charge carriers to produce an electrical signal with a significant gain so that even very low light levels impinging on the device can be detected (see 1.1). The benefits of APDs over conventional PIN photodiodes are their high sensitivity, high speed, high gain and high signal-to-noise ratio. Thanks to their characteristics, they are widely used in optical range-finders, spatial light transmission, scintillation detectors, etc. A special application of APDs is their use as fast detectors in the X-ray range. This spectral region has become more and more relevant after the development of synchrotron radiation sources, where the single photon sensitivity and intrinsically fast response of APDs is a valuable asset [1]. Examples of their application as detectors are Mössbauer microscopy and time-resolved X-ray diffraction imaging [14].

1.1 Impact ionization

The key role in the functionality of avalanche photodiodes plays process called impact ionization: Free charge carriers (electrons and holes) are accelerated by a high electric field until they gain sufficient energy to excite an electron from the valence into the conduction band, as illustrated in fig. 1.1. As a result an electron-hole pair is created. Avalanche multiplication takes then place when carriers generated like this undergo this same event. In this way a significant current flow is established in the device from one original free carrier. The electric fields required to observe this phenomenon depend on the bandgap of the material and may range at room temperature from 10^4 Vcm^{-1} in low-bandgap semiconductors, such as InAs ($E_g = 0.33$ eV), to values well in excess of 10^5 Vcm^{-1} in wide-bandgap materials, such as GaP ($E_g = 2.24$ eV) [15]. $Al_xGa_{1-x}As$ falls into the second category with its bandgap ranging from 1.42 eV (GaAs) to 2 eV ($Al_{0.45}Ga_{0.55}As$, i.e., the highest Al concentration with a direct bandgap).

The minimum energy needed for impact ionization is the ionization threshold energy E_i. Threshold energies are important because they strongly influence the ionization coefficients for electrons and holes. These quantities, denoted by α and β, respectively, are defined as the reciprocal of the average distance, measured along the direction of the electric field, travelled by an electron or a hole to create an electron–hole pair.

Impact ionization is a three-body collision process, and the final carriers are left with finite kinetic energy and momentum. This means that in general the energy of

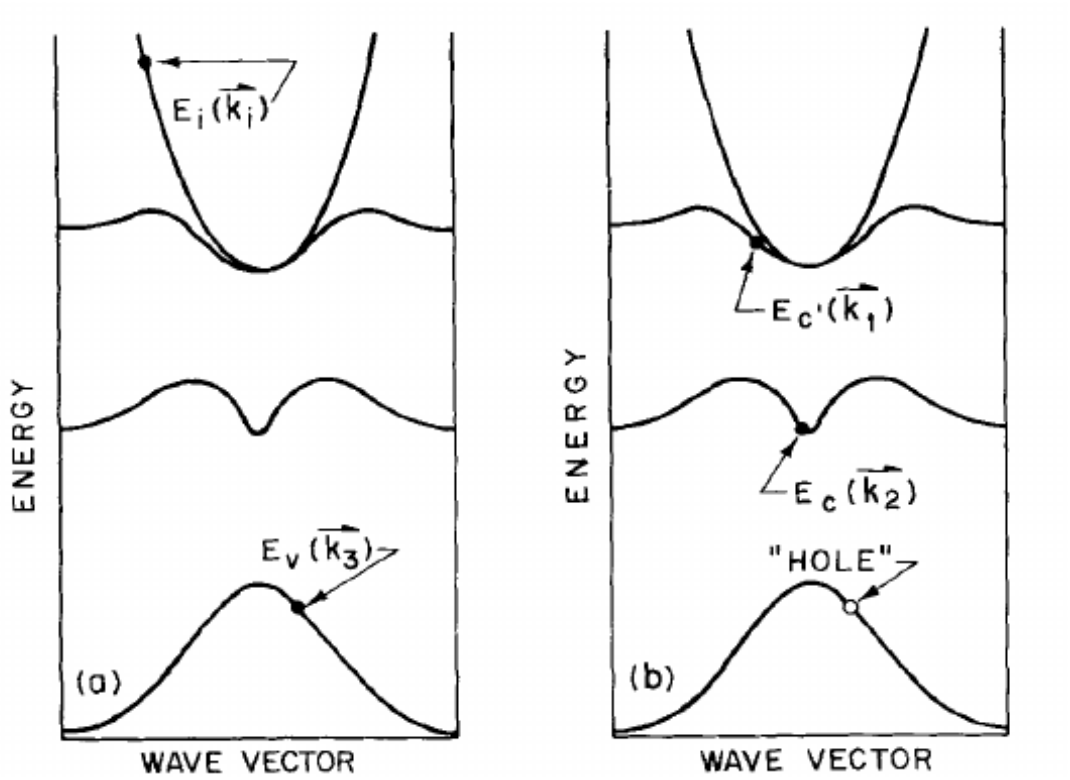

Figure 1.1: Hypothetical impact-ionization process: (a) primary particles before ionization; (b) resultant particles immediately after ionization. From [15]

the impact-ionizing carrier is greater than the bandgap. The threshold energies and consequently the ionization coefficients depend on the band structure of the semiconductor. The values of α and β, along with the length of the field region and the carrier-injection conditions, determine the magnitude of the avalanche gain and multiplication noise. Great effort has been made to develop models which predict the behaviour of these entities in various materials [16, 17]. Using GaAs as a material for avalanche multiplication we have to deal with α and β having very similar values. This leads to high multiplication noise due to strong feedback effect. One of the possible ways how to deal with this drawback of GaAs is the above-mentioned bandgap engineering. This problematic is explained in detail in section 1.4, together with particular structural features of the devices developed in this thesis.

1.2 Silicon APDs for X ray detection

APDs are typically operated in either a linear mode where the device has a well-defined moderate signal gain, or in a Geiger mode where they are biased above breakdown and a single electron leads to a run-away gain. In the short discussion in this section, where we focus on detection of X-rays, we will take into account only linear operation, as Geiger operation leads to high noise rates and is generally most inter-

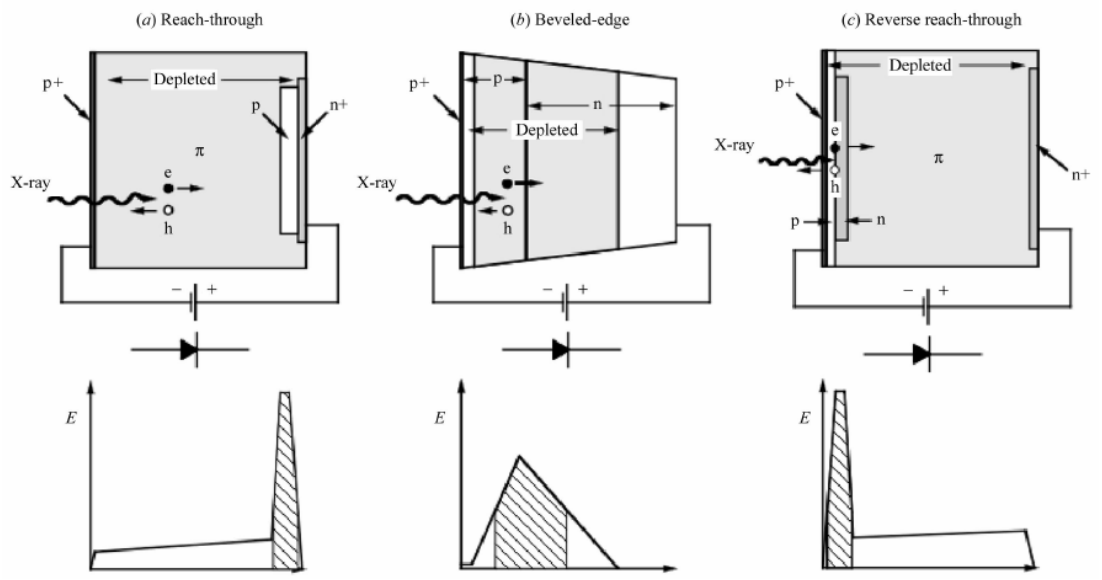

Figure 1.2: Schematic of the structure and field profile of several types of APDs. The orientations are chosen so that, under bias, free electrons will move from left to right. Hatched sections of the field profile indicate the gain region. According to the usual diode convention, the left side is the anode and the right side is the cathode, with the X-rays shown entering through the anode. Reverse biasing (shown) is achieved by applying positive HV to the cathode (right side) and holding the anode (left side) at ground.[from [1]]

esting for the detection of very-low-energy photons. Moreover, only direct detection, where the X-ray is absorbed within the silicon APD itself, is considered here.

Diagrams of several device structures are shown in fig. 1.2. The depletion layer of the device consists of a low-field (drift) region and a high-field (gain) region. For modest-energy X-rays the dominant process in Si is photoelectric absorption, typically leading to a single electron having almost the energy of the incident X-ray. This electron then quickly loses energy to scattering processes in the silicon. On average, at room temperature, one electron hole–pair will be created for each 3.6 eV of energy deposited in the silicon. These electrons drift to the gain region of the device and are amplified. It is worth noting that at higher X-ray energies an increasing fraction of the X-rays will suffer Compton scattering, which, for most geometries, will cause the photon to go out of the detector without deposition of sufficient energy for detection. Thus, direct detection in silicon devices becomes increasingly inefficient at higher X-ray energies, owing both to decreased photoelectric absorption and to increased scattering out of the APD.

Silicon APDs, with single photon sensitivity and an intrinsically fast response, are the detectors of choice in a variety of experiments. Of particular note is their extremely large dynamic range (the ratio of maximum count rate to noise rate is typically $> 10^8$, and 10^{10} is possible) and very good time resolution (ns typical, < 100 ps pos-

sible) [1]. Pulse counting in a random process is unavoidably affected by losses. In nearly all detector systems a minimum amount of time must separate two events so that they can be recorded as two separate independent events. The minimum time of separation for proper detection is usually called the deadtime (or resolving time) of the counting system. Feller [18] and Evans [19] have developed the two basic types of idealized models for deadtime, i.e., nonparalyzable and paralyzed model. The paralyzable detection system is unable to provide a second output pulse unless there is a time interval equal to at least the resolving time τ between the two successive true events. If a second event occurs before this time, then the resolving time extends by τ. Thus, the system experiences continued paralysis until an interval of at least τ lapses without a radiation event. This interval permits relaxation of the apparatus. Based on the interval distribution of radiation events, the fraction of those events which are longer than τ is given as $e^{-n\tau}$, where n is the average number of true events per unit time. Product of this fraction with the true count rate provides the observed count rate:

$$m = n \cdot e^{-n\tau} . \tag{1.1}$$

The nonparalyzable type of detector system is not affected by events which occur during its recovery time (deadtime), τ. Thus the apparatus is dead for a fixed time τ after each recorded event. If the observed counting rate is m, then the fraction of time during which the apparatus is dead is $m \cdot \tau$. And the fraction of time during which the apparatus is sensitive is $1 - m \cdot \tau$. Thus, the fraction of true number of events that can be recorded is given as,

$$\frac{m}{n} = 1 - m \cdot \tau . \tag{1.2}$$

For low count rates, both these models give virtually the same result, but their behaviour is very different at higher rates (fig. 1.3 (a)).

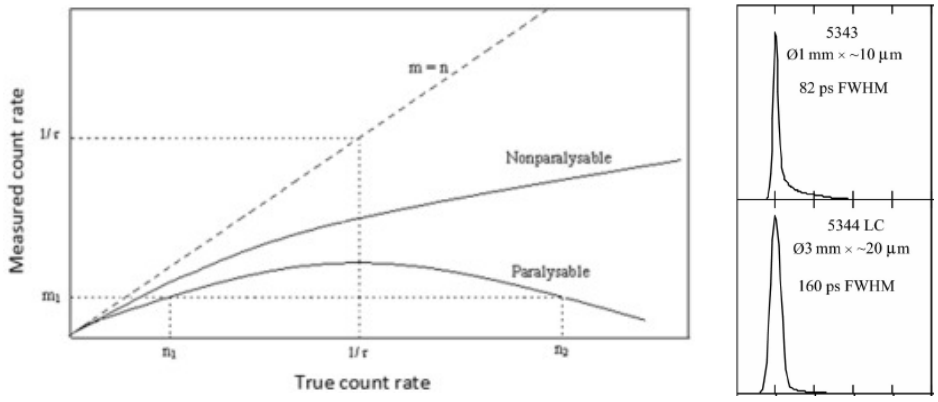

(a) (b)

Figure 1.3: (a) Illustration of the typical behaviour of measured vs. true count rate and its two possible theoretical trends (from [20]) (b) Time response of two APDs differing by area and active thickness. Full horizontal scale is 2.5 ns in each case.

Two essential parameters for describing the response of an APD to X-rays are its active thickness and its capacitance. The active thickness of the device is that part of the silicon in which X-ray absorption will lead to subsequent electron amplification. This affects both the efficiency of the device and its time resolution. Since X-rays tend to penetrate and (to a first approximation) uniformly illuminate the active thickness of Si, the time resolution is generally not better than the active thickness over the drift velocity (the high-field drift velocity in Si is about $100\,\mu m\,ns^{-1}$ [21]). This means that there is typically a trade-off between device efficiency and time resolution: for example, an APD with a 100 μm active thickness will generally not have a time resolution better than about 1 ns, while to get below 100 ps the active thickness should be 10 μm or less.

The APD capacitance, determined by the area and the thickness of the depletion region, affects both the amplitude and the width of the voltage pulse from the device. In detail, considering the APD as a parallel-plate device with constant field [22], one finds that the rise time of the voltage signal will be governed by the process of the charge transport within the device, while the fall time is not shorter than the RC time constant of the diode capacitance and the amplifier input impedance (e.g. RC = 1 ns for a 20 pF diode capacitance into 50 Ω). Meanwhile, the voltage signal amplitude scales inversely with the device capacitance, for a fixed gain, so devices with lower capacitance (smaller areas, thicker depletion regions) generally provide larger and faster signals.

Two time responses of epitaxial reach-through structure devices by Hamamatsu are shown in figure 1.3 (b) as an example. The upper one had an active thickness of only 10 μm and a time resolution of 72 ps which can be estimated from the FWHM after subtraction of source pulse width. Despite this performance was excellent, the device had relatively large capacitance, so the pulse signal was small. That led to a problem in a device having nominally the same structure but a larger area, which failed because the signal amplitude decreased so much that amplifier noise blurred the resolution to 140 ps. Thus the development of a low-capacitance version of this device was launched, where the depletion region was increased to 20 μm, which increased the overall response time and the resulting time resolution was 150 ps FWHM (the lower panel in 1.3 (b)). However, the signal-to-noise ratio was dramatically improved, and the tail of the time response behaved similarly to the original device (the upper panel in 1.3 (b)). This device, then, is especially interesting as a fast low-energy X-ray detector (low energy because it is thin) and for cases where a short time response is essential.

Table 1.1: The comparison of important properties of silicon and GaAs at RT.

Material	bandgap [eV]	atomic number	electron mobility [$cm^2/V \cdot s$]
GaAs	1.4	31(Ga), 33(As)	≤ 8500
Si	1.1	14	≤ 1400

1.3 Advantages of APDs based on GaAs/AlGaAs

In the previous section 1.2 the basic principles and advantages of silicon based APDs were explained and some limitations given mostly by intrinsic properties of silicon were mentioned. This section is focused on the limits and their possible overcoming by using GaAs as an alternative material. Table 1.1 compares bandgap, atomic number and mobility of silicon and of GaAs. These properties make GaAs the material of choice in high-energy X-ray detection if compared to silicon.

As mentioned above, direct detection in silicon devices becomes increasingly inefficient at higher X-ray energies, owing both to decreased photoelectric absorption and to increased scattering out of the APD. In this respect, the higher atomic number of the elements in GaAs alloy becomes an advantage as it provides higher absorption for energies above 11 keV. In the fig. 1.4 the transmittance T (a) and the absorption length λ (b), related together by expression $T = \exp(-\frac{x}{\lambda})$, where x is a thickness of the absorbing material, are plotted in dependence of photon energy for GaAs and Si.

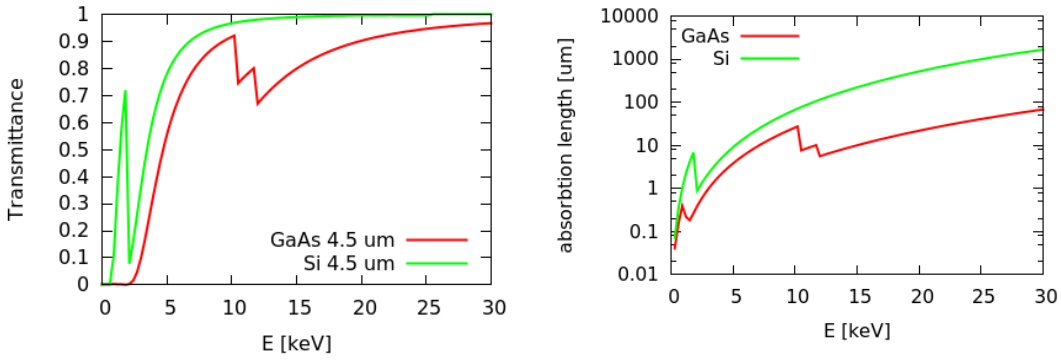

(a) (b)

Figure 1.4: Comparison of transmitance (a) and absorption length (b) of Si and GaAs as a function of the energy of the impinging photons. Data taken from [23].

The higher absorption of GaAs not only makes it possible to detect the radiation of higher energy at all, but it also brings advantages in terms of time resolution. To a first approximation X-ray radiation uniformly illuminates the active thickness of device, so that the time resolution is generally not better than the active thickness over the drift velocity. By taking the values from fig. 1.4, the absorption of photons of energy above 11 keV is 22 times higher for GaAs than for silicon. The thickness of the active region of a GaAs based X-ray detector can therefore be thinner by the same

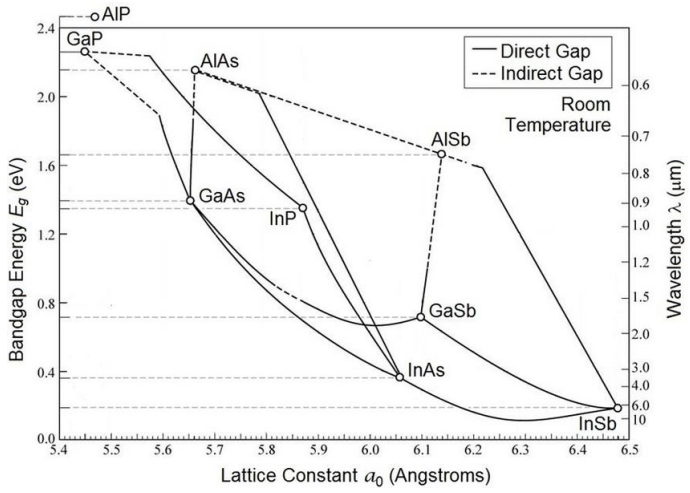

Figure 1.5: Diagram of lattice parameters vs. bandgap for different semiconductors.

factor as compared to a silicon detector with equal X-ray efficiency. Now, considering also approximately the 6 times higher mobility in GaAs compared to silicon, the time resolution improves by about two orders of magnitude if Si is replaced with GaAs.

The other important advantage of GaAs is its compatibility with $Al_xGa_{1-x}As$. Rare enough, $Al_xGa_{1-x}As$ has the same lattice parameter for all concentrations of Al x ranging from 0 to 45 while the bandgap is increasing with the concentration of Al. Above $x = 0.45$, however, the band gap becomes indirect. This unique and very useful property of $Al_xGa_{1-x}As$ can be inferred from the diagram in fig. 1.5. This allows us to perform the so called bandgap engineering - the possibility to tailor material composition, thus the bandgap, on the nanoscale. A detailed explanation including description of the particular structural designs we use, follows in sections 1.4 and 1.5.

1.4 Staircase APD-bandgap engineering

An important parameter in device performance is the ratio of electron gain to hole gain on passing through a region of the device: the statistical fluctuation in gain (noise) is reduced when one carrier type undergoes much stronger multiplication than the other. McIntyre et al. [16] have shown for the special case in which $\beta = k\alpha$, where k is a constant and α and β are the ionization coefficients of electrons and holes, respectively, that the noise spectral density when only holes are injected to the depletion layer is given by

$$2eI_{in}M^3\left[1+\left(\frac{1-k}{k}\right)\left(\frac{M-1}{M}\right)^2\right], \tag{1.3}$$

and if only electrons are injected to the depletion layer the expression modifies into

$$2eI_{in}M^3\left[1+(1-k)\left(\frac{M-1}{M}\right)^2\right], \tag{1.4}$$

where e is the elementary charge, I_{in} is the injected current and M is the current multiplication factor (gain). The analysis is limited to the white noise part of the noise spectrum only, and to diodes having large potential drops across the multiplying region of the depletion layer. The plots of the functions 1.3 and 1.3 for different values of the parameter k and two different normalisations in fig. 1.6.

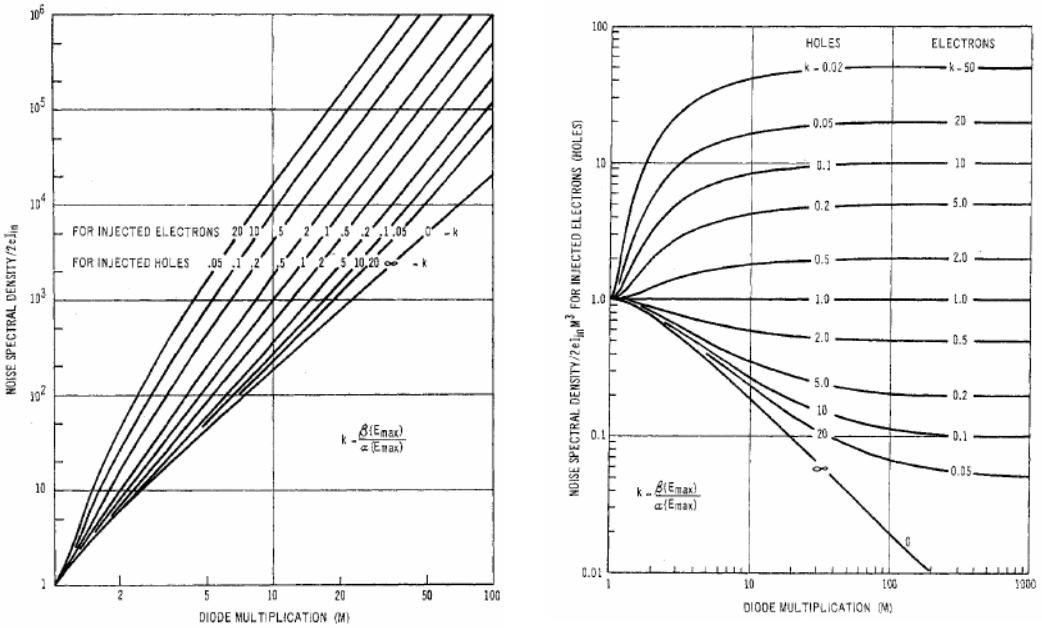

(a) (b)

Figure 1.6: Noise spectral density normalised by $2qI_{in}$ (a) and by $2qI_{in}M^3$ (b) vs. multiplication factor for either hole or electron injection, considering that $k = \beta/\alpha$

However, in the cited article of McIntyre et al., the constant k was defined as $\beta = k\alpha$, in this work we will work with k defined as $k = \frac{\alpha}{\beta}$.

While silicon has an ionization rate ratio $k \gg 20$ and therefore it is an ideal material for APDs used at the energies below 11 keV, unfortunately, most III-V semiconductors, as GaAs, have α and β nearly equal. It is, therefore, of great interest to explore the possibility of "artificial" increase (or decrease) of the α/β ratio in these materials by using a different device structures from a simple PIN homojunction. This can be done by employing the opportunity to tailor the material properties, notably the bandgap at the nanoscale, by changing the stoichiometry x in $Al_xGa_{1-x}As$ (bandgap engineering). It has been shown that in an AlGaAs/GaAs superlattice structure $\alpha/\beta = 8$ [11]. The large enhancement with respect to bulk GaAs is attributed to the large difference between the conduction and the valence band discontinuities [24, 25]. Multiplication

measurements in diodes with a graded bandgap avalanche region, which can be realized by varying linearly the Al composition of the alloy, have provided strong evidence of significant asymmetry between the effective ionization coefficients for electrons and holes [26]. Finally a structure called staircase APD has also been described by Capasso in 1983 [11], in which strictly only electrons impact ionize. A scheme of the bandgap structure of the multiplication region of such staircase APD is in fig. 1.7. The energy difference created by the bandgap discontinuity in the conduction band is noted as δE_c and the thickness of the graded region as l.

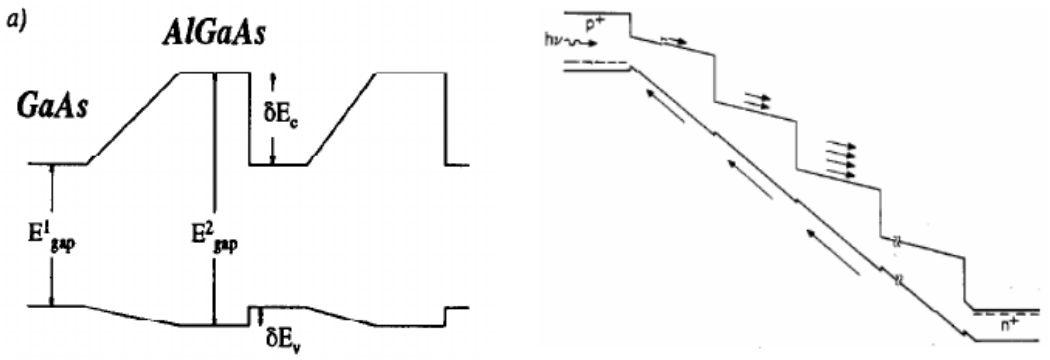

(a) (b)

Figure 1.7: Band diagram of (a) unbiased graded multilayer region and (b) the complete staircase detector under bias. The arrows in the valence band indicate that holes don't impact ionize. From [11, 13]

Ideally, the avalanche gain per stage is exactly 2; each electron impact ionizes once at each conduction-band step. In practice, the gain is $2 - \delta$, where δ is the fraction of electrons which do not impact ionize. The total gain of the structure is then $M = (2 - \delta)^N$, where N is the number of stages. Any hole-initiated ionization is caused by the applied electric field E only; the valence-band steps are of the wrong sign to assist ionization. For electron transport across the graded region, this bias field E must cancel the $\Delta E_c/l$ conduction-band quasi-electric field and provide a small extra component to assure drift, rather than diffusion transport. The device is then designed so that the hole ionization rate at fields $E > \Delta E_c/l$ is negligible.

The power of the noise of an APD per unit bandwidth can be described as [16]

$$\langle i^2 \rangle = 2eI_{ph}\langle M \rangle^2 F\,, \tag{1.5}$$

neglecting the dark current, where e is the elementary charge, I_{ph} is the unmultiplied photocurrent, $\langle M \rangle$ is the average avalanche gain and F the excess noise factor. To define it, we use following reasoning.

If the avalanche process were deterministic, in other words, if every injected photocarrier would undergo the same gain M, the factor F would be unity, and the resulting

noise would only be the multiplied input shot noise related to the poissonian distribution of the signal photons and to the stochastic rate with which a photon turns into the carriers. The avalanche process is instead intrinsically of statistical nature so that individual carriers have different avalanche gains characterized by a distribution with an average $\langle M \rangle$. This causes additional noise so that we can write [16]

$$\langle i^2 \rangle >= 2eI_{ph}\langle M \rangle^2 + 2eI_{ph}\sigma^2 \,, \tag{1.6}$$

where $\sigma = \langle M^2 \rangle - \langle M \rangle^2$ is the variance of the gain. Combining 1.5 and 1.6 we get following expression for the excess noise factor

$$F = \frac{\langle M^2 \rangle}{\langle M \rangle^2} = 1 + \frac{\sigma^2}{\langle M \rangle^2} \,. \tag{1.7}$$

In our experiments we always measure $\langle M \rangle$, usually denoted as M. It has been shown by McIntyre et al. [16] that σ strongly depends on the ratio of ionization coefficients α/β, as we already mentioned. In order to describe the excess noise of staircase APDs quantitatively as in [15], let us consider the excess noise factor of equation 1.5 to be dependent on the number of steps N and a random variable δ, which is telling us the probability that the electron will not impact ionize (the probability that the gain m at given bandgap step will be 1 is δ, while the probability of having $m = 2$ is $(1-\delta)$). The noise contribution of the n^{th} stage ($1 \leq n \leq N$) is multiplied by the rest of the stages by the factor $(2-\delta)^{2(N-n)}$. We write the mean-square noise current generated by the n^{th} stage as

$$\langle i^2 \rangle = 2eI_{n-1}(\langle m^2 \rangle - \langle m \rangle^2) = (\delta - \delta^2)(2eI_{n-1}) \,, \tag{1.8}$$

where $I_{n-1} = I_0(2-\delta)^{n-1}$ is the average current at n^{th} stage. The total noise per unit bandwidth on the output signal is

$$\langle i^2 \rangle = 2eI_0(2-\delta) + \sum_{n=1}^{n=N} 2eI_0(2-\delta)^{n-1}(\delta - \delta^2)(2-\delta)^{2(N-n)} = \tag{1.9}$$

$$= 2eI_0(2-\delta)^{2N}\left[1 + \sum_{n=1}^{n=N} \frac{\delta(1-\delta)}{(2-\delta)^{n+1}}\right] ,$$

so the excess noise factor can be written as

$$F(N,\delta) = 1 + \delta\frac{1-(2-\delta)^{-N}}{2-\delta} \,, \tag{1.10}$$

from where it is seen that we are approaching the ideal case $F = 1$ as δ gets close to zero. In order to have such conditions, the bandgap discontinuities have to be realized at a distance shorter than the mean free path of the carriers, which is provided by using

MBE (2.2).

1.5 Separated absorption and multiplication regions

Beside the staircase structure, the important feature of our devices is the separation of the multiplication and absorption regions. This design was proposed by Capasso in [11] in order to make the multiplication process more defined spatially and, as a consequence, to decrease the intrinsic noise of the devices. A realization of the structure proposed by Capasso is described in [13, 27]; the particular device structure used in this publication is reported in fig. 1.8.

The staircase diode is an effective multiplier for electrons. In order to use this advantage one has to ensure that only electrons are injected into the multiplication region, otherwise the gain is reduced while the amplification noise is increased. This injection condition can be achieved if an absorption layer is placed between the p-contact and the multiplication region. This detector concept is called separate absorption and multiplication region avalanche photo diode (SAM-APD). With reference to the simplified structure of fig. 1.8 (top), the incident radiation should be absorbed completely in the absorption region. In this way, in fact, the generated electrons drift towards the multiplication region and eventually to the n-contact, while the holes are collected at the p-contact. In order to reduce the electric field strength in the absorption region and avoid in this way multiplication in this part of the device, a p-doped region separates the multiplication region from the absorption region. In this way, the absorption region is confined between the top p contact and the p-doped layer and will thus be subject to a negligible electric field. For X-ray photons with energies above 11 keV, having a 4.5 $-\mu$m-thick absorption region and a 1 $-\mu$m-thick multiplication region, one can assume that nearly 80% of the absorbed photons generate electron-hole pairs in the absorption region while 20% produce a mixed injection condition in the multiplication area.

The p-doping concentration in the separation region needed for optimal functionality of the SAM-APD devices was also a subject of studies and will be discussed in section 4.1.

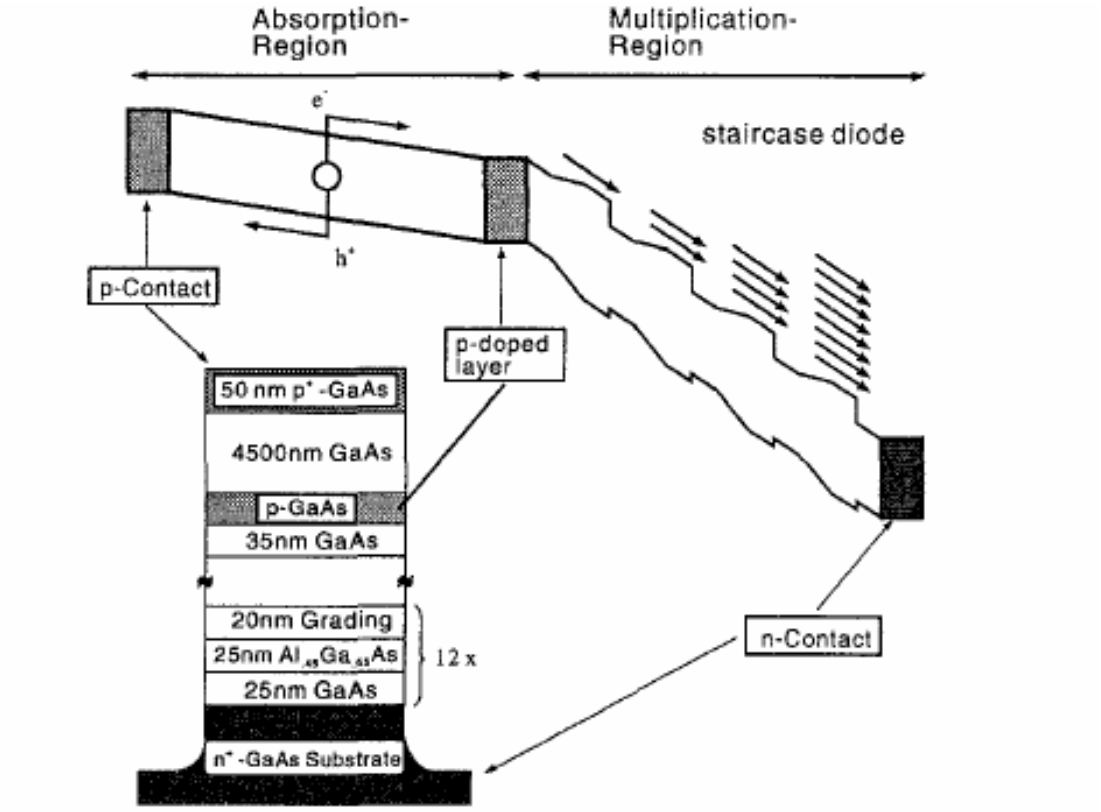

Figure 1.8: Simplified band structure (top) and layer structure (bottom) of the SAM-APD detector. From [27]

2. Fabrication and experimental techniques

This chapter is dedicated to methods and techniques employed during manufacturing and later testing of SAM-APD. The first section focuses on MBE, its basic principles, description of the apparatus (in particular the one installed at IOM-CNR), followed by the growth process and calibration methods.

The next section 2.2 describes the fabrication techniques which were used. Section 2.3 describes the methods which were used to check the quality of the samples. Finally, section 2.4 is dedicated to the description of the light sources which were used to measure response of the device to photons of various energies, to evaluate noise level and probe the time response quality.

2.1 Molecular beam epitaxy

MBE is an Ultra-High-Vacuum (UHV)-based technique for producing high quality epitaxial structures with sub-monolayer (ML) precision. Since its introduction in the 1970s as a tool for growing high purity semiconductor films, MBE has evolved into one of the most widely used techniques for producing epitaxial layers of metals, insulators, semiconductors, and superconductors, both at the research and at the industrial production level. The basic principle of MBE growth is as follows: a flux of atoms or clusters of atoms is being created by heating of a solid source. The fluxes are then flowing almost without collisions with other particles, thanks an UHV environment, upto a heated substrate surface, where they can diffuse and eventually are incorporated into the growing film.

Despite the conceptual simplicity, great technological effort is required to produce systems that yield the desired quality in terms of material purity, uniformity, and interface control. An exhaustive discussion of the principles and applications of the MBE technique can be found in [28].

The choice of the MBE with respect to other growth techniques depends on the desired structures and needs. In particular, MBE is the proper technique when abruptness and control of interfaces and doping profiles are needed, thanks to the low growth temperature and rate. As mentioned in the section 1.4, for growing staircase structure, the MBE technique is indispensable.

Besides, the control of the vacuum environment and of the quality of the source materials allows a much higher material purity, as compared to non UHV based techniques, especially in semiconductors containing aluminium for applications in high

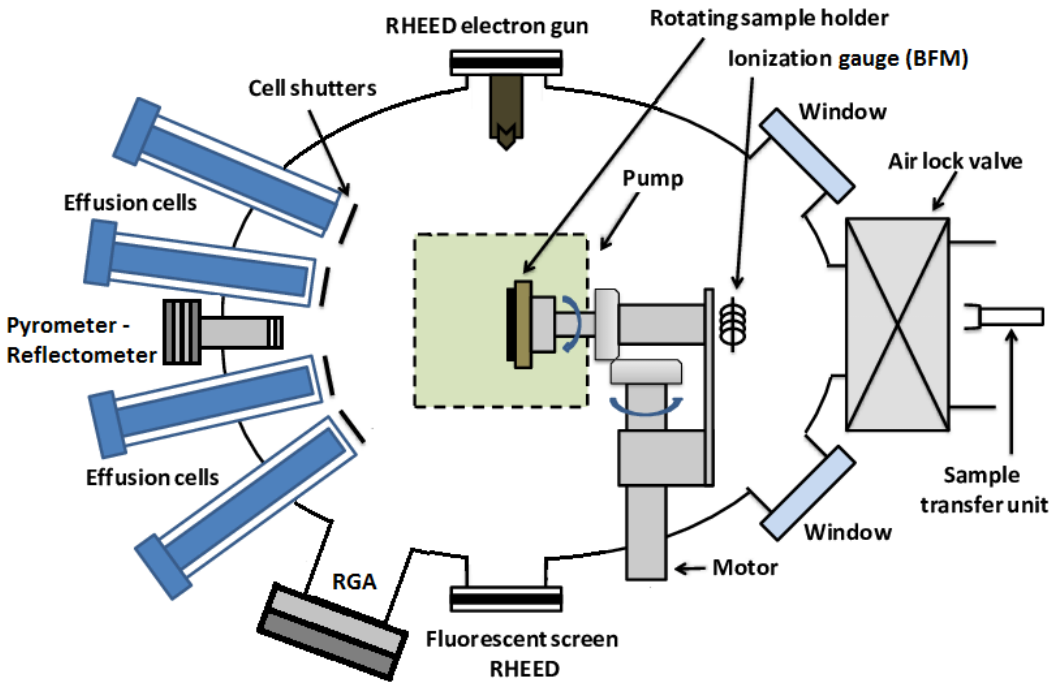

Figure 2.1: Schematic of MBE apparatus installed in IOM-CNR, Trieste, Italy.

Figure 2.2: MBE apparatus installed in IOM-CNR, Trieste, Italy.

mobility and high speed devices.

2.1.1 MBE growth apparatus

A schematic drawing of the high mobility MBE system installed at IOM-CNR in Trieste is shown in Fig. 2.1. The MBE chamber is mainly dedicated to the growth of GaAs-based heterostructures characterized by a very high material purity that ensures high carrier mobility in 2D electron gases at low temperatures. Such a system requires some peculiar modifications compared to a standard MBE apparatus. Two 3000 l/s cryopumps replace standard ion pumps, providing a cleaner, higher-capacity pumping system. All-metal gate valves are mounted to eliminate outgassing from Viton seals. No group-II materials, such as Be, are used for p-doping, since they are known to drastically reduce carrier mobility; a carbon source is used instead for p doping. High-capacity and duplicated cells are used to avoid cell refilling or repairing for extended periods. Extensive degassing and bake out duration (three months at 200 °C) were carried out after the installation of the MBE system to increase the purity of the materials. The description of some elementary components follows:

- *The growth chamber*: a stainless-steel chamber, UHV connected to a preparation chamber, where substrates are degassed prior to growth. All the components of the growth chamber must be able to resist bake-out temperatures of up to 200 °C for extended periods of time.

- *The pumping system* must be able to efficiently reduce residual impurities to a minimum. Typically the base pressure in the MBE chamber is from 10^{-11} to 10^{-12} mbar. This helps reducing concentration of impurities below 10^{14} cm^{-3} in grown structures.

- Liquid N_2 *cryopanels* surround internally both, the main chamber walls and the source flanges. Cryopanels prevent re-evaporation from parts other than the hot cells and provide thermal isolation among the different cells, as well as additional pumping of the residual gas.

- *Effusion cells* are the key components of an MBE system, because they must provide excellent flux stability and uniformity, and material purity. The cells are placed on a source flange, and are co-focused on the substrate to optimize flux uniformity. The flux stability must be better than 1% during a work day, with day-today variation a few % [29]. This means that the temperature control must be less than ±1 °C at typical operating temperatures around 1000 °C [28]. The material to be evaporated is placed inside a pyrolitic boron nitride crucible. A mechanical or pneumatic shutter, usually made of tantalum or molybdenum, is

placed in front of the cell, and it is used to trigger the flux coming from the cell with response times much faster than the growth rate (typically 1ML/sec) (see Fig. 2.1). The high mobility MBE system at IOM CNR includes 2 Ga, 2 As, 1 Al, 1 In evaporation sources, while n and p type doping are provided by Si and C (graphite) filament sublimation sources, respectively.

- *The substrate manipulator* holds the wafer on which the growth takes place. It is capable of a continuous azimuthal rotation around its axis to improve the uniformity across the wafer. The heater behind the sample is designed to maximize the temperature uniformity and minimize power consumption and impurity outgassing. Opposite to the substrate holder, an ionization gauge is placed. It can be moved to face the molecular beams and is used as a beam flux monitor (BFM).

- *The Reflection High Energy Electron Diffraction* (RHEED) gun and detection screen are used to assess the morphology and the crystalline order of the surface, and to calibrate precisely the material fluxes evaporated by the effusion cells; with RHEED it is possible to monitor the epitaxial growth ML by ML. More details on this tool is given in the section 2.1.3.

- *The Reflectometer* is used for in-situ monitoring of thickness during growth as well. The light impinge on the substrate with normal incident and its reflection is recorded. Either a light from white lamp with subsequent spectrum analyser or, as in our system, monochromatic diode(s) can be used. Recording such reflected signal during growth, we acquire a harmonic response in time, where the maxima-minima distances are given by $d = \lambda/4\, n$, where n is the refractive index and λ the wavelength of the probing light. By a careful calibration of the refractive index for given materials through an iterative process with X-ray diffraction data (see below in sec. 3.1.1), the thickness, and thus the growth rates can be monitored in-situ.

- *The quadrupole residual gas analyser* (RGA) is a mass spectrometer analysing composition of residual gas in the chamber. This tool is also used for leak-testing the vacuum system through helium detection.

2.1.2 MBE growth process

In general, three different phases can be identified in the MBE process [28]. The first is the crystalline phase constituted by the growing substrate, where short- and long-range order exists. On the other extreme, there is the disordered gas phase of the molecular beams. Between these two phases, there is the near-surface region where the impinging molecular beams interact with the hot substrate. This is the phase where

the phenomena most relevant to the MBE process take place. Atomic or molecular species get physisorbed or chemisorbed on the surface. There they can undergo different processes. The MBE growth of III-V semiconductors uses the so called three temperatures method [28], in which the substrate is kept at an intermediate temperature between the evaporation temperature of source materials of the group III (around 300 °C for As) and group V (around 800 °C and 1000 °C, 1100 °C, for In, and Ga, Al, respectively). At the substrate temperature, the vapour pressure of group III species is nearly zero; this means that every atom of the III species that impinges on the substrate is chemisorbed on its surface; in other words group III atoms have a unit sticking coefficient. The high vapour pressure of the group V species favours, on the contrary, the re-evaporation of these species from the sample surface. Due to the higher group V species volatility with respect to group III, growth is usually performed with an V/III beam flux ratio much higher than one. This flux imbalance does not affect the one-to-one crystal stoichiometry between III-V species. In fact, as shown by [29, 30], in the case of homoepitaxial growth of GaAs, As atoms do not stick if Ga atoms are not available on the surface for bonding. So, in the case of GaAs, the growth rate is driven by the rate of the impinging Ga atoms on the substrate.

2.1.3 Growth rate calibration

The growth rates of GaAs and AlAs are calibrated by the intensity oscillations of the specular spot of the RHEED signal during the growth of a GaAs or AlAs film on a GaAs substrate. This technique employs a high energy (up to 20 keV) electron beam, directed on the sample surface at grazing incidence; the diffraction pattern of the electrons is displayed on a fluorescent screen and acquired by a CCD. Thanks to the grazing incidence and the limited mean free path of electrons in solids, the electron beam is scattered only by the very first atomic layers, giving rise to a surface-sensitive diffraction pattern. During crystal growth the intensity of the zero order diffraction spot (the specular spot) is recorded as a function of time. The intensity of the spot has an oscillatory behaviour. This happens because a flat surface, present when a ML is complete, reflects the electrons optimally while in a condition in which a half-ML has been deposited the electron beam gets partially scattered by the rough surface. Starting with a flat surface and proceeding with growth, the incident electron beam gets partially scattered by the islands steps of the growing ML, thus reducing the reflected intensity. Scattering becomes maximum at half ML coverage, while as the new ML completes the surface flattens again by coalescence of the islands, and the reflected intensity recovers its value. Thus, a period of RHEED oscillation corresponds to the growth of one single ML. By measuring the time necessary to complete a certain number of oscillations one can calculate the growth rate in ML/s for a fixed effusion

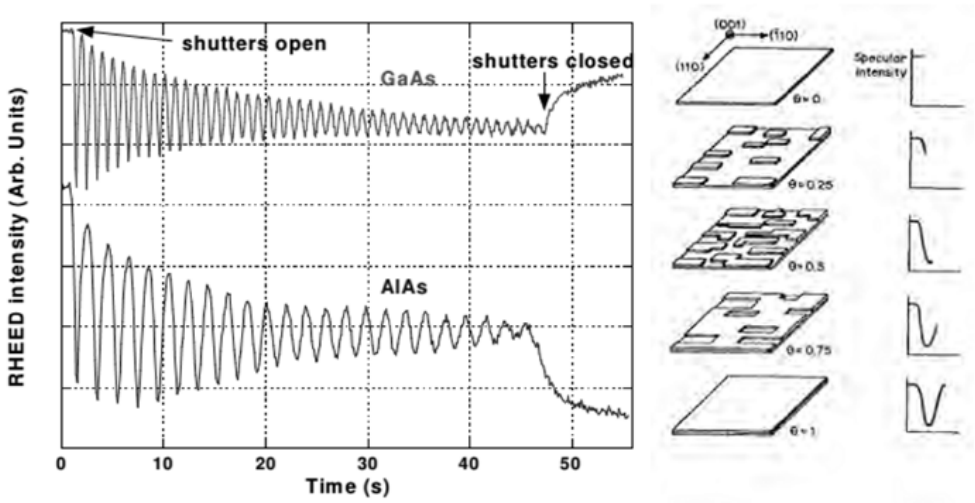

Figure 2.3: RHEED oscillations. In the left panel an actual measurement for GaAs and AlAs grown on GaAs (001). In the right panel a schematic view of the relationship between RHEED intensity and monolayer coverage θ.

cell temperature, and easily convert it to units of Å/s knowing the lattice parameter of GaAs or AlAs. An example of RHEED oscillations together with the illustration of the principal is in fig. 2.3

Reflectometry becomes reliable for layer thicknesses $> \lambda/4$, i. e. much thicker than typical thicknesses of RHEED oscillations (a few to a few tens of ML), which makes the former much less sensible to statistical fluctuations and to flux transients, and thus more precise. Additionally, reflectivity probes a larger spot size (about a cm diameter) than RHEED and can be used during sample rotation, making it less sensible to spatial flux variations. An example of reflection oscillations is in fig. 2.4

This calibration is performed almost daily, prior to sample growth, on a ad hoc substrate. The day-to-day variation of R_{GaAs} and R_{AlAs} , with constant cell temperatures is $\sim 1\%$; the long term behaviour of these rates, on the other hand is fairly predictable, and is constant (within $1-2\%$) until the cell is almost empty, unless major changes to the cell environment happen (like refilling, etc).

2.2 Fabrication techniques

In this section the methods of fabrication utilized during preparation of the devices are described. We introduce here the general procedures and mechanisms which will be applied in the fabrication process in section 3.1.

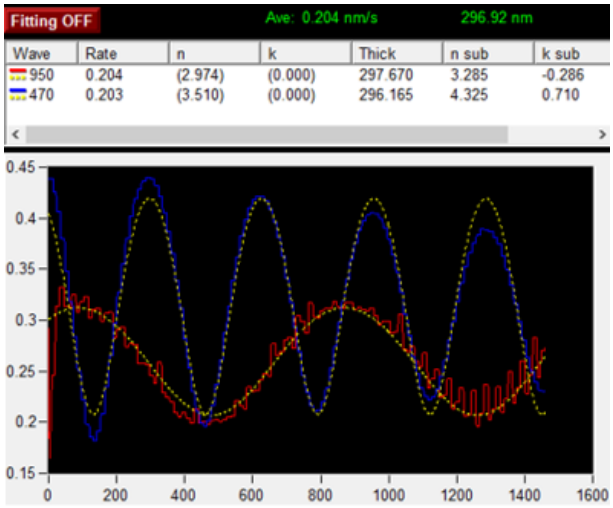

Figure 2.4: A reflectivity measurement with two different wavelengths (λ_1 = 950 nm, λ_1 = 470 nm). The x-axes is time in seconds.

2.2.1 Photolithography

Many miniaturization methods start with lithography, the technique used to transfer copies of a master pattern onto the surface of a solid material. The most widely used form of lithography is photolithography. In short, by illumination through the mask the mask pattern is transferred to the latent image in the photoresist deposited on the surface of the sample.

Photoresist

A photoresist is a solution composed mainly by a polymer, a sensitizer and a casting solvent. The polymer changes structure when exposed to a radiation, the sensitizer controls the photochemical reactions, the solvent allows the deposition of the resist on the substrate and the formation of thin layers on the surface to be covered. The tone of the photoresist describes its reaction to the exposure. When the photoresist is of the positive tone, the photochemical reaction during exposure weakens the polymer causing disconnection of the main and side polymer chains, resulting in a higher solubility of the exposed resist. The solubility of the exposed resist is faster than the development rate of the unexposed resist. When the photoresist is of the negative tone, the exposure causes the strengthening of the polymer by random cross-linkage of main or pendant side chains, making the exposed parts less soluble. The principles of use of these two basic and most general types of photoresists are in fig. 2.5.

Currently many other resists for particular applications are available on the market. One interesting example is image reversal resists which are positive resists with an additional amine, where depending on the manufacturing process, either positive or negative images may be generated. Further available resists for special applications

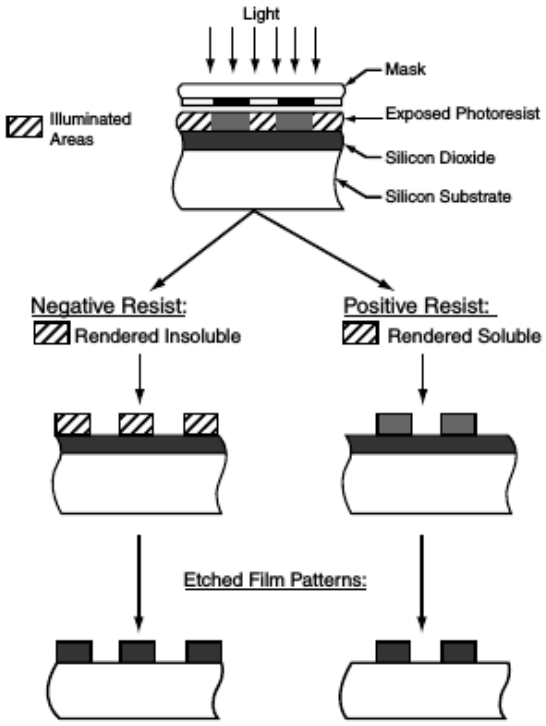

Figure 2.5: Positive and negative resist exposure, development, and pattern transfer example on Si/SiO_2 sample. Positive resists develop in the exposed region. Negative resists remain in the exposed region. From [31].

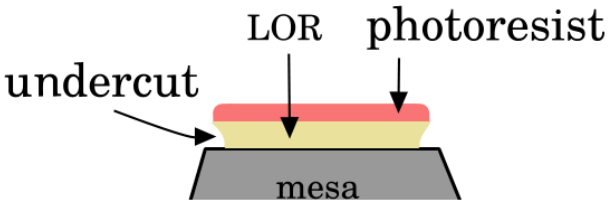

Figure 2.6: Illustration of undercut created in the double resist structure of LOR technique.

include positive polyimide resists (high-temperature applications 300°C), negative PMMA photoresists (water-free development for sensitive substrates, polymer PMMA and cross-linker), positive and negative two-layer photoresists (lift-off technologies, polymer copolymer PMMA). In the last case, lift-off technologies, application of two resists is performed subsequently. The first one, lift-off resist (LOR), directly in contact with a substrate, is not photo-sensitive. This technique is employed when there is a need to perform subsequent deposition of a layer which is meant to cover just a particular places of the structures, typically a metallization layer. The advantage of LOR technique during these processes is the undercut created in LOR below the photoresist (fig. 2.6). The material to be deposited does not reach the surface below this undercut, which creates discontinuity in the layer and enables consequently the solvents to reach and remove the resists from the surface of the sample. If only photoresist were used in

such processes, the resist strip becomes very problematic point.

Spin coating

One of the techniques used to cover a surface with a thin, homogeneous layer of photoresist is the spin coating. The photoresist - a viscous solution - is dispensed onto the sample, which is then spun at high speed. The spinner chuck, which can be either mechanical or vacuum based, holds the sample in the place. The speed at which the sample is spun varies from hundreds to thousands rotations per minute (rpm) depending on the viscosity and the target film thickness. At the optimal speed centrifugal forces causes the solution to flow to the edges, where it builds up until the surface tension is exceeded. The rotation at high speed causes the resist to deposit homogeneously. The resist thickness is a function of spin speed, solution concentration and molecular weight and can be valued using the empiric expression [32]:

$$t = K\frac{C^{\beta} \cdot \mu^{\gamma}}{\omega^{\alpha}}, \tag{2.1}$$

where K is a calibration constant, C the polymer concentration in g/100ml solution, μ the intrinsic viscosity, ω the rotation speed in rpm and α, β, γ parameters to be determined. The quality of resist coating determines the density of defects transferred to the final structure. After the a spin coating the resist still contains up to 15% of the solvent and the layer can have inner tension: the coated sample is then soft baked (this operation is also known as a pre exposure bake or post coat bake), to promote residual solvent evaporation, surface adhesion and to reduce the inner tensions in the layer of resist and consequently reduce the pattern distortion in the subsequent process. Temperature and time of the soft bake are specific to every resist, can be found in the data sheets and are crucial for optimal photo-sensitivity of resulting layer of resist.

Illumination and development

After soft baking, the resist-coated sample is transferred to some type of illumination or exposure system where they are aligned with the features on the mask. The photomask for UV lithography is composed by flat glass or quartz substrate, transparent respectively to near and deep ultraviolet, and an absorber pattern metal layer, usually consisting of chromium, opaque to UV. For any lithographic technique to be of value, the alignment technique must be capable of a precise (a small fraction of the minimum feature size) superposition of the mask pattern and the pattern on the wafer.

In the simplest case an exposure system consists of a UV lamp, illuminating the resist-coated sample through a mask without any lenses between the two - contact and proximity masks. These shadow printing techniques were very important in the

pioneer times of microfabrication. Especially with the contact masks, it was possible to get relatively good resolution with small technological demand. The drawback of this method is high defectivity and rapid mask degradation. The projection printing inserts imaging optics between the mask and the sample, prolonging the mask life time, reducing defects and, considering reduction of the mask pattern by factor 4,5 or 10 by imaging optics, making mask fabrication less challenging [31]. However the projection printing is the nowadays technology of cutting edge in a microdevice fabrication, in the presented work the contact mask was adequate choice considering the microfabrication requirements.

The purpose of the illumination is to deliver light with the proper intensity, directionality, spectral characteristics, and uniformity across the wafer, allowing a nearly perfect transfer of the mask image into the resist in the form of a latent image.

During the latent-image-forming reaction, the sensitizer in the resist usually bleaches; in other words, exposed resist is rendered transparent to the incoming wavelength. This bleaching allows the use of thick films with high absorbency, since light will reach the substrate through the bleached resist. The absorbency of the unexposed resist should not reach 40% so as to avoid degradation of the image profile through the resist depth, as too large percentage of the light is absorbed in the top layer. On the other hand, with the absorbency far below 40%, exposure times required to form the image become too long. The smaller the dose needed to transfer the mask features onto the resist layer with good resolution, the better the resist sensitivity.

Post exposure treatment is often desired, because the reactions initiated during exposure might not have run to completion. To halt the reactions or to induce new ones, several postexposure treatments are in use: postexposure baking, flood exposure with other types of radiation, treatment with reactive gas, and vacuum treatment. Postexposure baking and treatment with reactive gas are used in image reversal (negative resist) and dry resist development.

The optical lithography (Karl Süss MJB3) at TASC-IOM-CNR clean room works with spectral line of mercury lamp of 365 nm wavelength. A spatial resolution and an accuracy of a mask aligner are 300 nm.

The next step in photolithographic process is development. It transforms the latent image formed in the resist during the exposure into a relief image that will serve as a mask for further steps. During the development process, selective dissolving of the resist takes place. Two main technologies are available for development: wet development, widely used in circuit and miniaturization manufacture in general, and dry development, which is starting to replace wet development for some of the ultimate line width resolution applications. Two main types of wet development setups are used: immersion and spray development. During immersion developing, sample is immersed for a limited time period in a developer bath and agitated at a specific tem-

perature. During spray development, fan-type sprayers direct fresh developing solution across wafer surfaces.

Resolution and minimum feature size

Correct feature size must be maintained during the transfer of the pattern from the mask to the sample. The term critical dimension (CD) refers to a specific minimal feature size and is a measure of the resolution of a lithographic process.

In the shadow printing mode, including contact and proximity arrangements of the mask and the sample, an optical lithography has a resolution with limits set by a variety of factors. These include diffraction of light at the edge of an opaque feature in the mask as the light passes through an adjacent clear area, alignment of sample to mask, nonuniformities in sample flatness, and debris between mask and wafer. Diffraction causes the image of a perfectly delineated edge to become blurred or diffused. Therefore we define the theoretical, diffraction limited resolution R as half of the finest grating period and at the same time the minimum feature size transferable. For contact mask it can be written as [31]

$$R = \frac{3}{2}\sqrt{\frac{\lambda z}{2}}, \tag{2.2}$$

where λ is wavelength used for illumination and z is photoresist thickness. The theoretical maximum resolution is seldom achieved, however, as only the diffraction effects were taken into account to derive equation 2.2. The other factors mentioned above (wafer flatness, mask alignment, etc.) usually conspire to make the resolution worse.

2.2.2 Etching

Process of a controlled material removal from its surface is called etching. There are two fundamental groups of etching - wet and dry. In the former the detachment of material is happening in a liquid, while in the latter the material is transferred into the gaseous phase. The use of wet etching techniques has a long history in treating surfaces and materials. We can distinguish also chemical and physical etching. The wet etching is always chemical since the process of removal of material is based on chemical interaction between sample and etchant. Dry etching is realized by glow discharge (plasma) or ion beam methods. Physical dry etching requires high kinetic energy of ions, electrons or photons to etch off the substrate atoms. When the high energy particles knock out the atoms from the substrate surface, the material evaporates after leaving the substrate. Dry etching can be also of physical-chemical nature, where impinging particles disturb the structure of the material being etched and the etching gas reacts chemically with the activated surface creating volatile compounds which are then removed by gas flux. In the fig. 2.7 are schematics of important dry etching

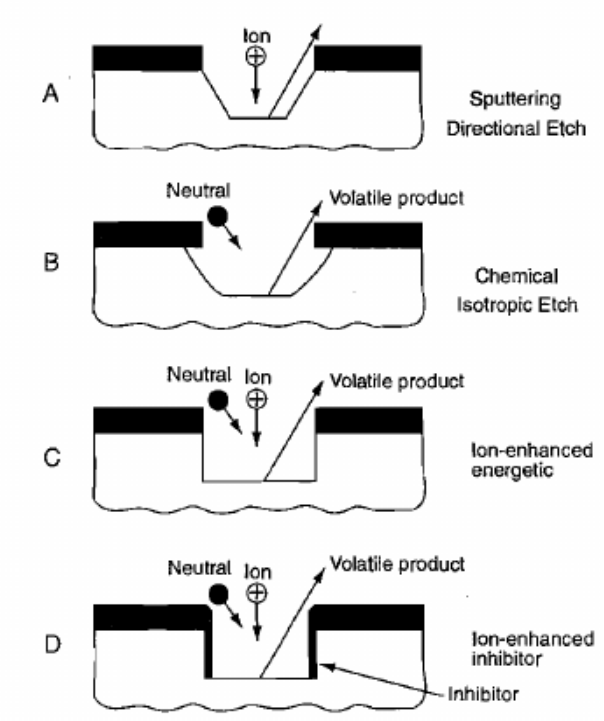

Figure 2.7: Important dry etching profiles associated with different dry etching techniques. From [31].

profiles associated with different dry etching techniques: (A) Sputtering and formation of trenches (ditches) in physical ion etching. The mask is etched most rapidly in the neighborhood of the mask corner. The slope becomes less steep and not all ions arrive at the etch bottom parallel to the sides. (B) Chemical etching in a plasma at low power and relative high pressure leads to isotropic etching (uniform in all directions) and lateral undercuts. (C) Ion-enhanced etching: physical-chemical is the most perfect image transfer as the undercutting is limited by the combined action of physical and chemical etching. The low pressure and high power lead to directional anisotropy. (D) Ion-enhanced inhibitor. Sidewalls are protected from undercutting by a surface species (e.g., a polymer) which are being deposited on the sidewalls during the etching.

Nowadays the etching techniques have become a key process for the fabrication of semiconductor micro-devices and micro-components since they allow a much more refined removal from a solid surface compared to mechanical methods. This is very important since in the modern microelectronics, the structures in the sub-micrometer resolution are needed. The etching of semiconductors is in fact widely used at all the stages of the microsystem technology, such as for removing contaminants from the wafers, for creating three-dimensional structures, for revealing buried layers to define electrical contacts, etc.

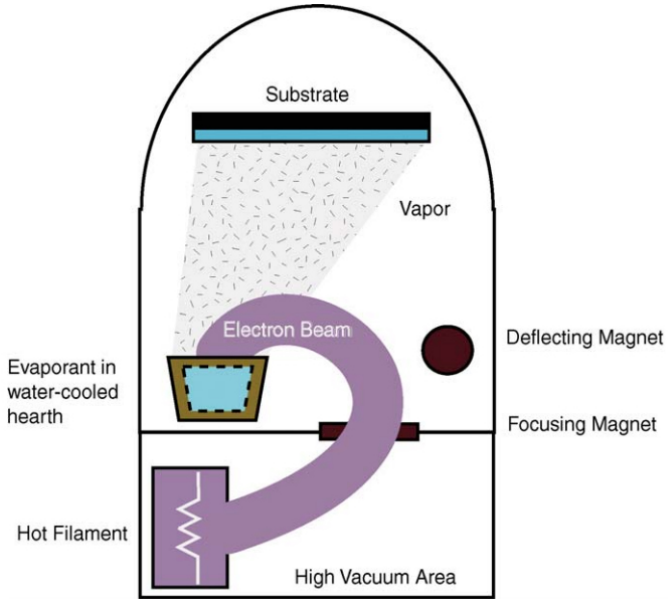

Figure 2.8: The schematic of e-beam evaporator.

2.2.3 E-beam evaporation

Electron-beam evaporation is a form of physical vapour deposition in which a crucible with material to be deposited represents a target anode and is bombarded with an electron beam given off by a tungsten filament placed below the crucible. The beam is on its pass focused and banded by magnets to reach the anode. The crucible is positioned in a copper multi-pocket e-beam carousel cooled by water to suppress thermal deposition and promote in this way the deposition caused by e-beam: the electron beam causes atoms from the target to transform into the gaseous phase. These atoms then precipitate into a solid form, coating everything in the vacuum chamber (within line of sight) with a thin layer of the anode material.

The e-beam evaporation is high vacuum process with working pressures 10^{-5} – 10^{-7} mbar. A scheme of a typical set-up is depicted in fig. 2.8. Some evaporation systems may contain many crucibles in order to perform multiple material deposition without breaking the vacuum. They may contain a large number of wafers suspended above the crucibles.

The thickness monitoring is done through quartz crystal microbalance (QCM), consisting of a thin disc of quartz crystal into the chamber, placed where it is exposed to the deposition. The resonance frequency is being continuously probed and read out. As the material is sticking to the surface of the crystal, this resonance frequency is changing. For small masses of deposited material the change in the resonance frequency is directly proportional to deposited mass. A calibration of this change of resonance frequency to the thickness for each material to be deposited is needed.

2.3 Dark characteristics

To check the quality of the devices the current-voltage (IV) characteristics and capacitance-voltage (CV) characteristics are measured in the dark through a semiconductor device analyzer B1500A by Agilent (fig. 2.9). It supports measurement in the ranges of 0.1 fA - 1 A and 0.5 μV - 200 V, spot and sweep measurement, time sampling measurements (up to 5 ns sampling interval), pulsed measurements with minimum pulse widths of 50 μs, multi-frequency AC impedance measurement supports CV , C-t (capacitance versus time) and C-f (capacitance versus frequency) measurement in frequency range of 1 kHz to 5 MHz etc. [33].

(a) (b)

Figure 2.9: Semiconductor device analyzer B1500A by Agilent front (a) and from the back (b).

Dark current characteristics

The dark current characteristics (IV dependences measured without presence of light) are measured using the semiconductor device analyzer B1500A described above, biasing the device always reversely and probing range of voltages from 0 V to breakdown voltage.

In the ideal case the only origin of dark current would be the thermal generation of electron-hole pair. In such case the dark current is scaling with the area of the device. To be able to compare devices with different areas A we define dark current density as

$$J(V) = \frac{I(V)}{A}, \tag{2.3}$$

where $I(V)$ is the dark IV characteristic.

In reality the dark current has also other components created by crystalline structure or interface defects.

Dark current has strong temperature dependence. Here presented measurements were done at room temperature.

Capacitance voltage characteristics

The measurements of capacitance in dependence on voltage were performed both through the multi-frequency unit of B1500A and through precision LCR meter (HP4284A). The capacitance measurements are bringing us a knowledge about electric field distribution inside of the device.

Considering for simplicity our device as an ideal parallel-plates planar capacitor with relative permitivity ε_r we can write the depletion width as

$$d(V) = \frac{\varepsilon_r \varepsilon_0 A}{C(V)}, \tag{2.4}$$

where A is the area of the mesa, $C(V)$ is the measured capacitance as a function of reverse bias V, ε_r and $\varepsilon_0 = 8.854 \cdot 10^{-12}$ F/m are the equivalent relative permittivity of the material and the permittivity of vacuum, respectively.

2.4 Light sources for detector tests

In this section, the light sources used for device tests are described. These include both table-top laser sources and synchrotron radiation beamlines. A short outline of the principles of synchrotron radiation is provided as well.

2.4.1 Green lasers

As the first light source for the testing of the SAM-APD detectors a green lasers ($\lambda = 515 - 540$ nm) was chosen. This photon energy range was selected in order to ensure, that photogeneration takes place entirely within the absorption region. In fact, the absorption length in GaAs is about 140 nm for this wavelengths [34]. This enables us to study the pure multiplication effect, without having it combined with charges generated in the multiplication region.

Three different lasers were used for different experiments:

- A continuous wave table top laser MILLENNIA V, all solid-state, diode-pumped of wavelength $\lambda = 532$ nm, power stability $\pm 1\%$ (after 30 min warm-up), noise $< 0.1\%$ rms (over a 10 Hz - 10 MHz bandwidth) [35]

- An infrared (fundamental $\lambda = 1030$ nm) ytterbium doped fibre laser of output power 0.4 W, using its second harmonics of wavelength $\lambda = 515$ nm with pulse repetition rate 40 MHz and pulse width set on 10 ps

- A pulsed table top laser of wavelength $\lambda = 540$ nm with pulse repetition rate 200 kHz and pulse width set on 100 fs, delivering an average power of 500 μW.

2.4.2 Synchrotron beam-line setup

Synchrotron in general is a type of accelerator in which charged particles travel in a closed path. Its fundamental parts are bending magnets enabling the path to be closed and at least one cavity where particles gain energy by means of interaction with alternating electric field the frequency of which is synchronized with their movement. The largest synchrotrons were built to produce high energy particles. A different application of synchtrotrons is to generate electromagnetic radiation in a large range of energies up to those of X-rays. This radiation is produced when a charged particle (in this case electrons) is accelerated, by changing speed, but in the case of synchrotron more likely by changing its trajectory. The mechanism of x-ray emission by electron acceleration is essentially the same as that of bremsstrahlung radiation. Originally this 'synchrotron radiation' was considered parasitic at the beginning, but devices optimised for its generation are being used and built all around the world. They should be correctly called 'synchrotron light sources' but since their number and importance is so big they are often simply referred as synchrotrons. They are sources of radiation of high flux, brilliance and special collimation, polarization and timing properties.

The core of a synchrotron light source is a storage ring with a 'racetrack' design with straight sections and curves. In a storage ring electrons are kept at constant energies with their speed very close to the speed of light so they are relativistic. Charged particles emit electromagnetic waves when they are being accelerated. So traditionally the bending magnets controlling the closed paths were used to generate radiation.

One of the main figures of merit of the the x-ray sources is "brightness" (often called "brilliance"), which takes into account number of photons produced per second N/t [numeber/s], the angular divergence of the photons, or how fast the beam spreads out Ω [mrad^2], the cross-sectional area of the beam A [mm^2] and the photons falling within a bandwidth (BW) of 0.1% of the central wavelength or frequency and relates them as

$$brilliance = \frac{N \cdot s^{-1}}{\Omega \cdot A \cdot 0.1\%\mathrm{BW}} .$$

With the need to increase mainly the energy and brightness of emitted beam wigglers were designed. They consist of magnets with alternating polarity inserted into the straight sections. Here electrons move generally straight except small wiggles where they are highly accelerated and the appropriate radiation is emitted.

Instead of wigglers most modern machines preferentially use so-called undulators, since they are the most powerful generators of synchrotron radiation at storage rings.

Like wigglers, they consist of periodic arrangements of dipole magnets generating an alternating static magnetic field which deflects the electron beam sinusoidally. The special properties of undulator radiation arise from the fact that due to the small amplitude of the oscillations the radiation cones emitted during each oscillation period

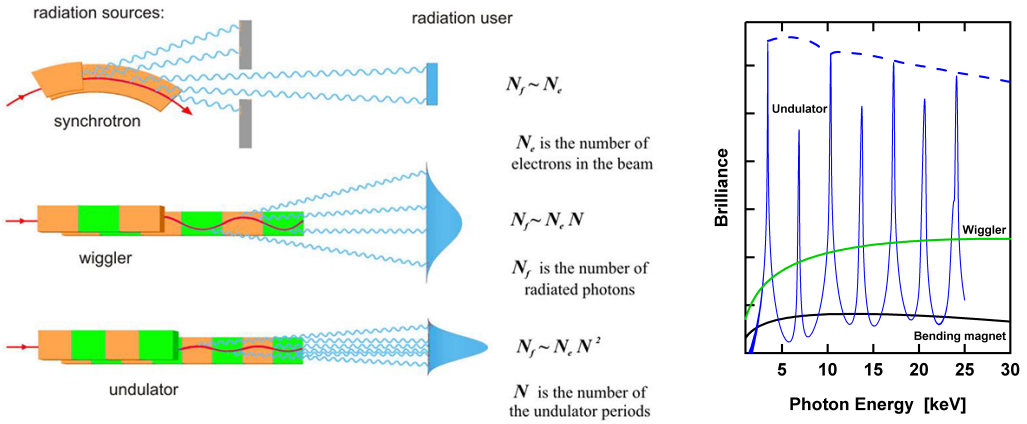

(a) (b)

Figure 2.10: Schematic of different x-ray radiation sources illustrating principles and reasons of different brilliance [36] (a) and qualitative comparison of brilliance of banding magnet, wiggler and undulator [37] (b).

overlap and interfere. This means the series of N magnets acts similarly to a diffraction grating, generating a spectrum of peaks due to constructive and destructive interference of the radiation cones. A comparison of the different types of X-ray sources is in fig. 2.10a.

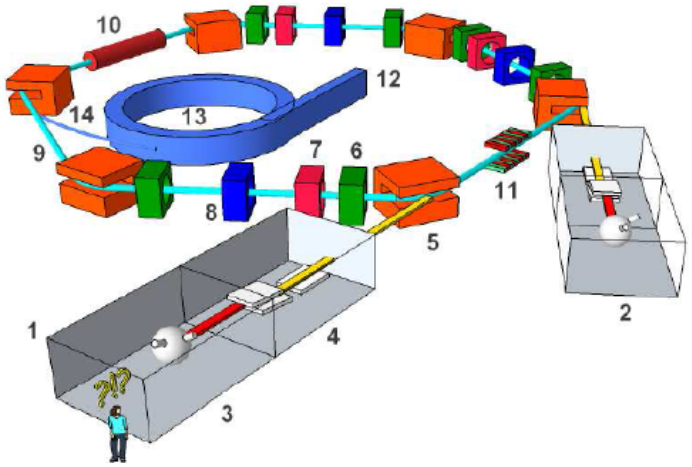

Figure 2.11: Simplified representation of the structure of a third-generation synchrotron; forms, scales and composition are indicative; 1) beamline from undulator ; 2) beamline from bending; 3) experimental hutch; 4) optical hutch; 5) bending magnet; 6) quadrupole magnet; 7)sixfold magnet; 8) magnet steering; 9) vacuum chamber of the storage ring; 10) RF cavity; 11) device insertion; 12) linear accelerator (linac); 13) booster; 14) transfer line.

Thanks to the higher photon flux given off by undulator together with smaller solid angle into which the radiation is emitted the brightness of an undulator beam can be 10^9 times that of a conventional x-ray tube or of a bending magnet. A qualitative comparison of brightnesses of bending magnet, wiggler and undulator is shown in fig.

2.10b.

The places where synchrotron radiation is emitted from the storage ring are connected to the beamlines dedicated and optimized to use it for particular methods. A schematic of a third-generation synchrotron source is in the fig. 2.11. The Elettra - Sincrotrone Trieste S.C.p.A. where some of the experimental data for this thesis were acquired has 28 beamlines with various technique specializations as electron emission, imaging, scattering, reflection/emission, absorption, diffraction and lithography. The machine is equipped by booster which performes the top-up injection of 1 mA every 6 and 20 min in operations modes 2 GeV and 2.4 GeV, respectively. In the following, a brief description of the Elettra beamlines used for his experimental thesis work is provided.

BEAR beamline

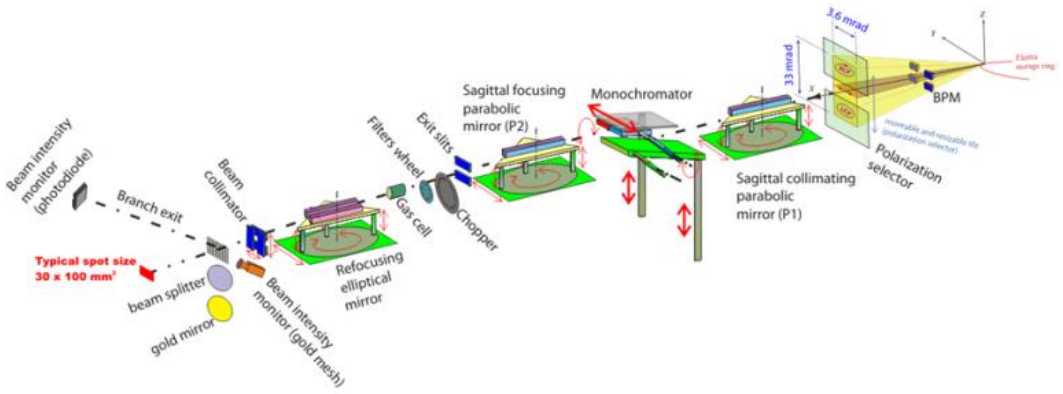

Figure 2.12: Layout of the BEAR beamline [38].

The optical layout of the BEAR beam line is based on the PMGM (Plane Mirror Plane Grating) configuration. Any movement of the beam is monitored by a photon beam position monitor (BPM) installed at the beginning of the beamline (fig. 2.12). After this, the beamline is equipped with a device for selecting the polarization of light (from nearly linear to elliptical). The PMGM configuration is based mainly on a first parabolic mirror, collimating the light emitted by the bending magnet source without any entrance slit, a monochromator working in parallel light at variable deviation angle, a second parabolic mirror focusing the dispersed beam onto the exit slit, and finally an elliptical mirror focussing the beam on the sample. The layout has been conceived to be theoretically aberration free and to have the non plane optics in sagittal focusing. The bending magnet light is collimated on the monochromator by a platinum coated mirror, working in sagittal focusing. The mirror is placed at 12059 mm from the source. Eventual movements of the source are monitored by a Photon Beam Position Monitor. The monochromator is based on two different channels working in parallel

light: the grazing incidence channel working in the 40-1600 eV energy range, and the normal incidence channel working in the 3-50 eV energy range. Both channels are mounted on the same mechanical stage, whose horizontal translation allows to select the different channel. A second paraboloidal mirror P2 collects the radiation coming from the monochromator focusing it onto the exit slits. The divergence of the beam is less than 20x20 (h x v) $mrad^2$. The beam is focused on the sample by an ellipsoidal mirror. The intensity of the light on the sample is monitored on the monitor section.

The experimental apparatus is mainly based on two end stations and the transfer stage. The spectroscopy chamber is mainly dedicated to the synchrotron analysis of samples, the preparation chamber to the preparation of samples. The transfer stage allows to insert samples and to transfer them between the two chambers, always remaining in UHV environment (10^{-10} mbar).

XRD2 beamline

This variable energy beamline (8 to 35 keV) is complementary to XRD1 [39] and is dedicated to high throughput macromolecular crystallography (MX) experiments: large tunable energy range for SAD/MAD experiments, maximal photon flux 2-3 $\times$ 10^{13} , beam size 280 μm $\times$ 292 μm, angular divergence 2.3 mrad $\times$ 0.3 mrad, automated sample mounting in cryogenic environment and high speed large area detector are some of the important features of this beamline.

The XRD2 project is developed in partnership with the Indian scientific community and administered through Elettra and the Indian Institute of Science (IISc), Bengaluru.

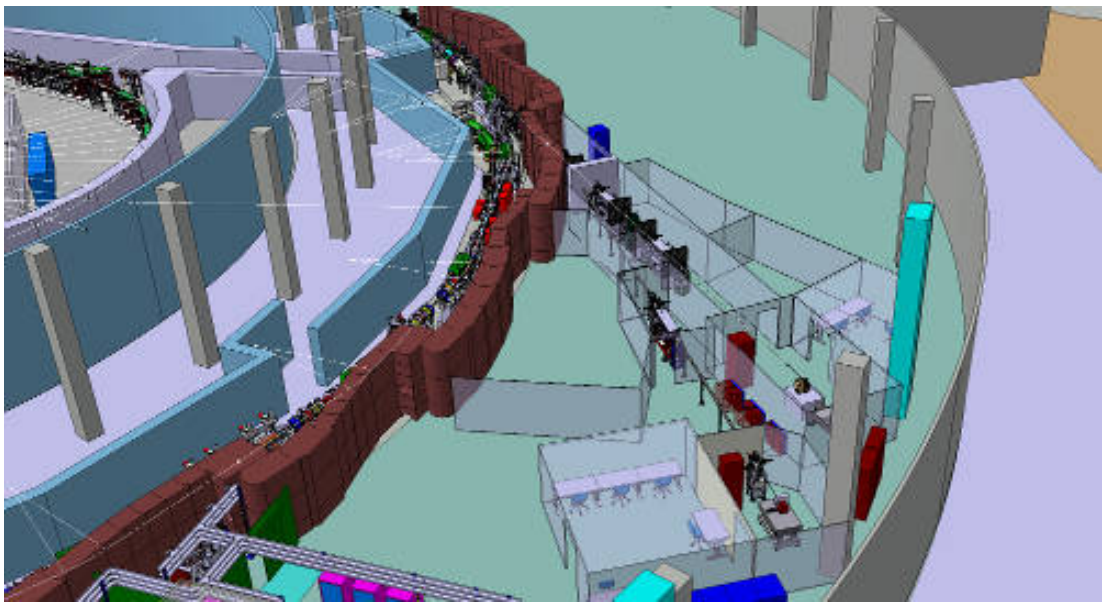

Figure 2.13: Illustration of XRD2 beamline arrangement [40].

3. Preparation and set-ups of experiments

3.1 Fabrication

This chapter is describing the processes of fabrication of SAM-APDs. The process consists, in sequence, of the growth of the structure using MBE apparatus, fabrication of the mesas and placing and bonding sets of devices to the printed circuit board (PCB).

3.1.1 Sample growth

The prototypical epitaxial structure is shown in the fig. 3.1b and in table 3.1. It follows the SAM-APD concept proposed by Capasso at.al. [24], described in section 1.4. The particular modifications to this original structure investigated in this thesis are presented and described in chapter 4.

Growth of the graded composition $Al_xGa_{1-x}As$ layer required special attention, as it would imply a continuous linear gradient of either the Ga or the Al flux. This is not practically achievable by realign the cell temperatures in MBE, especially in the region $x \to 0$. For this reason such layers are grown under the form of a *digital alloy*, where very thin layers of GaAs and $Al_{0.45}Ga_{0.55}As$ are alternating. The thickness of each GaAs/AlGaAs bilayer is constant (in our case 1.5 nm), but the thickness ratio of individual GaAs and AlGaAs in each bilayer is changing so that averaged composition of the bilayer is decreasing stepwise from 0.45 to 0. Since the thickness's are smaller than the mean free path of electrons (aprox. 80 nm [41]) which are being multiplied

Table 3.1: Layer description of grown structure.

Material	x	Dopant	Dopant type	Thickness [nm]	Doping density	Repet.
GaAs		C	p	150	$6 \times 10^{18}\,cm^{-3}$	
GaAs				4500		
δ layer		C	p		$2.5 \times 10^{12}\,cm^{-2}$	
GaAs				35		
$Al_xGa_{1-x}As$	$0 \to 0.45$			20		
$Al_xGa_{1-x}As$	0.45			25		x12
GaAs				35		
GaAs		Si	n	100	$2 \times 10^{18}\,cm^{-3}$	
GaAs (001) substrate		Si	n	5×10^5	$2 \times 10^{18}\,cm^{-3}$	

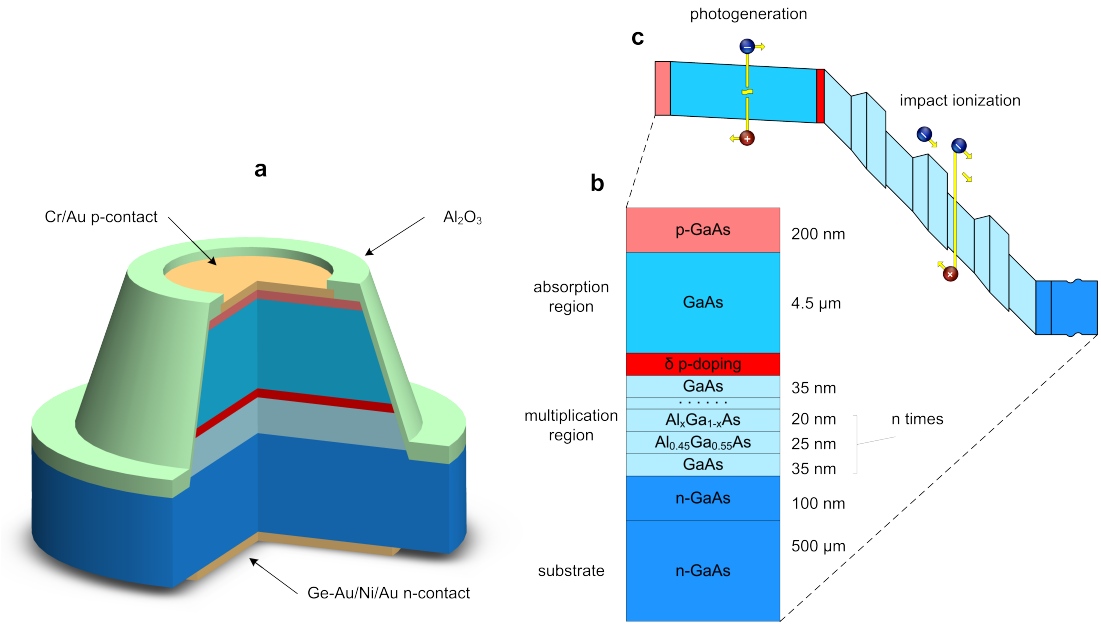

Figure 3.1: Sketch of the fabricated avalanche photodiode with absorption and multiplication regions (a), scheme of epitaxial structure (b) and illustration of working mechanism (c).

in this part of device, the electrons feel the potential of the digital alloy as a constant gradient. Illustration of the digital alloy is in fig. 3.2.

To start the growth, a 2-inch GaAs n-doped substrate is first mounted into a sample holder either by gallium bonding or mechanical fixation, and inserted into a preparation chamber, where it is degassed to evaporate air ambient impurities. Prior to growth, GaAs and AlAs growth rates are calibrated on a dedicated GaAs substrate by RHEED oscillations or reflectivity (section 2.1.3). Typical growth rates are 0.22 to 0.28 nm/sec for GaAs (in the multiplication and absorption layer, resectively) and 0.18nm/sec for AlAs. The wafer to be grown is then than transferred to the growth chamber, where it is heated up to 580 °C in order to remove the surface oxide layer. After this, epitaxial growth starts at the same temperature through a computer-controlled routine:

After the deposition of a 100-nm-thick highly n-doped ($2 \cdot 10^{18}$cm^{-3}) buffer layer onto a (001) n-substrate, a 1 μm thick intrinsic multiplication layer was grown.. This layer includes a staircase structure. Each step consists of 35 nm GaAs, 25 nm $Al_{0.45}Ga_{0.55}As$ and 20 nm of a linearly graded region formed by a digital alloy (where the aluminium content is reduced from 45 % to 1 %). Devices with 12 steps were grown first, following the protocol of [27]. Later also device with 6 and 24 steps were fabricated. Above the staircase structure, a 35-nm-thick GaAs spacer was grown, followed by a δ p-doping layer of carbon atoms. Such layer ensures that after applying a reverse bias the vast majority of the potential drops in the multiplication region (illustrated in fig. 3.1, c). On the top of the delta layer, the intrinsic 4.5-μm-thick GaAs absorption layer was deposited. Finally, the sample was capped with a 200 nm highly

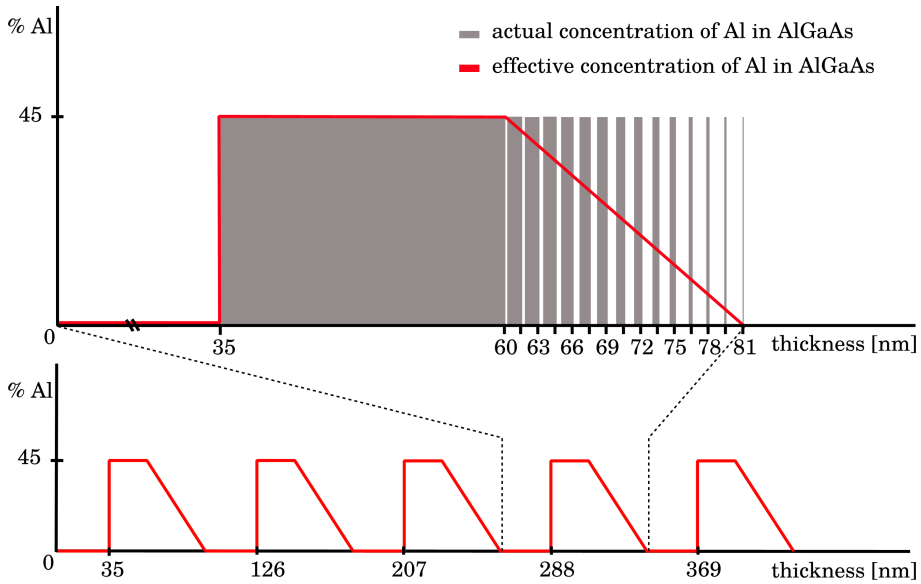

Figure 3.2: Aluminium concentration profile in part of the staircase structure (bottom) and detail of a single step (top). In gray is the actual concentration, in red is the effective concentration i.e. how the electrons percept it.

p-doped ($6 \cdot 10^{18}$cm^{-3}) GaAs contact layer. The overall thickness of the active part is 5.5 μm.

Thickness, composition and uniformity of the layers were assessed post growth by X-ray diffraction. A (004) rocking curve (measured with a high resolution X-ray diffractometer equipped with a four-crystal Ge (220) monochromator, using Cu-Ka1radiation) from a SAM-APD with the structure of Table 3.1 is shown in fig. 3.3 (red trace). Appearance of sharp superlattice interference fringes up to high order confirms the thickness uniformity and interface quality of our layers. An analysis of fringe spacings and of the average alloy composition over a single step gives a step thickness of 80 ± 1 nm and $x \approx 0.47$ for this particular sample.

Hall measurements were performed to calibrate the effective acceptor density. The free carrier concentration at room temperature was measured in a series of bulk GaAs samples containing either a δ (i.e., a 2D sheet of C atoms deposited during a growth interruption of the host GaAs material) or a 50 nm p-doped layer, with different planar densities of C atoms (Fig. 3.4a), obtained by varying the current through the graphite filament of our carbon sublimation source.

The planar density expresses actual 2D density in the case of a δ separation layer. In the case of a finite thickness layer is calculated as an integral of density over the thickness. For example a 50 nm thick layer of C-doped GaAs with acceptor density 5×10^{17} cm^{-3} has a planar density 2.5×10^{12} cm^{-2}. This notation was chosen to make the amounts of acceptors in the two types of separation layers easily comparable. In the following text are the planar densities referred as densities of unit cm^{-2}.

It was found that δ p-doped C layers are highly compensated, likely owing to atom-

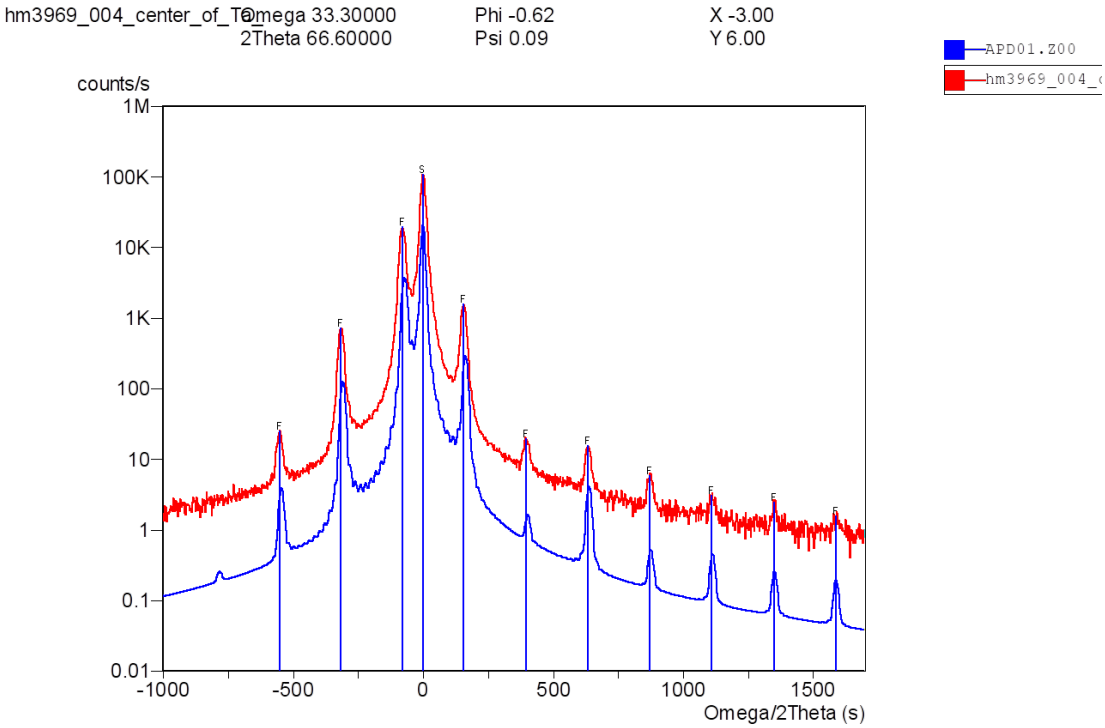

Figure 3.3: XRD spectra of a SAM-APD structure with 12 repetitions in multiplication layer grown on (001) GaAs n-doped substrate.

ic pairing [42]. Compensation takes places in the thin GaAs:C layers as well, although to a lesser extent. Maximum achievable acceptor density in δ p-doped C layers and in the thin (50 nm) GaAs:C layers were 2.5×10^{12} cm^{-2} and 1.2×10^{13} cm^{-2}, respectively (Fig. 3.4b). In the same plot it can be seen that in the δ doping case, the dopant concentration p drops below its maximum by further increasing the source current. To study effects of higher concentration of dopant in the separation layer, the 50 nm thick layers has to be used.

3.1.2 Fabrication of APD diodes

Devices were fabricated in the cleanrooms (CR) of the nanofabrication facility in IOM-CNR, Trieste, Italy [43]. The cleanrooms are of class ISO 3 (maximum 1000 particles/m^3).

After MBE growth, prior to the fabrication, the back side of the wafer has to be cleaned (in case of gallium bonding to the MBE sample holder) and polished (in case of one-side polished wafers). Then the fabrication itself follows.

Mesa litography

First step in the device fabrication is preparation of mesa through a photolithography, as described in 2.2.1. First the sample surface is coated with a photoresist layer

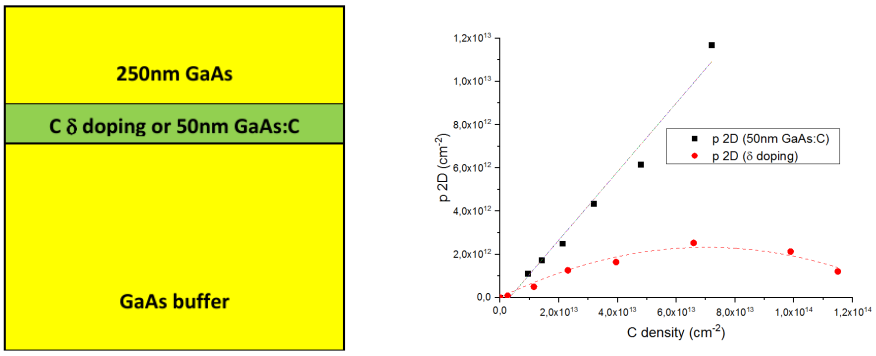

(a) (b)

Figure 3.4: (a) Schematics of the structures used for calibration of the p doping density, (b) acceptor density in the C-doped layers as a function of the 2D density of C atoms, showing that the effective 2D doping density is much lower than the 2D density of deposited C atoms. The dash lines are just to guide the eye.

as follows:

- The sample is placed into the spinner hood where it is first cleaned by acetone and subsequently by isopropanol, applying this solvents on the surface of the spinning sample. Subsequently the sample surface is blown by nitrogen flow.
- The positive photoresist S1818 thermalized to CR temperature is applied to the cleaned surface of the sample by pipette in a homogeneous layer.
- The sample is span for 1 min at the rotation speed 2500 rpm which results in the fininal thickness of the coating about 2 μm.
- After spinning the resist bakeout has to be performed. The coated sample is placed on the hotplate heated up to 115 °C for 1 min.

After the coating with the resist, the sample is going to be exposed for 15 s through photomask using a Suss mask aligner with a mercury I-line of 365 nm. There were several mask designs used during optimisation of the process. The diameter of the mesa for most of the measurements was chosen to be 200 µm. An example of one of the mask designs used for fabrication is shown in fig. 3.5 and the details of the structures are in fig. 3.6.

After the exposition the latent image created in the photoresist by illumination is developed using the MF-322 developer. This first steps are illustrated in fig.3.7 a, b.

Etching mesa

For $Al_xGa_{1-x}As$ the etching solution $H_3PO_4 : H_2O_2 : H_2O$ (3:1:50) is used. The sample has to be submerged in it for a certain period of time taking in consideration that

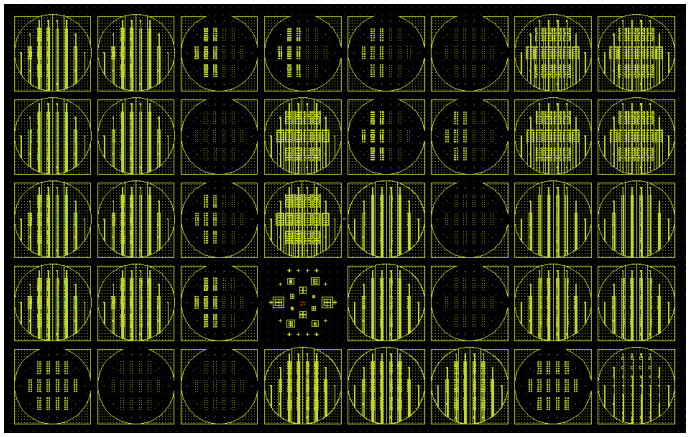

Figure 3.5: The design of one of the photomasks which were used.

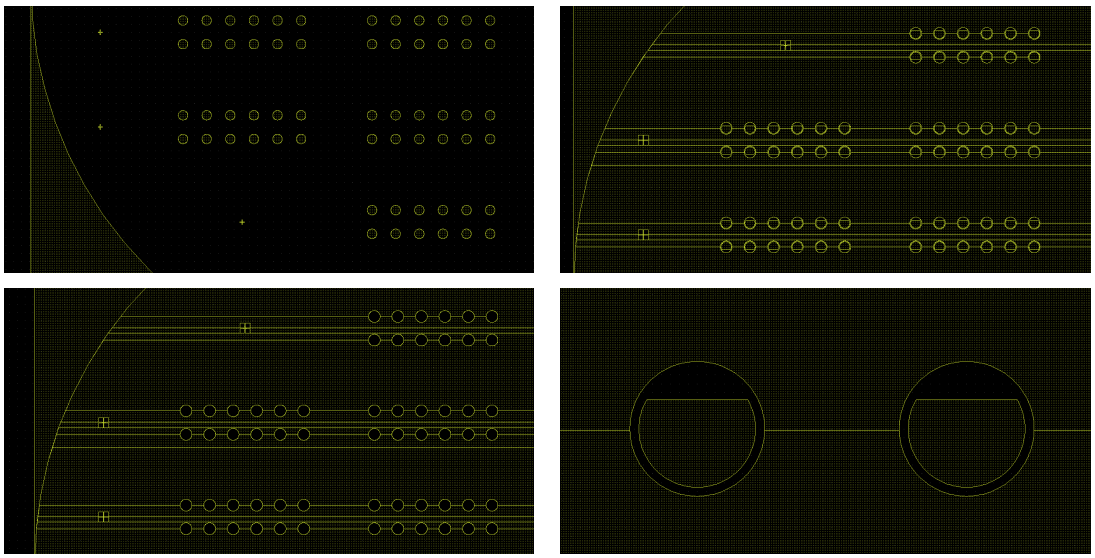

Figure 3.6: Details of the mask shown in fig. 3.5. The mask for mesa etching (top left); structures for lift-off process of opening in the the dielectric layer (bottom left) and for preparation of top p-contact (bottom left for metallization of full circle, top right for metallization with an opening in the center (D-opening)); detail of the D-opening.

the etching rate is approximately 100 nm/min. However, this value is not stable as it depends on the concentration of the peroxide solution (H_2O_2), which is decaying over the time of its storage so its concentration is decreasing. For this reason, a calibration of the etch rate is needed every time. However, in the case of the staircase structure there is one more criterion to estimate the optimal moment for etching to be stopped. An effect of interference on the multilayer staircase structure is employed. At a certain point of the etching process a interference pattern appears on the etched surface. This means, that the etching already reached the multiplication region, which is the last one to be etched. When the interference pattern disappears again it means that the n-substrate has been reached and that the etching process has to be terminated. At this point, the sample is removed from the etching solution and rinsed with water. This

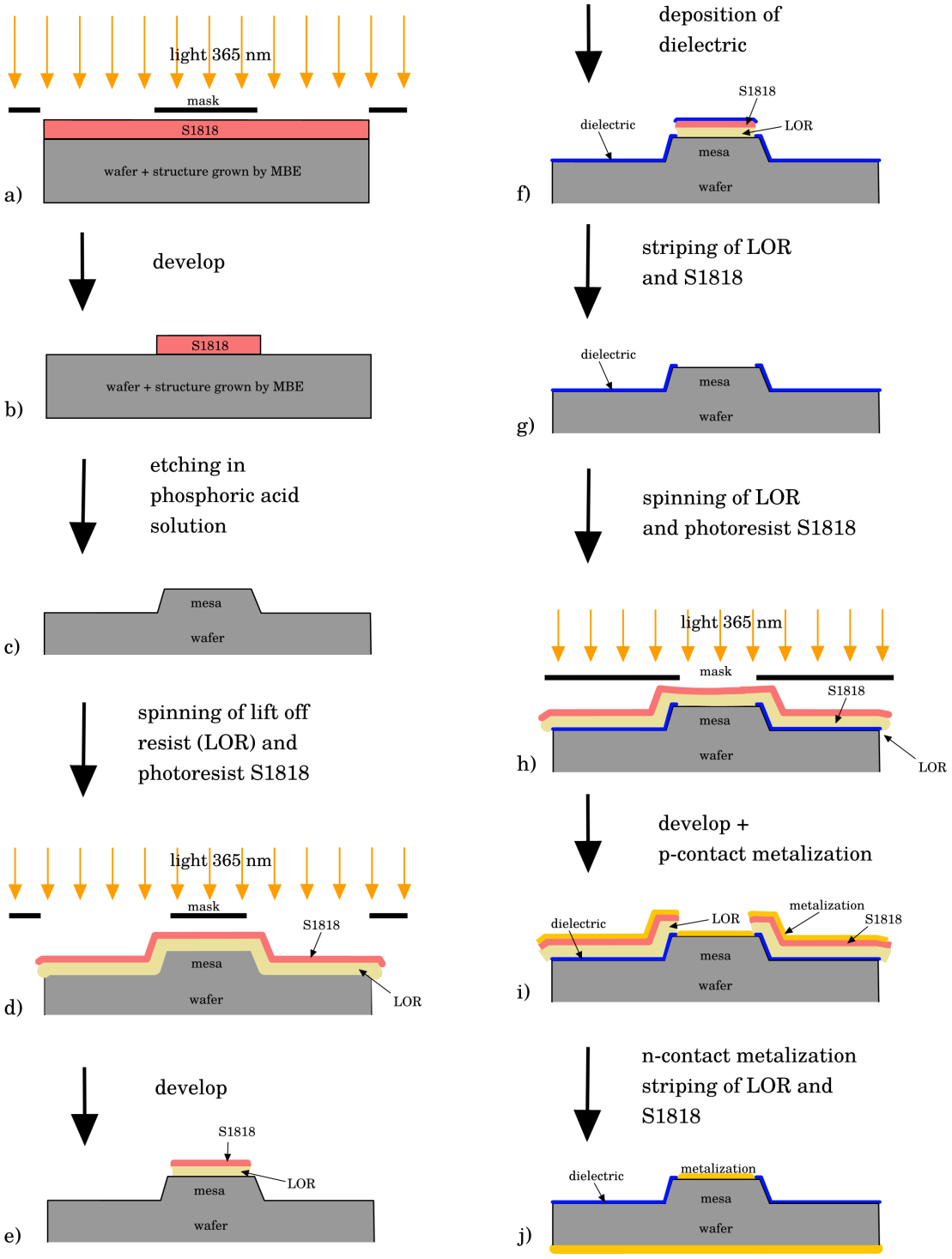

Figure 3.7: The pictorial description of the steps in the fabrication process.

fabrication step is illustrated in fig.3.7c.

Dielectric layer

It is necessary to coat the sample with a dielectric layer to provide an electric isolation of the structures. There are many different types of dielectric layer and many different ways how to prepare them. In the case of silicon the best option is usually silicon dioxide, since it can be grown thermally and such layer has usually very good quality. In the case of GaAs thermal growth is not possible. Two solutions for the dielectric layer have been considered: magnetron sputtering of silicon dioxide from SiO_2 target and e-beam evaporation of SiO_2 and alumina (Al_2O_3). The first option has disadvantage that during the magnetron sputtering, the tool dedicated to this process was heating up above secure temperate after depositing few tens on nanometres of SiO_2. The plasma had to be stopped for at least 5 min and only then the process could continue. This was causing bad quality and low reproducibility of layers prepared in such way. Therefore, the second option has been selected. By e-beam evaporation of of both SiO_2 and Al_2O_3 layers of 250-500 nm thickness can be prepared in continuous process. However, in the case of SiO_2 a creation of defects was observed (fig. 3.8a,b) unlike in the case of Al_2O_3 layers (fig. 3.8c).

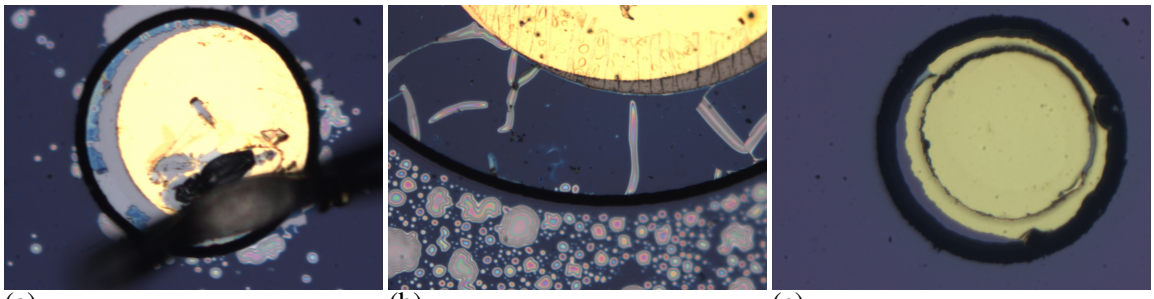

(a) (b) (c)

Figure 3.8: bonded device with SiO_2 as passivation layer (a) detail of defects created in the SiO_2 layer on the device (b) device with Al_2O_3 passivation layer (c)

The deposition of dielectric is preceded by lift-off lithography. The lift-off resist LOR-3B and photoresist S1818 are used. The coating by LOR-3B has the same procedure as the one of S1818 described above, except the spinning speed and bake out which are in the case of LOR-3B 2500 rpm and 180 °C for 5 min respectively.

The resist needs to coat the sample everywhere except the top part of mesa where an opening is left to allow the photon beam to enter to the device. For this reason we use a mask which leaves covered by the resist just a circular part on the top of the mesa. (fig. 3.7 d,e).

After the lithography and immediately before the dielectric deposition an oxygen cleaning is performed.

After the dielectric deposition (fig. 3.7 f)both the resists are striped, first with acetone to strip photoresist S1818 and then with MF-developer to strip LOR-3B. After the resist strip the sample is in the stage depicted in the fig. 3.7 g.

Metal evaporation

A multilayer of upto 4 different metals can be grow without breaking the vacuum in the e-beam evaporator of the IOM-CNR nanofabrication facility.

P-contact metallization: Prior to the evaporation of metal contacts the lift-off lithography is performed, same as for deposition of dielectric layer. This is in order to create the p-contacts just in the circular area on top of the mesas.

Since the devices are made to be used in the reverse bias mode, the ohmicity of the p-contact is not crucial. Even if the contact were rectifying, in the operational mode the device would be connected to the circuit in the open direction.

For this reason we are using a very simple coating composition: 5 nm of chromium for better adhesion of a subsequent gold layer of 50 nm.The process of p-contact creation is illustrated in fig. 3.7 h,i.

Two different types of mask were used to create a top metallization. First, the full area of the opening was covered by the metallization (mask detail in fig. 3.6 bottom left). Later a design of so called D-opening was prepared, where a blank area in D-like shape (to leave one part of the metallization with a big enough area for the wire-bonding) was left on the top of mesa. This design improves significantly the behaviour of the device for low energy photons as shown in section 4.2.3 for green laser, since it increase the fraction which reach the absorption region and create the charge carriers to multiply.

The two resists of lift-off lithography are left on the sample even during the next step in order to protect the front side during the process.

N-contact metallization: Unlike for the p-contact metallization the composition of the n-contact has to be selected in a way that an ohmic contact is created. In fact, the n-contact is in the operational mode of the device, connected so that it would be used in closed direction. In literature [44] multilayer of GeAu (eutectic alloy)/Ni/Au was suggested to obtain well performing ohmic contacts on n-GaAs. The ratio of the thickness of GeAu and Ni layer should be between 4 and 5 to obtain the optimal behaviour of the contact [45].

The n-contact metalization doesn't need to be performed with a mask because it is done on the whole back of the sample. After deposition of the multilayer GeAu/Ni/Au of respective thickness's in nanometres 40/10/50 the resists from the previous process

are striped by acetone (to strip photoresist S1818) and then with MF-developer (to strip LOR-3B). After completing this step the sample is in the final stage of the fabrication depicted in fig. 3.7 j.

3.1.3 Placing of diodes and wire-bonding

When fabrication is finished, the wafer is cut to sample sets each consisting of 12 devices. Such device arrays are then glued by conductive paste to the PCB, so that the back side n-contact is connected to the biasing pin of the PCB as shown in the previous chapter in fig. 3.11. The top p-contacts are bonded to the pads of PCB by aluminium wire of thickness of 25 μm(fig. 3.9a,b).

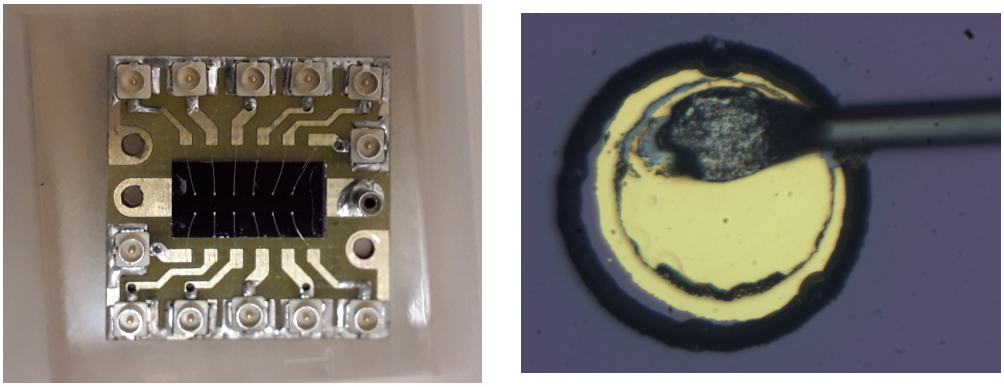

(a) (b)

Figure 3.9: Set of 12 devices bonded on the PCB (a) detail of single device (b).

3.2 Experimental setup for detector tests

In this section the experimental setups of the light sources used for device tests, which are described in the section 2.4, are detailed.

Since the devices had to be tested under several different sources with different purposes, a universal PCB (fig. 3.10) was designed in order to have the device bonded on one board compatible with all the experimental setups. The sets of 12 devices are attached to the center of the board by conductive epoxy glue so that the back n-contact is then connected to the biasing pin (in fig. 3.10c on the right center of the board). Then 12 wire-bondings connect each device with one pad leading to U.FL connector (a miniature RF connector for high-frequency signals up to 6 GHz).

In many setups which were used for the device characterization the UHV compatible stainless housing (fig. 3.11) was used. The stage to which the device is mounted is connected to 2 stepper motors which enable the remote control of x-y movement. The housing includes a flange with 4 SMA connectors (SubMiniature version A semi-precision coaxial RF connectors) which can be connected through coaxial cables to 4

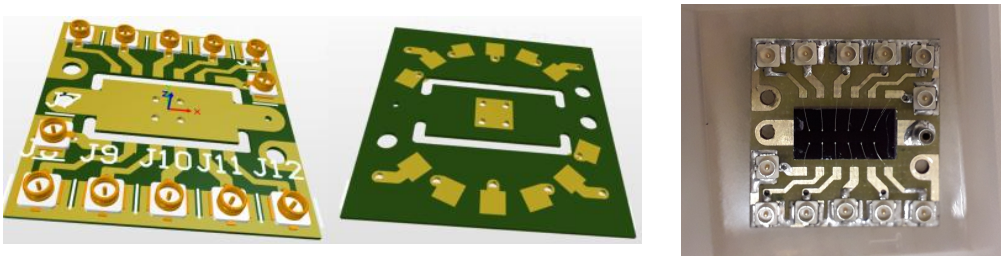

(a) (b) (c)

Figure 3.10: PCB design of the top side (a), back side (b) and PCB with devices bonded on it (c). A pin for connection of bias is at the right center of the picture (c).

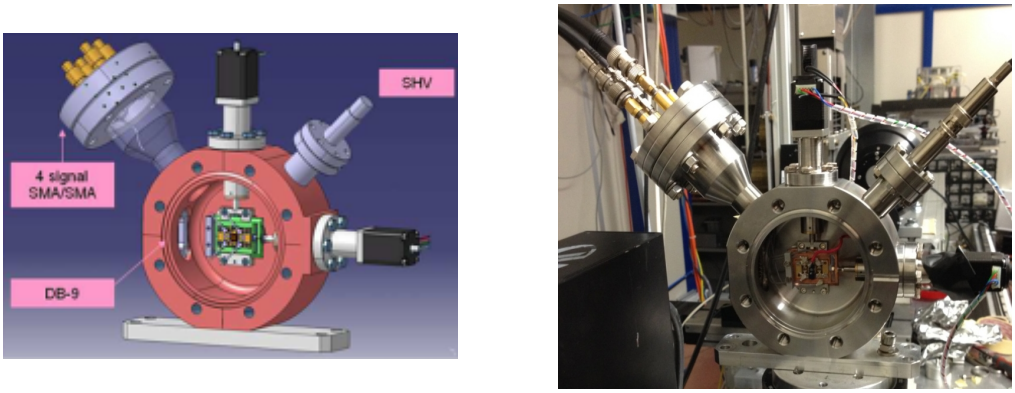

Figure 3.11: Schematic picture (a) and photo (b) of the vacuum compatible stainless housing for detectors.

selected U.FL connectors on the PCB. The voltage is brought to the biasing pin through a SHV (safe high voltage) connector.

There are 2 important quantities being measured in most of the experiments, so we define them here: Measuring the photo-current I_{ph} under the illumination and having measured the dark current I_{dark}, we define net photo-current I_{net} as

$$I_{net} = I_{ph} - I_{dark} \,. \tag{3.1}$$

However, the net photo current (which is carrying the information about internal multiplication) varies with the active area size of the device, intensity of illumination, photon energy and others. To extract information about the internal multiplication, so that it is comparable through different devices under the illumination from different sources, we define the gain M as

$$M = \frac{I_{net}(V)}{I_{net}(V(M=1))} \,, \tag{3.2}$$

where $I_{net}(V(M = 1))$ denotes the value of the net photo-current at the reverse bias voltage at which the device already reached full charge collection but is not yet internally multiplying. In other words, the gain is telling us how many times, in average, is each charge carrier generated by photon absorption multiplied within the device.

3.2.1 Laser setup

As a first light source for the testing of the SAM-APD detectors a green laser was chosen because its photon energy ensures that photogeneration takes place entirely within the absorption region. Section 2.4 reports the parameters of 3 different laser sources which were used in different setups for the device characterization. Here the setup of those experiments are described.

Noise measurements set-up

To extract a quantitative information about the noise related to the multiplication process and consequently to extract the excess noise factor F defined in section 1.4 as a function of the gain M, the setup schematically depicted in fig. 3.12 was assembled. The system is based on a transimpedance amplifier (TIA), which converts the current

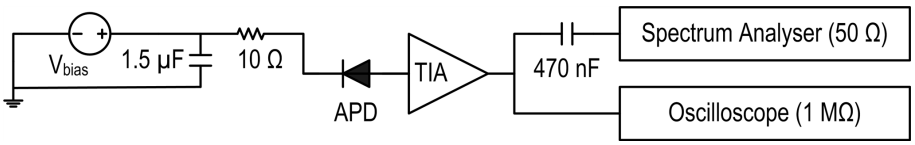

Figure 3.12: The block diagram of the setup for noise measurements.

of the photo-detector into a more convenient voltage signal. In particular, the set-up to measure both F and M was realized by feeding simultaneously the output of the TIA into a spectrum analyser (Agilent EXA Signal Analyzer N9010A) and into an oscilloscope (LeCroy HDO6104), whose input resistance was set to $R_in = 50\ \Omega$ and 1 MΩ, respectively. The spectrum analyser was fore-run by a 470 nF capacitor to avoid any issue with the DC compliance of the instrument input. The TIA features a resistance $R_f = 10\ \text{k}\Omega$ and a frequency cut above 1.5 MHz. The power supply Keysight B2962A was used to bias the devices through a CR filter.

We defined the excess noise factor F of the APD in equation 1.5. Taking into the account that equation 1.5 neglects the dark current, we replace the photocurrent I_{ph} by a net photocurrent I_{net} (3.1) and we write the excess noise factor F as

$$F = \frac{\langle i^2 \rangle}{2eI_{net}(V(M=1))\langle M \rangle^2}\,. \tag{3.3}$$

Now we need to plug into this equation the quantities which we acquire with the described setup. The mean values of the net photo-current and of the gain are obtained from the signal of the oscilloscope - after dividing the acquired voltage by the resistance of TIA we obtain the photo-current which after subtraction of dark current give us the net photo-current. The gain M is then given by the net photo-current through the equation 3.2. To access the mean value of the power of the noise of the device

$\langle i^2 \rangle$ we use the power of the noise S_{iiph} measured by spectrum analyser, which is the power of the noise of the total signal which is being acquired including the noise of the instrumentation. The floor of this noise S_{ii00} given by this instrumentation has to be therefore subtracted to get $\langle i^2 \rangle$. Then the excess noise factor F can be written as

$$F = \frac{S_{iiph} - S_{ii00}}{2eB\frac{R_f^2}{R_i n}\frac{I_{net}(V)^2}{I_{net}(V(M=1))}}, \tag{3.4}$$

where B is the resolution bandwidth of the spectrum analyser.

For these measurements the device was kept in the UHV compatible chamber described at the beginning of this section. However the measurements where not carried out under vacuum, the easy mounting on a optical table and the possibility of x-y movement control were used with advantage. The continuous table-top laser MILLENNIA (of parameters listed in section 2.4) was used for illumination. A neutral density filter was set on the optical path to regulate the impinging power. A photo of the optical setup and the housing is in fig. 3.13.

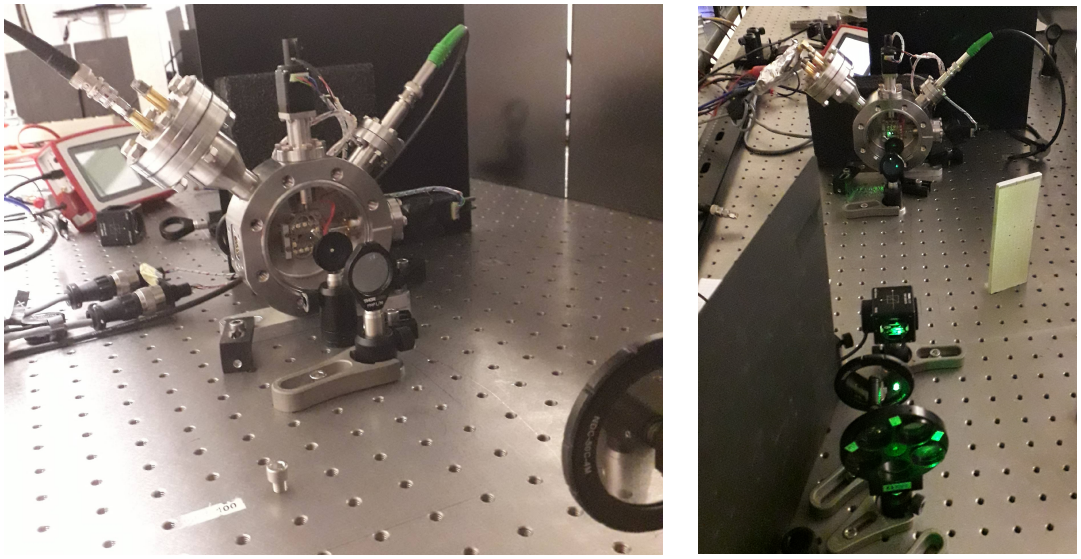

Figure 3.13: Photos of the setup for noise measurements.

Time response measurement setup

The time response of the devices was tested under the laser sources. The device was biased through the power supply Keysight B2962A and CR filter. The aim of the measurements was to record the response of the device to the ultra-short laser pulses (10 ps). The signal of the device was read out by the oscilloscope (Tektronix DPO71254C) through 1 dB attenuator. The oscilloscope has an analogue bandwidth 12.5 GHz with sampling frequency 50 GS/s.

The devices were tested with the ytterbium doped fibre laser, whose parameters are

listed in section 2.4. The optical arrangement and housing of the devices was identical to the one for the noise measurements.

Spectroscopic measurements setup

The preparation of this setup for spectroscopic measurement aims at the final target of resolving the K-beta from the K-alpha lines of Fe-55 spectra, 6.49 keV and 5.9 keV respectively. Considering pair generation energy $\varepsilon = 4.2$ eV [46], the separation of these two lines is expected to be in order of one 100 electrons. Considering a modest value of the internal gain of the device to $M = 10$, the rms noise should be around 1000 electrons, to be able to distinguish these two energies.

Because of this requirement we have decided to use, as central component of our analogue electronics, the CUBE - a charge sensitive amplifier (CSA) developed by XGlab for radiation detectors. The model PRE 039 which is the most compatible with the SAM-APD here reported (designed for devices with a capacitance 3 - 10 pF) has an equivalent noise charge (ENC) of 20.2 e^- at 1 µm [47]. A dedicated PCB was designed (fig. 3.14a) where the CUBE was wirebonded as shown in fig. 3.14b.

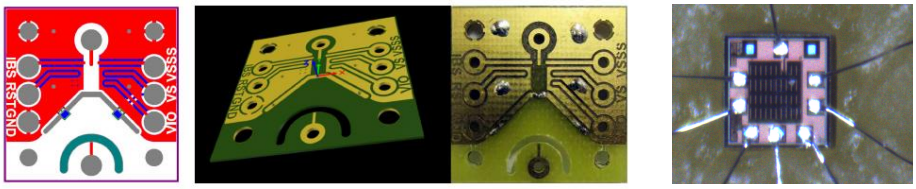

(a) (b)

Figure 3.14: PBC dedicated to accommodate and connect the CUBE to the rest of the electronics (a) microscope view of the bonded CUBE (b).

The measurement setup (fig. 3.15) consists of a low-noise power supply (Keysight B2962A), the main board where the PCB with the device was mounted together with the CUBE PCB, the CSA bias board, a shaper and an oscilloscope (LeCroy HDO6104, analogue bandwidth 1 GHz, sampling frequency 2.5 GS/s).

Preliminary measurements, focused on the setup testing were performed so far. A pulsed table top laser of wavelength $\lambda = 540$ nm of pulse width 100 fs was used for this purposes to emulate high energy photons.

3.2.2 Synchrotron beamline setup

BEAR beamline

An additional PCB was designed in order to interface the sample holder on the BEAR beamline adapted to the load-lock system of UHV chamber and to ensure com-

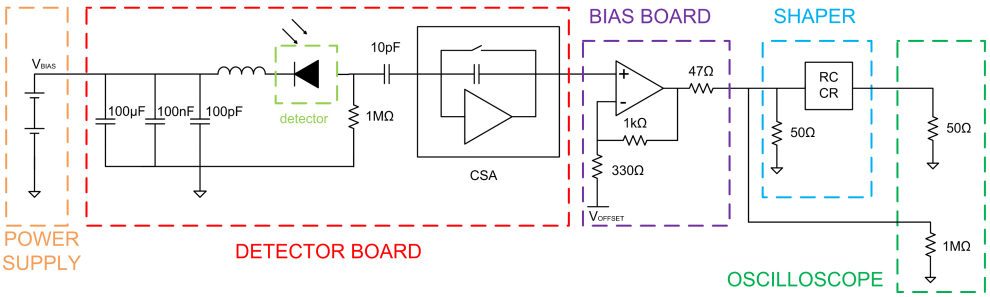

Figure 3.15: Block diagram of the setup for the spectroscopic measurements.

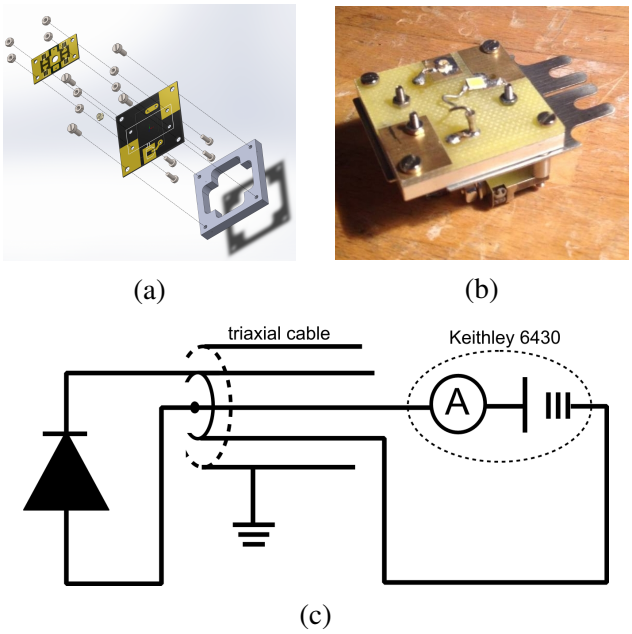

(a) (b)

(c)

Figure 3.16: Design (a) and illustrative photo (b) of the PCB prepared in order to interface the sample holder used at the BEAR beamline and the PCB used to carry the devices.

patibility with the PCB on which the devices are bonded. The design picture and an illustrative photo are shown in fig. 3.16a,b.

The measuring circuit (fig. 3.16c) was designed to ensure that no drain currents originating from surface charge compensation that has high probability at this photon energy (500 - 1000 eV), will be summing up with the photo-current from the device. As power supply and amperometer Keithley 6430 was used.

XRD2 beamline

For tests under X-ray illumination the same PCB with the devices as for the noise measurements was mounted on the UHV-compatible chamber, which was placed downstream in the focal plane of the XRD2 line. The photocurrents generated in the devices were measured by utilizing the aforementioned picoamperometer AH501. Also in this setup the power supply Keysight B2962A was used to bias the devices through CR

filter.

4. Results and discussion

In this chapter the experimental results and their discussion are described. The experiments carried out in order to optimize the doping concentration in the p-doped separation layer are presented and discussed in Section 4.1. The influence of the number of steps in the multiplication region on the APDs performance is shown in Section 4.2. In particular, noise measurements, time response and spectroscopic measurements will be presented. Finally, in Section 4.3 the response of the devices to hard X-ray irradiation is shown.

4.1 Delta doping concentration effect

As suggested in section 1.5, the p-doped separation layer plays a key role in functionality of the SAM-APDs. For this reason we performed experiments focused on effects of the doping level of this separation layer.

We calibrated the effective acceptor density as described in section 3.1.1. It was found that δ p-doped C layers are highly compensated, likely owing to atomic pairing [42]. To study effects of acceptor concentration in the separation layer higher than $2.5 \times 10^{12}\,\mathrm{cm}^{-2}$, we had to therefore employ the 50 nm thick GaAs:C layers. Compensation takes places in such thin GaAs:C layers as well, although to a lesser extent. Maximum achievable acceptor density in δ p-doped C layers and in the thin (50 nm) GaAs:C were 2.5×10^{12} cm^{-2} and 1.2×10^{13} cm^{-2}, respectively. In the δ doping case, the dopant concentration p drops below its maximum by further increasing the source current.

We studied the effects of acceptor concentration on the prototypical SAM-APD structures consisting of a 4.5 µm-thick absorption region and a multiplication region made of 12 steps (see fig. 3.1 [11, 13]). Concentration was changed in the range $8.8 \times 10^{10}\,\mathrm{cm}^{-2}$ $6 \times 10^{12}\,\mathrm{cm}^{-2}$ and a set of six samples (see table 4.1). Samples A to E were delta-doped, while the in the with the highest density (F) the 50 nm GaAs:C layer was used.

Table 4.1: Areal acceptor densities in the δ (A-E) and 50 nm thick (F) p-doped layer as measured with Hall effect

device	A	B	C	D	E	F
density [cm^{-2}]	$8.8 \cdot 10^{10}$	$5.0 \cdot 10^{11}$	$1.3 \cdot 10^{12}$	$1.6 \cdot 10^{12}$	$2.5 \cdot 10^{12}$	$6 \cdot 10^{12}$

4.1.1 Characterization in dark

The devices were first tested in dark by measuring their current-voltage (IV) and capacitance-voltage (CV) characteristics. The IV measurements allow us to select devices with the lowest leakage, while the CV measurements provide information about the electric field and potential distribution inside the device. In particular, we studied the effect of the acceptor concentration in the δ p-doped layer on the CV characteristic.

As we said in the introduction, we are aiming to keep the absorption region without strong electric field and we want most of the potential drop to happen in the multiplication region. In other words, we want mainly the multiplication region to be depleted.

The left part of fig. 4.1 shows the capacitance per area as a function of the applied voltage, while the right part shows the depletion width calculated from the $C(V)$ according to the equation 2.4.

It can be seen that for the two highest carbon concentrations (samples E and F) the capacitance keeps constantly high over the entire range of the reverse biases, up to the breakdown voltage which was evaluated by measuring dark IV characteristics. Example of a typical dark current density is in fig. 4.2. In these conditions, the depletion width corresponds to the thickness of the multiplication region. This means that this amount of carbon atoms is able to prevent the formation of a large electric field in the absorption region by confining the main drop of the applied potential inside the multiplication region.

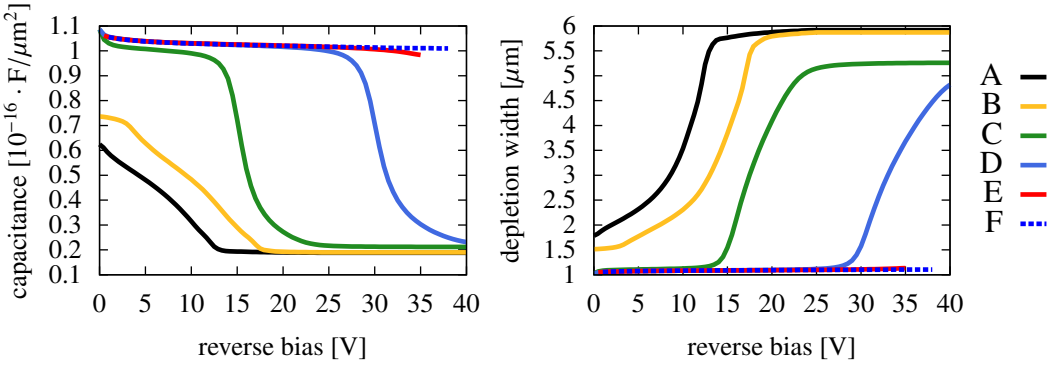

Figure 4.1: Capacitance (left) and corresponding depletion width (right) versus reverse bias for the different devices.

Conversely, in the samples with lower doping levels the capacitance starts to drop at a certain bias, meaning that the applied potential starts to deplete beside the multiplication region also the absorption region. In particular, the depletion region of most of the devices with lower doping reached at some voltage a depletion width of 5.5 μm, which is the full thickness of the grown structure confined within the n-p contact layers. The voltage at which this drop occurs increases with the doping dose in the δ p-doped layer. To confirm this interpretation, we reproduced the CV curves of samples C, D, E and

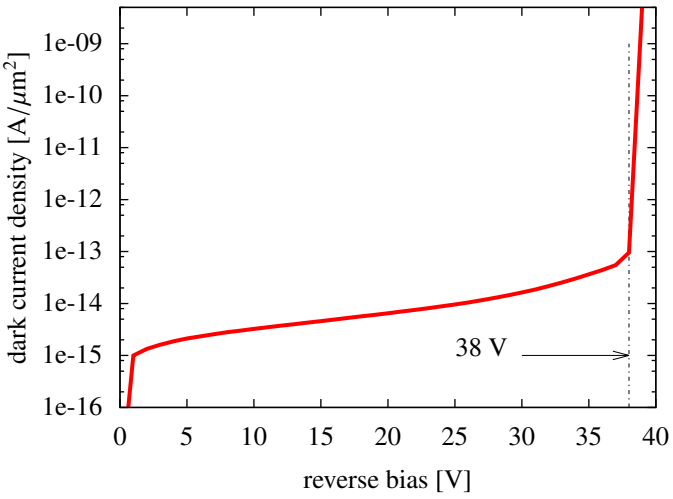

Figure 4.2: Typical dark current density values showing the break down voltage at 38 V.

F with TCAD simulations [48–50]. Fig. 4.3 shows that experimental and simulated data are in good agreement; in particular, the concentration of acceptors in the p-doped separation layer obtained from simulations fairly approximates the values measured by Hall effect (tab. 4.1). The background doping in the absorption region that best fits our experimental CV curves (around 5×10^{14} cm^{-3}) is in qualitative agreement with the fact that MBE-grown GaAs layers have generally a low residual p-type doping in the $10^{13} - 10^{14}$ cm^{-3} range [51], although it seems slightly overestimated.

Fig. 4.4 shows the band profiles simulated at different biases with sim32 software [52] for samples A, C, E and F to illustrate the dependence of the band profiles throughout the absorption and multiplication regions on the acceptor level in the p-doped separation layer and on the applied bias from zero up to breakdown voltage. At 0 V the valence band is completely pinned at the Fermi level in correspondence of the p layer for devices C, E and F. However, for device A pinning is incomplete, which means that the inbuilt potential slightly depletes the absorption region even in the absence of an external bias. This explains why the CV characteristics (fig. 4.1) of the devices with low doping do not start at a capacitance value corresponding to a 1 μm-thick depleted zone (i.e. the multiplication region), but they are affected by the partial potential drop in the absorption region already at 0 V bias. This effect is more evident with 1 V external bias: while in devices C, E and F the band profile in the absorption region still keeps flat , in device A it starts to deplete significantly. At a reverse bias of 20 V device A is fully depleted including the absorption region. At this voltage a slight slope of the band profile in the absorption region of device C indicates that is starts to deplete in this device too, while for devices E and F it is still flat. At 33 V device C is almost fully depleted , with a significant potential drop in the absorption region, with

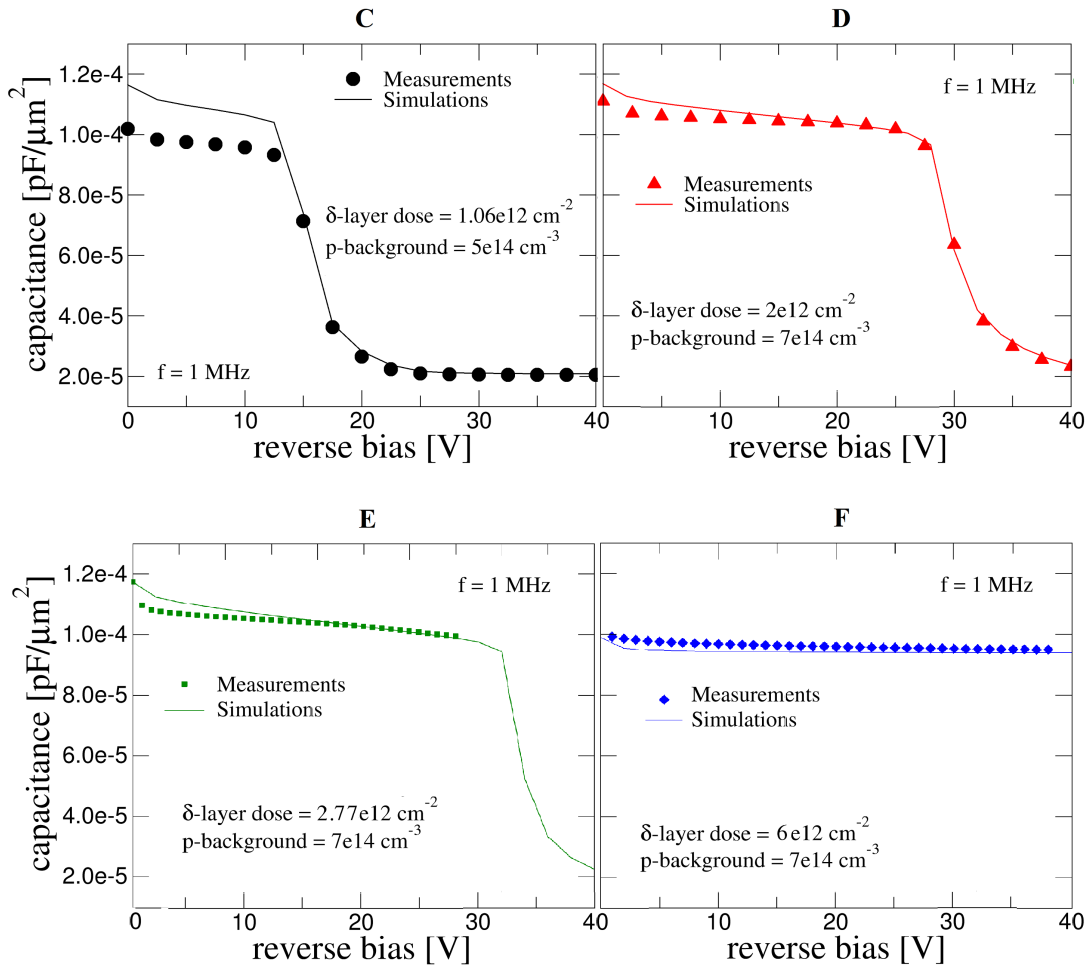

Figure 4.3: Comparison between experimental and simulated CV curves. In the simulation the δ-layer dose is equal to the actual concentration of acceptors put in the sample, while the p-backgrounds is the residual acceptor concentration present in the absorption region.

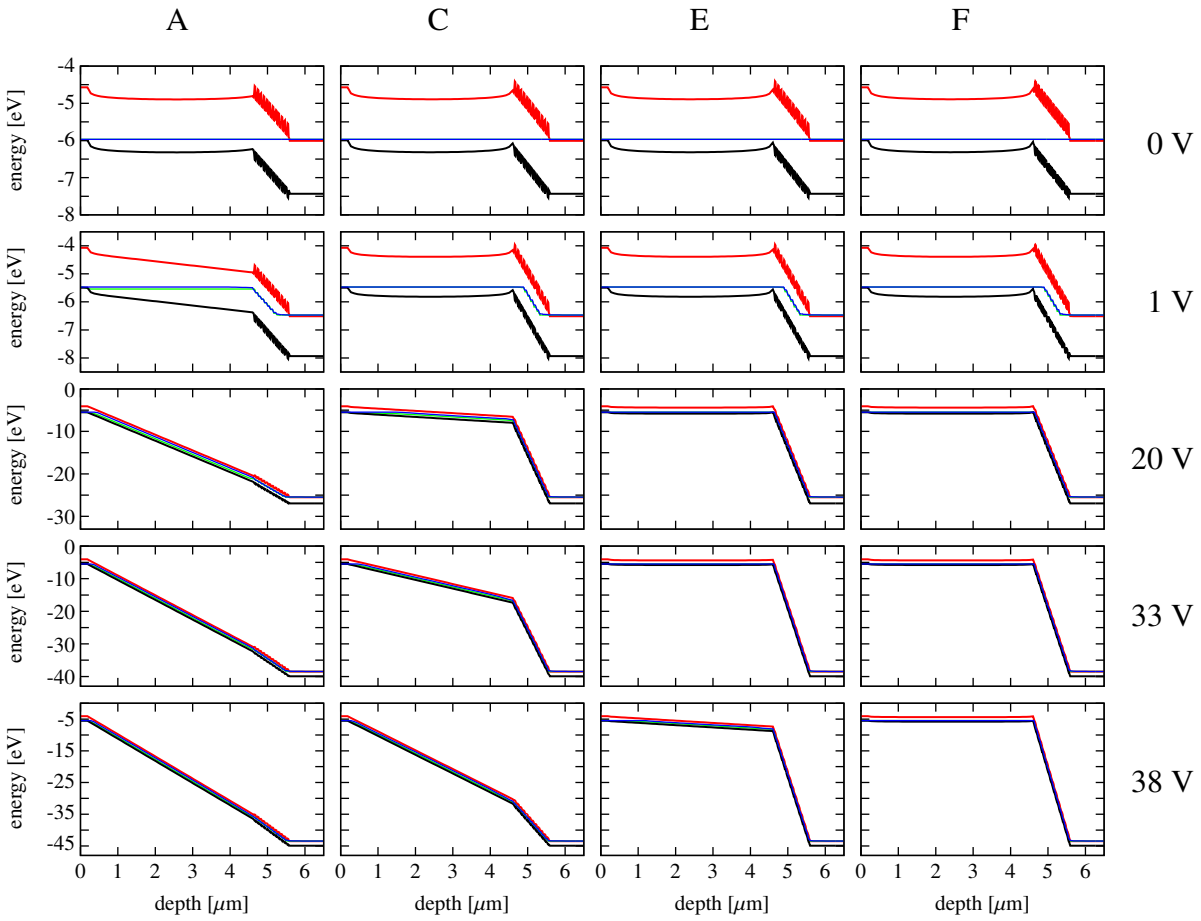

Figure 4.4: Band diagrams of devices A, C, E and F for 5 different reverse biases. Conduction band (red), valence band (black), electron and hole quasi-fermi levels (green and blue).

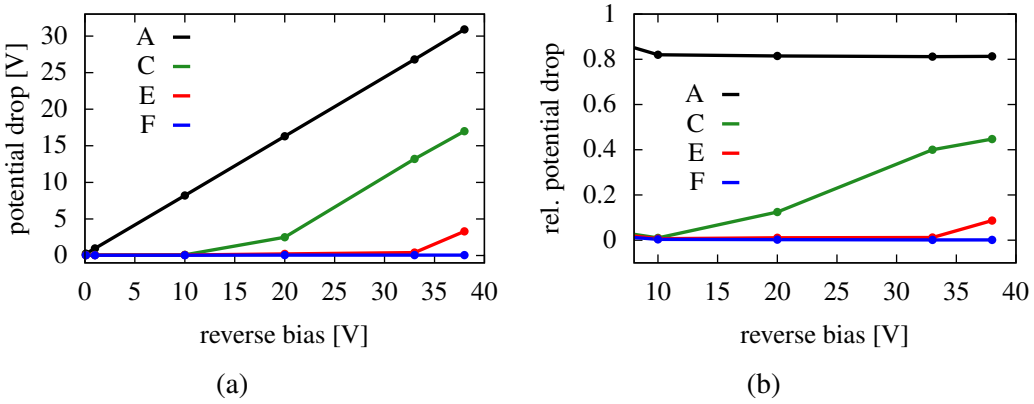

(a) (b)

Figure 4.5: Values of voltage drop (a) within the absorption region as function of reverse bias voltage and this drop as a fraction of the applied bias (b) for devices A, C, E and F.

devices E and F still keeping this region flat. Finally, at breakdown voltage (38 V), a very small potential drop is observed even in the absorption region of sample E, while flatband condition is maintained only for sample F.

To quantify the depletion of the absorption region, we have plotted in fig. 4.5a the potential drop between the top p contact and the p separation layer as a function of the reverse bias, as they result from the simulations. For device A this drops increases linearly with the bias starting from 0 V, which means that the doping of the separation layer is ineffective in shielding the external bias at all voltages. For device C the drop is zero up to a value between 10 and 20 V suggesting that the effectiveness of the p-doped layer disappears at this voltage. Finally, for devices E and F there is no potential drop in the absorption region for all the biases, except for a small increase in device E close to breakdown. Fig. 4.5b shows these voltage drops as a fraction of the applied bias, i.e., the portion of total voltage which is distributed within absorption region.

The influence of the small difference in band profiles of devices E and F on the high-bias capacitance can be also appreciated with a closer look at the CV curves of samples E and F. Data for these two samples taken from fig. 4.1 are shown again in fig 4.6. It can be seen that the CV profiles coincide up to about 25 V, above which a small but appreciable capacitance drop is observed for sample E. This corresponds to an increase of about 40 nm in the depletion width, with respect to sample F.

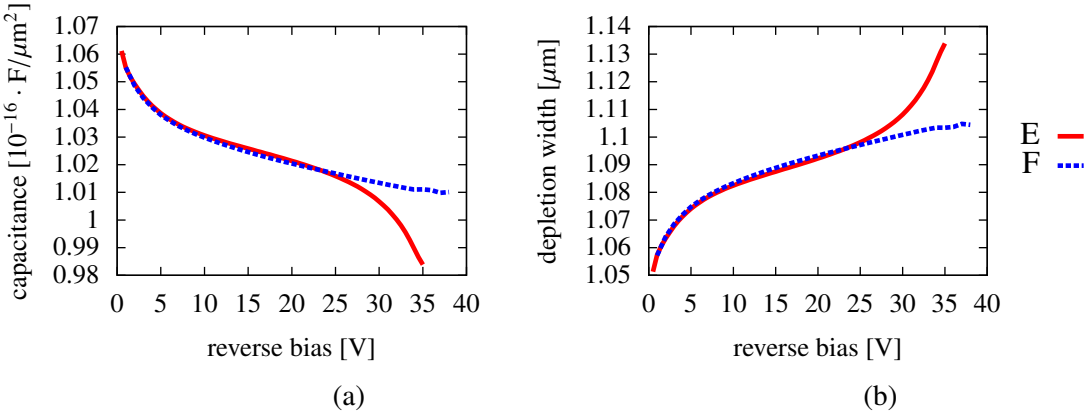

Figure 4.6: Experimental CV characteristics (a) of samples with δ separation layer of acceptor density of 2.5×10^{12} cm^{-2} (E) and 50-nm separation layer of acceptor density of 6×10^{12} cm^{-2} (F) and their respective depletion width (b).

The shape of the CV curves in fig. 4.6 can be used to calculate the profile of dopant concentration inside the device, $N(d)$, by using the equation for general nonuniform distributions [53, 54]

$$\frac{d(1/C_A^2)}{dV} = \frac{2}{e\varepsilon_r\varepsilon_0 N(d)} \tag{4.1}$$

where C_A is the capacitance per unit area of the mesa, V is the applied bias and q is the elementary charge and d is the depletion width, related to C_A through the data of fig. 4.6. Since we are probing values of d in the proximity of the depletion width, we are sensitive to the charge distribution around the p-doped layer. From these analyses (fig. 4.7) it follows that in the case of the 50-nm separation layer (F) the dopant

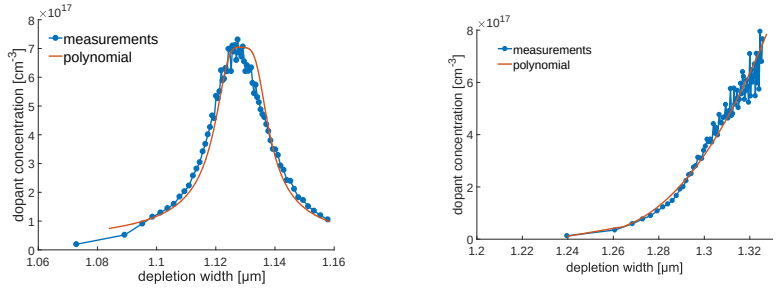

(a) (b)

Figure 4.7: Dopant concentration profile as a function of depletion width for devices E (a) and F (b). The blue dots represents the measured values, while the red continuous curve are the results of a polynomial fit of the inverse of the capacitance optimized with the least squares method, both obtained by using Equation 4.1. The fitting polynomials were introduced in order to obtain (after differentiation) noiseless reference curves which show the profiles also where the measured data becomes noisy.

concentration as a function of the distance below the junction between the p-layer and the intrinsic layer (which corresponds to the depletion region) grows monotonically. This trend testifies how the layer shields the absorption region in a way that the field has no measurable effect beyond the p-layer, at least within the voltages of operation. On the other hand, in the δ case the carrier concentration has a bell shape due to the drop in capacitance, which starts to occur in the devices with a just sufficient carbon concentration (E), meaning that in this case we start depleting beyond the δ–layer in the absorption region, as seen in fig. 4.6 b above.

4.1.2 Response to the light

Selected devices were tested under light to assess their response to incoming photons. Two different light sources were used: the IOM-CNR BEAR beamline at the synchrotron Elettra (Trieste, Italy) in the energy range 500-800 eV and a green (λ = 532 nm) tabletop laser. Both sources and measurement setups are described in the section 2.4 and 3.2.

For both light sources, dark current and photocurrent were measured as a function of the applied reverse bias. The net photo-current was calculated as the difference between these currents. To compare the response under different light sources and different fluxes, the gain was defined as the signal normalized by its value at 20 V, where multiplication does not take place yet (equation 3.2).

Devices B, C and E were tested at the BEAR beamline. Fig. 4.8 (a) reports the photocurrent for different energies of the beam and the dark current of device E. The plot shows that in the experiments with higher photon energy, the photocurrent is larger. Fig. 4.8 (b) reports the gains calculated from the data plotted in the left part: gains

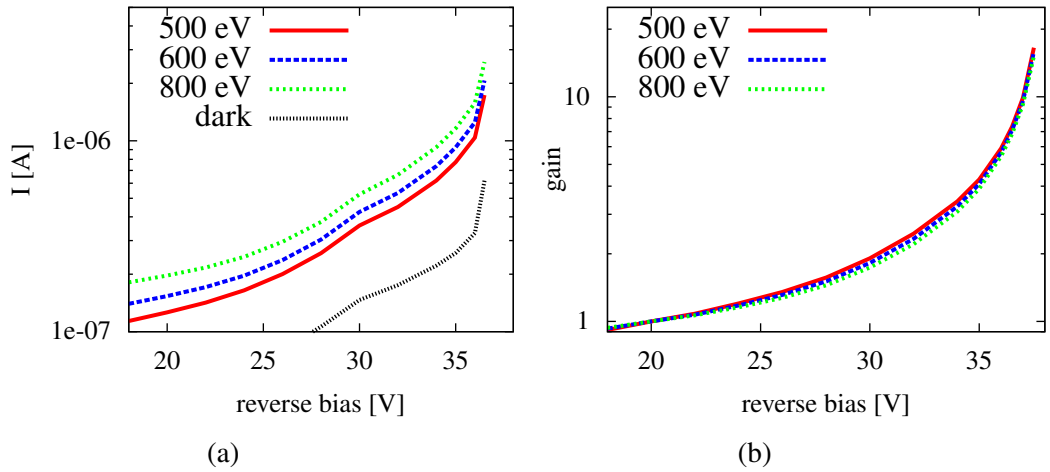

Figure 4.8: Dark current and photocurrent for three photon energies of the BEAR beamline in the 500-800 eV range of device E (a); gain for the same photon energies (b).

for different photon energies are overlapping. This is reasonable since all the photo-generated carriers are created in the absorption region, as mentioned above, and subsequently multiplied in the multiplication region in the same way.

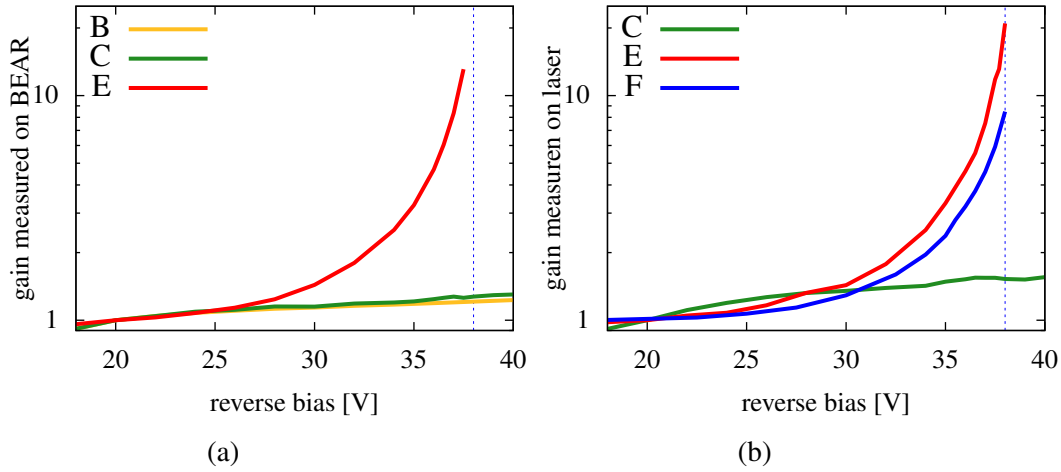

Figure 4.9: Gains of devices with different areal density of the δ p layer measured at the BEAR beamline averaged over seven different energies in the 500-800eV range (a); and with the green laser (b). The brakedown voltage of device E (38 V) is marked by a dashed line.

Fig. 4.9 (a) the gains of devices B, C, E characterized on the BEAR beamline are plotted. Curves are averaged over seven different energies in the 500-800eV range. It can be noticed that the multiplication for the low-doping structures is minimal, while with doping in the device E the multiplication effect is clearly visible and reaches a value of 13.1 at 37.5 V. The gain of the devices C, E and F was measured under laser light. These data (right part of fig. 4.9) show the same behaviour for the device C and

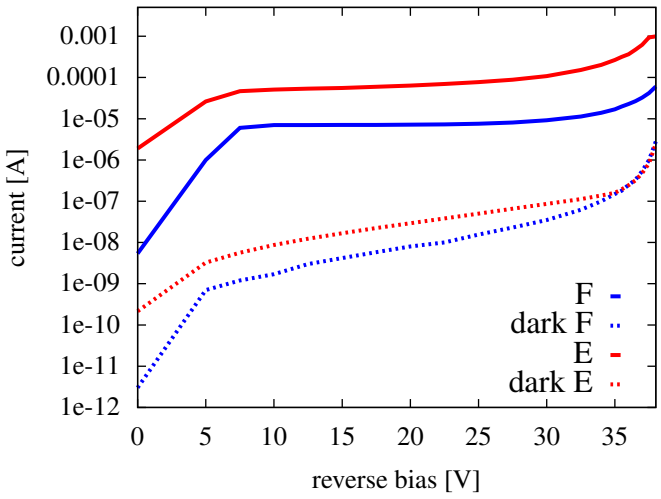

Figure 4.10: Currents for device E (red curves) and device F (blue curves) as a function of the applied reverse bias. The power of the photon fluxes during the acquisition of the photocurrents for E and F were 1400 µW and 1600 µW, respectively.

E as the one observed on the BEAR beamline, with a gain of the device E of 11.8 at 37.5 V and a maximum gain of 21 at 38 V of reverse bias. In the case of device F, we can see that the gain is of 8.5 at 38 V.

The curves of photo-currents and dark currents of samples E and F, as shown in fig. 4.10, reveal that the absolute values of the photocurrent are higher in the case of device E even though the photon flux during acquisition was slightly lower (1400 vs. 1600 µW). This could be explained by the fact that device E has a small residual field in the absorption region whose presence is suggested by the capacitance measurements (fig. 4.6) and simulations (fig. 4.4). This residual field makes the created electrons drift towards the multiplication region, providing a better charge collection above 25 V, where a difference in the CV curves starts to be observed (fig. 4.6). At lower biases, in the absence of this field, the charge carriers move just by diffusion; however even in this regime device F exhibits a smaller charge collection efficiency and subsequently a smaller photocurrent. One additional factor that possible contributes to the charge collection efficiency could be the different potential barrier created by the p-doped separation layer in the conduction band. In fact, it can be seen in the simulated band profiles of fig. 4.11 that for higher p doping (device F) , electrons have to overcome a larger potential barrier with respect to lower doping (E). This can be observed for all biases.

From the discussion above it can be concluded that $2.5 \times 10^{12}\,\mathrm{cm}^{-2}$ doping in δ p-doped separation layer is the optimal one. It is enough to confine the potential drop mainly in the multiplication region and enable in this way the multiplication. At the same time, it appears that, in contrast to higher doping, the depleted region extends

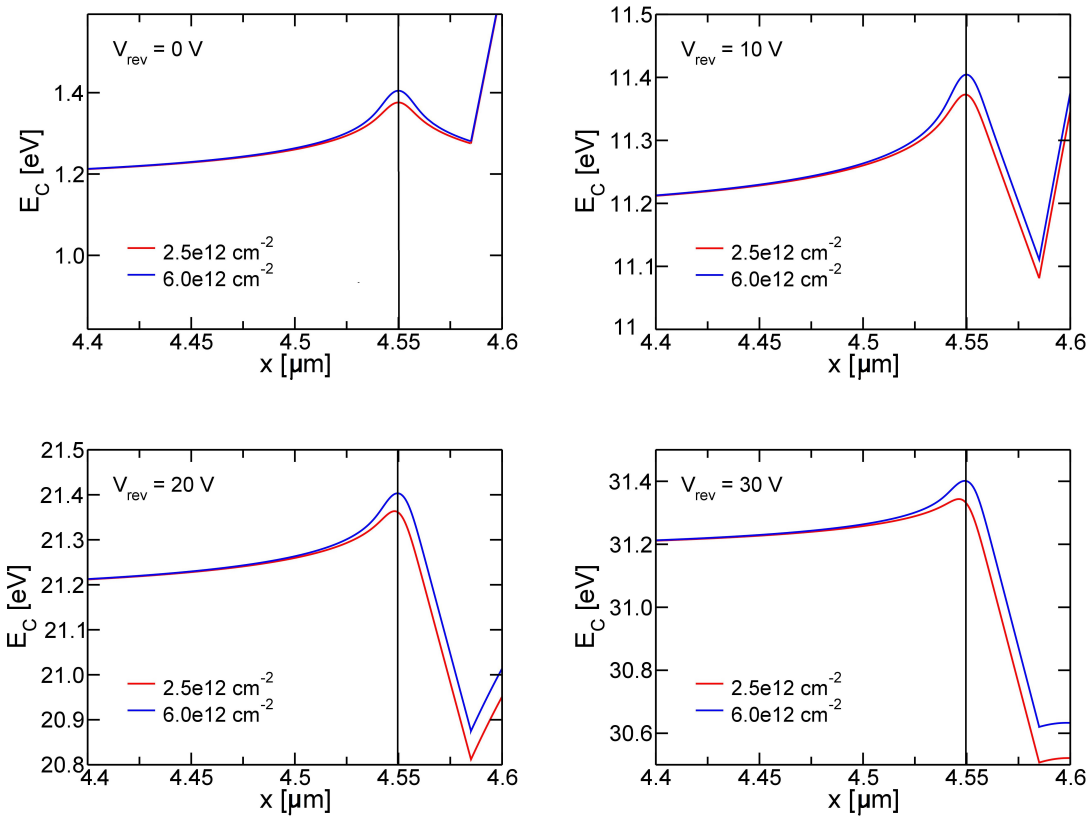

Figure 4.11: Simulated conduction band profile, at different bias voltages, of the SAM-APD device structure in the surrounding of the layer dividing the absorption and the multiplication region (position of the layer is indicated by vertical line). The red curve (device E) results always higher compared to the blue one (device F), which means that the electrons encounter more difficulties in reaching the multiplication region in the first case compared to the latter one.

slightly beyond the p layer for the highest applied biases, creating a mild residual field in the absorption region. This field seems to be beneficial for the collection efficiency of the devices as shown by comparing the absolute values of the photocurrent, while it does not influence significantly the multiplication process. Moreover, the higher concentration results in an obstacle for the electrons which are less likely to reach the multiplication region as shown in fig 4.11. We will employ therefore samples with 2.5×10^{12} cm^{-2} doping density in the experiments presented in the rest of this thesis.

4.2 Variation of the number of steps in the multiplication region

After setting up the optimal separation layer, the focus was put on the influence of other structural parameters on the behaviour of the SAM-APDs. In particular, we studied the variation of the number of the steps in the multiplication region. The sim-

ulations suggested that with increasing number of steps the noise associated to the multiplication, described by excess noise factor F, is lower for a given gain M. Calculations were carried out for devices with 6, 12 and 24 steps in multiplication region (fig. 4.12) by using an energy balance history dependent model (EBHDM) [55]. The same set of devices was fabricated using the δ p-doped separation layer with doping concentration $2.5 \times 10^{12}\,\mathrm{cm}^{-2}$ and mesas of 200 µm in diameter.

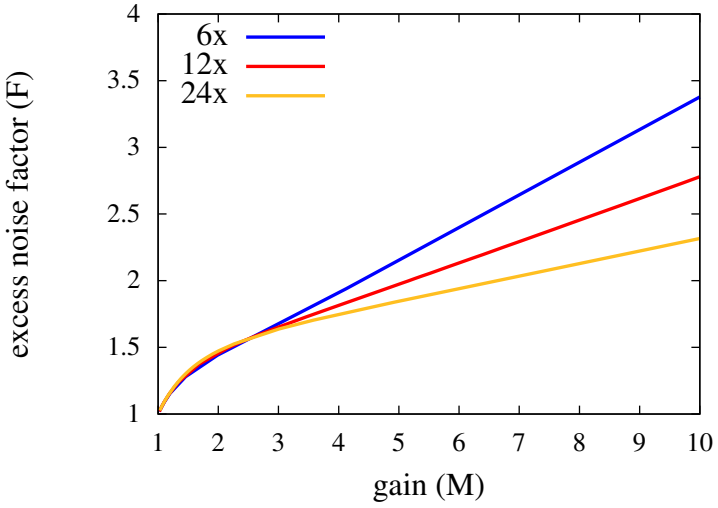

Figure 4.12: Simulated excess noise factor as a function of gain for the SAM-APDs with 3 different numbers of steps in the multiplication region.

4.2.1 Characterization in dark

The tree devices were tested in dark with the setup described in section 2.3. Capacitance-voltage curves per unit area and the the corresponding depletion widths calculated according to the equation 2.4 are plotted in fig 4.13. According to table 3.1 the thickness of one step is 80 nm, meaning that the thickness of the multiplication region for the devices with 6, 12 and 24 step is 480 nm, 960 nm and 1920 nm, respectively. This corresponds well to the values of the depleted width which we obtained from the CV measurements (fig. 4.13b).

4.2.2 Noise measurements under laser illumination

The measurements were performed under the illumination of the CW Millennia laser with the parameters listed in section 2.4 and with the setup described in section 3.2.1 dedicated to the noise measurement. The photo- and dark currents, together with the power of noise at biases from 0 V to biases near to the breakdown voltages were acquired for each type of device. From the currents the gain M (fig. 4.14 (b)) was calculated following equation 3.2. The excess noise factor F was extracted from the

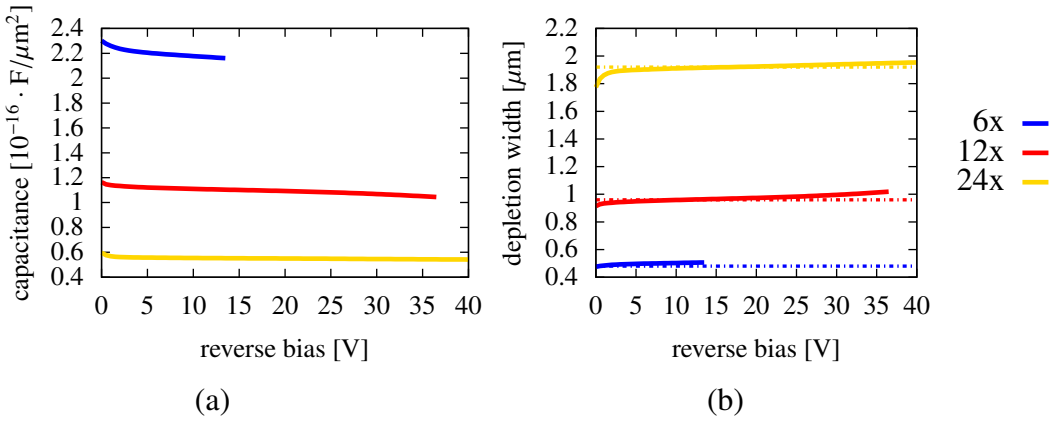

Figure 4.13: Capacitance (a) and corresponding depletion width (b) as a function of a reverse bias for the different devices. The dashed horizontal lines in (b) mark the thickness of the multiplication regions for the three devices.

acquired powers of noise according to the formula 3.4 and the origin of the curves was moved by applying a multiplicative factor so that the excess noise factor is 1 where the gain M is equal to 1 as it must be according to the definition of F. The need of this additional normalization comes probably from the fact that the shot noise is not the only noise which is being amplified by the multiplication process, as we assume in the equation 3.4. One possible additional source of a noise which enters to the multiplication process is the fluctuation of the laser. So far we did not find a way to measure this contribution simultaneously with data acquisition.

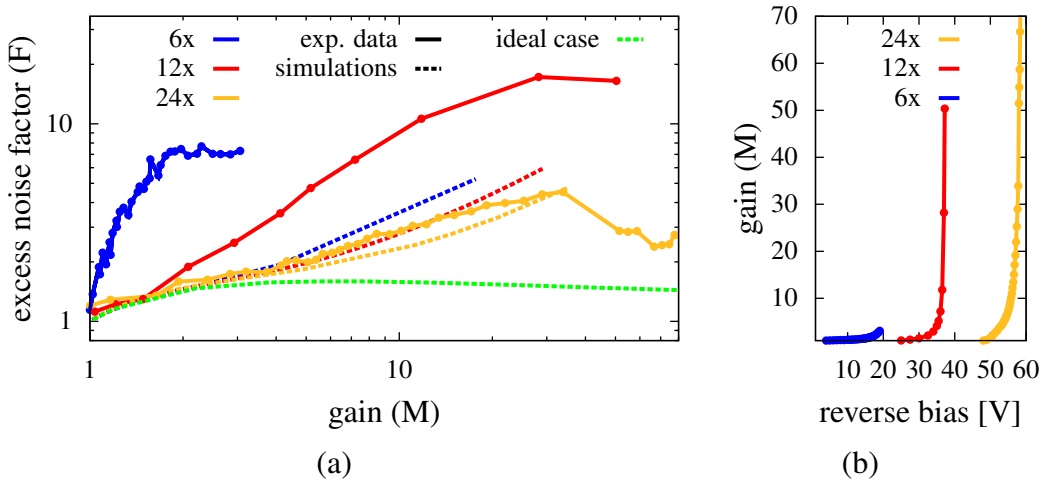

Figure 4.14: (a) excess noise factor calculated from the measured powers of the noise plotted as a function of the gain (solid lines), simulations for the same types of devices (dashed lines with the same colors) and simulation for ideal limit case of a device in which the multiplication of holes is completely suppressed (green dashed line); (b) gains as a function of the reverse bias.

Although the quantitative agreement is poor, with the simulations largely underestimating F especially for the samples with 6 and 12 steps, both experimental data

and simulations confirm that the excess noise factor for a given gain decreases as the number of steps is increased.

The results for the device with 24 steps follow the simulation for gains up to ~ 7. At higher gains F reaches maximum and drops afterwards. This could be related to more efficient suppression of the hole multiplication as the field in the multiplication region increases and the gain grows. In fact, a simulation made for an ideal case where only electrons are multiplied shows an analogous non-monotonic trend (fig. 4.14 green line, [55]). In the case of the device with 12 steps, a less pronounced maxima can be observed as well. In the data acquired on the device with 6 steps we don't observe any maxima suggesting that the regime of significant suppression of hole multiplication is not reached in this type of devices.

4.2.3 Time response

The same set of devices was also compared regarding their time response. The devices were illuminated by the 2nd harmonics ($\lambda = 532\ nm$) of the infrared fiber ytterbium doped laser (specification in section 2.4) and mounted on the setup described in section 3.2.1. For readout the oscilloscope Tektronix was used with an analogue bandwidth of 12.5 GHz and a sampling frequency of 50 GS/s.

The response to the laser pulses was acquired for each device for a set of reverse biases from 0 V to voltages close to the breakdown. We recorded the time response of two devices from each set, as shown in fig. 4.15. From these response curves the rise time was calculated as the time in which the device changes the amplitude of the response from 10 % to 90 % of the maximum. Values of the rise time as function of the reverse bias are plotted in fig. 4.16.

The devices with 6 steps have rise time around 1 ns. The devices with 12 and 24 result to have rise times of 100 ps and 80 ps, respectively. This values are not much higher than the maximal rise time of the oscilloscope which is 28 ps (calculation based on the first order approximation model). This limitation can be higher due to the cables (the U.FL cables have guaranteed reliability upto 6 GHz) and other setup non-idealities. There is also the fact that the values were calculated based on 4 - 5 points laying within the range of 10 % to 90 % of the maximum. For this reasons we conclude that the measurements are on the limit of possibilities of the instrumentation and that the values of rise time for devices with 12 and 24 steps can be considered only as an upper limit of the rise time.

The areas of the responses from fig. 4.15 were integrated for each bias and the gain was calculated by using equation 3.2, but with these integrated areas instead of the currents. The dependence of this gain on the reverse bias is in fig. 4.17. The values of the gain are in qualitative agreement with the one obtained from measurements under

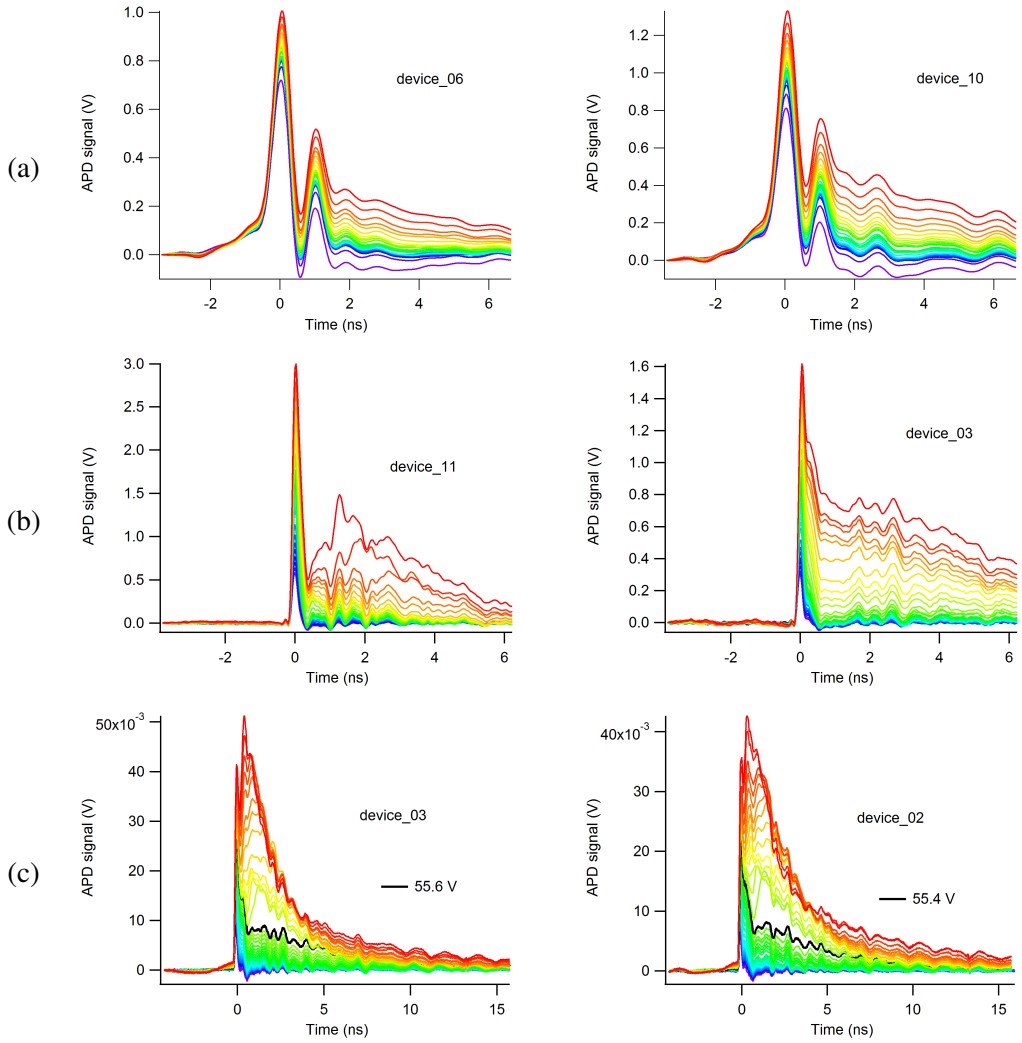

Figure 4.15: Time response of the devices with 6, 12 and 24 steps. Two devices of each kind are shown in panel (a), (b) and (c) respectively. The color scale from violet to red shows increasing reverse bias from 0 V to the voltage near to the breakdown. The black line in the case of the device with 24 steps (c) shows the time response at the bias at which the second broader peak starts to dominate.

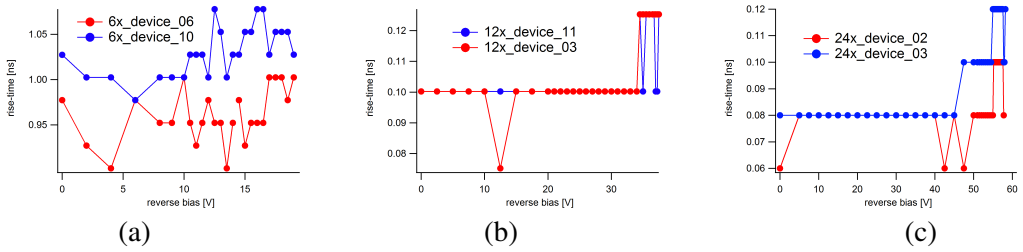

Figure 4.16: Rise times of the devices with 6 (a), 12 (b) and 24 (c) steps as a function of the reverse bias at which the given time response was acquired.

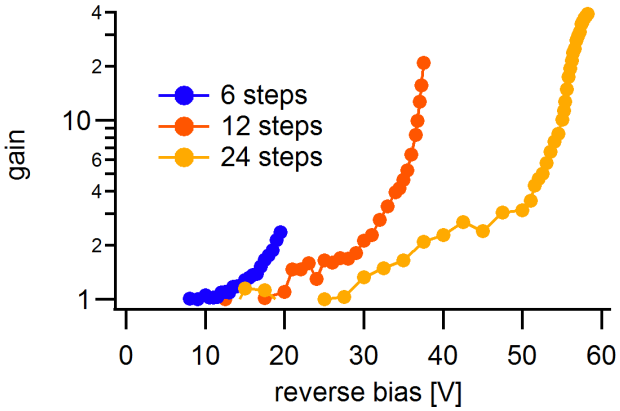

Figure 4.17: The block diagram of the setup for noise measurements.

continuous laser in the sense that with increasing number of the steps in the multiplication region, the maximum gain increases. If we compare the values quantitatively in table 4.2, we can see that the resulting gain from the time response is systematically smaller than the one obtained from measurements under continuous laser. A possible reason for this discrepancy is the worse collection efficiency of electrons generated by the ultra-short laser pulses. In fact, they are generated in a very short time range (10 ps), which makes them also near spatially. This dense bunch of electrons is travelling through the multiplication region where it is multiplied. At some bias the electric field created by this dense bunch of electrons become so significant that it effectively shields the external bias and in this way partially prevents further increase of the multiplication effect.

Table 4.2: Table summarizing the effect of the number of steps in the multiplication layer on device capacitance, on maximal gain obtained under CW illumination, from time response and from spectroscopic measurements, and on the rise time of time response.

# of steps	capacitance [10^{-16}F/μm^2]	max gain CW laser	max gain pulsed laser	max gain QUBE	rise time
6	2.2	3.1 @ 19 V	2.7 @ 19.5 V	4.14 @ 20 V	1 ns
12	1.1	50.4 @ 37.2 V	20.7 @ 37.5 V	11.1 @ 32 V	< 100 ps
24	0.55	92.8 @ 59 V	39.1 @ 58.2 V	34.1 @ 54 V	< 80 ps

4.2.4 Spectroscopic measurements

As it was explained in the section 3.2.1, this experimental setup aims to resolve the K-beta from the K-alpha lines of Fe-55 spectra. For this reason the CUBE - a charge sensitive amplifier (CSA) developed by XGlab for radiation detectors (model PRE 039) was used.

In order to test the setup in well defined conditions a measurements under illumination of the pulsed green table-top laser (pulse width ~ 100 fs, repetition rate 200 kHz, λ = 540 nm) described in section 2.4 were carried out. This source was selected for the possibility to emulate an X-ray single photon source and to adjust the amount of deposited energy and created charge carriers by setting the power of the laser. In such setup it is also possible to use an external trigger obtained by diverging part of the laser beam to a comertial silicon based photodiode. The other, already mentioned advantage, is the fact that photons of this wavelength are absorbed within few hundreds of nanometres in the absorption layer, so no effects of absorption in the deeper layers of the device are present, unlike in the case of Fe-55 source.

The incident power of the laser during this measurements was 28 µW. The response of each type of device (with 6, 12 and 24 steps) to this ultra-short pulses was measured at several biases. Five hundreds single responses for each reverse bias voltage were collected. The area below the curve of this single response is proportional to the charge deposited by a single event (in this case a single pulse). The histogram of the areas calculated from the five hundreds single responses for each reverse bias is plotted in fig 4.18.

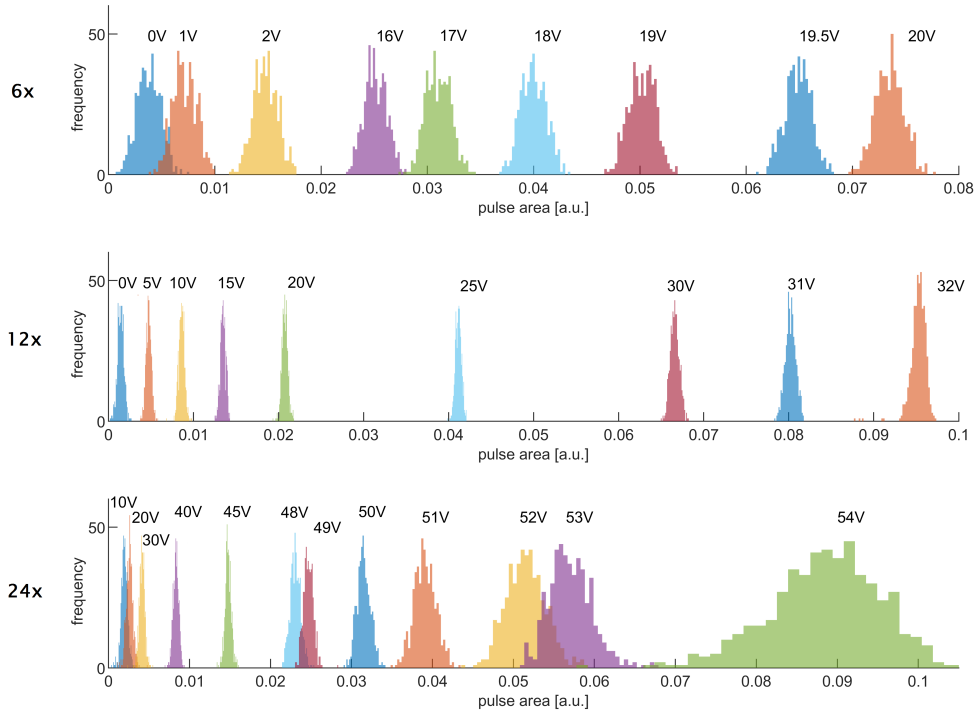

Figure 4.18: Histogram of the areas under the response curves of the CUBE setup for each type of investigated devices. For each reverse bias 500 responses were recorded.

For each distribution of the pulse area at a given reverse bias the mean value was

calculated. From the mean values the gain M as a function of reverse bias voltage was calculated (fig. 4.19a) using the mean value of the area below the response curve instead of current. The unity gain was set at the reverse bias voltage at which the dependence of the area on the reverse bias saturated, the full charge collection regime was reached, but the multiplication did not start yet.

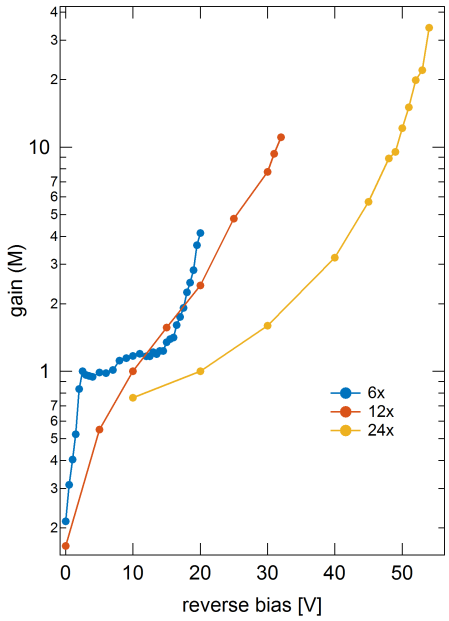

Figure 4.19: Gain as a function of reverse bias of the devices with 6, 12 and 24 steps in the multiplication region derived from the histograms of response areas acquired by CUBE.

The gain M increases with the number of steps. This trend is in agreement with the results obtained from two previous types of measurements (sections 4.2.2 and 4.2.3). The maximal values of gain measured by the setup for the spectroscopic measurements are compared with such previous values in table 4.2.

4.3 Response to hard X-ray

To assess the response to high-energy photons, the devices with 12 steps in the multiplication region and δ p-doped separation layer with dopant concentration 2.5×10^{12} cm^{-2} were tested under irradiation with hard X-rays generated by the XRD2 wiggler beamline at the Elettra Syncrotron in Trieste described in section 2.4.2. Photons of energy 12.4 keV with a maximum flux of 1.7×10^{13} ph·s^{-1} over an area of 300 µm × 90 µm were available for the measurements. The devices were mounted in the UHV chamber which is described in section 3.2.2.

Owing to the incorporated perpendicular movement stages it was possible to perform remotely controlled spatial mesh scans of the devices through the beam. The

beam-size was for this purpose reduced to 100 µm × 900 µm and a typical photon flux was of the order of 10^{12} ph · s^{-1}. The scans were acquired with a step of 30 µm. Two of these maps acquired under different reversed bias voltages are shown in fig 4.20. The area of lower efficiency (bottom left of the circular mesa) is caused by the absorption of the wire bond. Such photocurrent maps were used to align the center of the device with the incident radiation to record position-invariant measurements of the photocurrent. These were carried out by using an oscilloscope (KEYSIGHT DSOS404A) with a 4 GHz analogue bandwidth, a sample rate of 20 GSa·s^{-1} and a 10-bit resolution. In order to avoid radiation damage to the device, the power provided by the synchrotron beamline was kept on values at least one order of magnitude lower than the powers used at the experiments with laser sources described above.

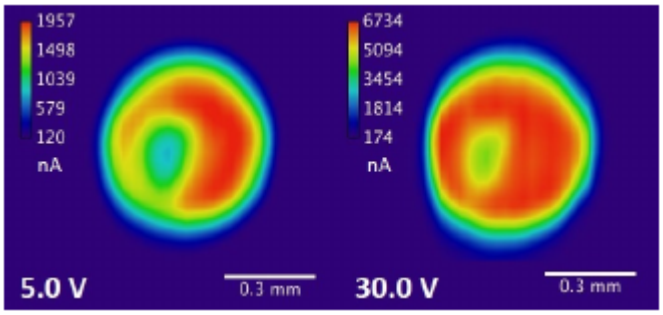

Figure 4.20: XY scans performed in air, with a hard X-ray source (12.4 keV) and with two different reverse bias voltages.

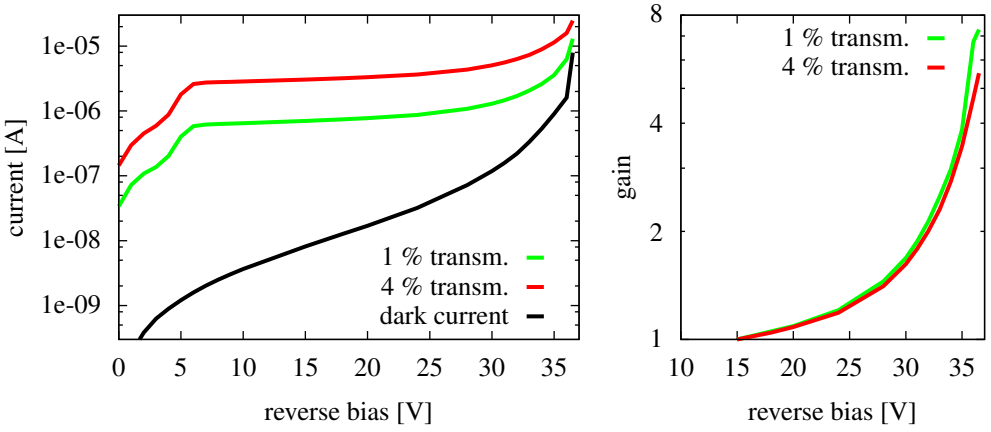

(a) (b)

Figure 4.21: Measurements performed in the air with a hard X-ray beam provided by the XRD2 beamline : black line, dark condition; green line, 1% of transmitted beam through an Al filter; red line, transmission 4%. (a) measured current; (b) gain calculated according to eq. 3.2.

Figure 4.21a reports both the dark current and the photocurrent measured under illumination with different photon fluxes, which were controlled by means of aluminium absorbers. In figure 4.21b reports the gain calculated from these photocurrents and

dark current according to the formula 3.2. As expected, the gain is independent of the particular incident photon flux. However, under illumination with 12.4 keV photons and at 36.5 V of reverse bias, the gain is only 7.3. The fact that this value is smaller compare to all other results from tests under the laser illumination can be due to much higher energy of photons used in this experiment. As opposed to the case of photons of the laser of energy 2.3 eV which are absorbed in few first nanometres of absorption region, photons of energy 12.4 keV can with high probability be absorbed also in the multiplication region. The charge carriers created in the multiplication region don't go through entire multiplication region and can not therefore multiply so effectively. Taking into account that the transition of the absorption region (4.5 μm of GaAs) is 70 % [23], we expect only up to 30% of 12.4 keV photons to multiply with maximum gain.

Conclusions

This project was driven by the necessity of the synchrotron radiation community to reduce the continuously widening mismatch between the ability of new generation light sources to develop high energetic, high brilliance radiation and the relatively modest ability of available detectors to record results of experiments where such sources are used. The aim was to develop fast and sensitive detector for X-ray radiation of energies where the existing commercial silicon detectors cannot provide the required performances, mainly due to intrinsic limits of the material. The choice was to employ GaAs/AlGaAs material to develop such detectors. The material of choice was the GaAs/AlGaAs system. The higher atomic number of GaAs elements compared to Si results in a higher absorption cross-section which offers the possibility of employing thinner absorption regions, which in turn results in faster devices. One additional benefit is the possibility to tailor the material properties by changing the composition x in $Al_xGa_{1-x}As$ alloys. In contrast to the GaAs-based pixelated detectors which are already commercially available, our devices have a fine inner structure in the multiplication region. Such band gap engineering is needed in order to overcome the intrinsically high noise characteristics of GaAs due to the similarity of electron and hole impact ionization coefficients. By taking advantage of the possibility to change the $Al_xGa_{1-x}As$ composition, a band gap modulation is realized under the form of a staircase structure under an external reverse bias. In this way, multiplication of electrons is promoted while multiplication of holes is suppressed resulting in remarkably higher signal to noise ratio. To make the multiplication process even better defined, hence less noisy, a p-doped layer is introduced between absorption and multiplication regions. In this way the first part is shielded from the strong electric field under reverse bias and most of the potential drop happens in the multiplication region.

During the first year we developed a technology platform to fabricate and test a device prototype that allowed us to benchmark our procedures against the state of the art. This induced optimization of the growth/fabrication process of the device and development of experimental setups for detector test. After reaching these benchmarks, we focused on fine tuning of some of the features of the epitaxial layer system which could affect the detector performance.

First, we studied the influence of the p-doped layer separating absorption and multiplication regions on the APD electrical characteristics and their response to light.

Six SAM-APD samples with different p-doping level in the separation layer were fabricated. For five samples with doping up to $2.5 \times 10^{12}\,cm^{-2}$ the separation layer was realized in the form of δ p-doped layer. In order to increase the doping above such value, a thin (50 nm in our case) GaAs:C layer is needed, instead of the δ doping. This

doping scheme was employed to grow the sixth sample with doping $6 \times 10^{12}\,\mathrm{cm}^{-2}$.

First, a characterization in dark was carried out and the influence of the p-doped separation layer on the CV curves was investigated. An acceptor density of $2.5 \cdot 10^{12}\,\mathrm{cm}^{-2}$ was found to be necessary to keep the absorption region with a small enough electric field over the whole range of reverse biases, up to the breakdown voltage. For the devices with a lower doping level, a drop in capacitance occurred at specific voltages within the measured range. Such voltage was found to decrease with decreasing doping levels. TCAD simulations are able to reproduce the measured CV curves for doping densities very close to the experimental ones. The analysis of simulated potential profiles confirms the interpretation above, thus indicating the device with the highest doping is the best suited for applications as a radiation detector.

The photoresponse of the devices was measured by utilizing light sources with energies low enough to ensure that the photogeneration occurs entirely within the first few 100 nm of the absorption region. It was noticed that for low doping levels the multiplication of generated charges is rather low (up to a gain of 2). On the other hand, when the doping level is $2.5 \times 10^{12}\,\mathrm{cm}^{-2}$ or more, we observe a multiplication at reverse biases up to the break down voltage. A virtual absence of gain for lower doping levels is due to the failure to establish an adequate potential in the staircase region that would lead to electron multiplication. Therefore doping at least $2.5 \times 10^{12}\,\mathrm{cm}^{-2}$ is necessary to confine the potential drop mainly in the multiplication region. Further analysis reveals that with $2.5 \times 10^{12}\,\mathrm{cm}^{-2}$ doping the depleted region extends slightly beyond the p layer for the highest applied biases, thus creating a residual field in the absorption region. For the doping $6 \times 10^{12}\,\mathrm{cm}^{-2}$, the measurements show that the potential drop is confined strictly in the multiplication region and the residual field is negligible, if any. This field seems to be beneficial for the collection efficiency of the devices as shown by comparing the absolute values of the photocurrent, while it does not influence significantly the multiplication process. Moreover, the higher concentration of dopant in the p-doped separation layer could result in being an obstacle for the electrons which are less likely to reach the multiplication region.

After the optimal p-doping concentration in the separation layer was found, we studied the influence of the number of steps in the multiplication region of the APD on the detector characteristics. Three samples with 6, 12 and 24 steps were fabricated and tested first in the dark. The measured capacitances, which are compared in table 4.2), confirm the establishment of the whole potential drop in the multiplication region. Noise characteristics and time response were assessed for the tree samples, together with preliminary spectroscopic measurements. The gains extracted from these different types of experiments and under different light sources are compared in table 4.2. In all the three cases , as predicted by simulations, the maximum gains increases with increasing number of steps. Time response experiments showed that the rise

time decrease with increasing number of steps, and in devices with 12 and 24 steps they are faster than 100 and 80 ps, respectively. For more accurate measurements an oscilloscope with higher analogue bandwidth and better sampling frequency is needed.

Last but not least, the devices with 12 steps in the multiplication region and δ p-doped separation layer were tested under irradiation with hard X-rays. A multiplication process for reverse biases near to break down voltage was observed in this photon energy range too, however, the measured gain was smaller than the one obtained in the tests under laser and soft X rays. This is likely due to the fact that the transmission of the 4.5 μm thick absorption region for this energy is about 70 %, thus the charge generation occurs with high probability in the multiplication region too and this leads to significantly a less efficient multiplication.

Bibliography

[1] Baron A., Kishimoto S., Morsec J., and Rigalc J.M. Silicon avalanche photodiodes for direct detection of x-rays. *J. Synchr. Rad.*, pages 131–142, 2006.

[2] Kishimoto S., Yonemura H., Adachi S., Shimazaki S., Ikeno M., Saito M., Taniguchi T., and Tanaka M. A fast x-ray detector using silicon avalanche photodiodes of 64-pixel linear array. *Journal of Physics: Conference Series*, 425(6):062007, 2013.

[3] *Ultrafast XUV*, 2020. `https://www.clf.stfc.ac.uk/Pages/ar11-12_full_hpl_ultrafast_xuv.pdf`.

[4] J. Ullrich. *Ultrafast Dynamics: Pump - Probe Experiments at Free Electron Lasers*, 2020. `http://www.elettra.eu/vFAMC/uploads/Main/Ullrich.pdf`.

[5] Kovalev S., Green B., and Golz T. et al. Probing ultra-fast processes with high dynamic range at 4th-generation light sources: Arrival time and intensity binning at unprecedented repetition rates. *Structural Dynamics*, page 024301, 2017.

[6] Stefan P. Hau-Riege, Sébastien Boutet, Anton Barty, Sa ša Bajt, Michael J. Bogan, Matthias Frank, Jakob Andreasson, Bianca Iwan, M. Marvin Seibert, Janos Hajdu, Anne Sakdinawat, Joachim Schulz, Rolf Treusch, and Henry N. Chapman. Sacrificial tamper slows down sample explosion in flash diffraction experiments. *Phys. Rev. Lett.*, 104:064801, Feb 2010.

[7] A. Thompson, D. Mills, S. Naday, J. Hormes, S. Gruner, P. Siddons, J. Arthur, R. Wehlitz, and H. Padmore. A program in detector development for the us synchrotron radiation community. Technical report, A white paper based on a workshop held in Washington DC, Oct. 30 – 31st 2000.

[8] DESY. 2017. `http://photon-science.desy.de/research/technical_groups/detectors/`.

[9] Kouhei Nakanishi, Kanako Kodani, Jung Yeol Yeom, and Seiichi Yamamoto. Estimation of optimum scintillator thickness of si-pm detectors for time-of-flight (tof)-pet. *Biomedical Physics & Engineering Express*, 3(2):027002, 2017.

[10] A.Peacock A.Owens. Compound semiconductor radiation detectors. *Nucl. Instrum. Meth. Phys. Res.*, pages 18 – 100, 2004.

[11] G.F. Williams F. Capasso, W.T. Tsang. Staircase solid-state photomultipliers and avalanche photodiodes with enhanced ionization rates ration. *IEEE T. Electron Dev.*, pages 381 – 390, 1983.

[12] J. Ng G. Lioliou, X. Meng and A.M. Barnett. Characterization of gallium arsenide x-ray mesa p-i-n photodiodes at room temperature. *Nucl. Instr. and Meth. A*, pages 813:1–9, 2016.

[13] J. Lauter, D. Protić, A. Förster, and H. Lüth. AlGaAs/GaAs sam-avalanche photodiode: An X-ray detector for low energy photons. *Nucl. Instrum. Meth. Phys. Res.*, pages 324–329, 1995.

[14] S. Kishimoto. Si-apd array detectors with 2 ns pulse-pair resolving time and sub-ns resolution for synchrotron x-ray measurements. *Nucl. Instrum. Meth. Phys. Res.*, pages 98 – 100, 2011.

[15] F. Capasso. Physics of avalanche photodiodes. In W. T. Tsang, editor, *Semiconductors and semmetals, part D; Photodetectors*, chapter 1, pages 2–168. Academic press, inc., 1985.

[16] R. J. McIntyre. Multiplication noise in uniform avalanche diodes. *IEEE Transactions on Electron Devices*, ED-13(1):164–168, Jan 1966.

[17] R. J. McIntyre. A new look at impact ionization-part i: A theory of gain, noise, breakdown probability, and frequency response. *IEEE Transactions on Electron Devices*, 46(8):1623–1631, 1999.

[18] W. Feller. On probability problems in the theory of counters. *Springer, Switzerland*, 1948:105 – 115, 2015.

[19] R.D. Evans. *The Atomic Nucleus*. McGraw-Hill, New York, 1955.

[20] Shoaib Usman and Amol Patil. Radiation detector deadtime and pile up: A review of the status of science. *Nuclear Engineering and Technology*, 50(7):1006 – 1016, 2018.

[21] C. Jacoboni, C. Canali, G. Ottaviani, and A. Alberigi Quaranta. A review of some charge transport properties of silicon. *Solid-State Electronics*, 20(2):77 – 89, 1977.

[22] G F. Knoll. *Radiation Detection and Measurement*. 01 2000.

[23] The center for X-ray optics. *X-ray database*, 2019. `http://cxro.lbl.gov/`.

[24] F. Capasso, W. J. Tsang, A. L. Hutchinson, and G. F. Williams. Enhancement of electron impact ionization in a superlattice: a new avalanche photodiode witha large ionization rates ratio. *Appl. Phys. Lett.*, 40(1):38 – 40, 1982.

[25] R. Chin, N. Holonyak, G. E. Stillman, J. Y. Tang, and K. Hess. Impact ionization in multilayered heterojunction structures. *Electron. Lett.*, 16:467 – 469, 1980.

[26] F. Capasso, W. J. Tsang, A. L. Hutchinson, and P. W. Foy. The graded bandgap avalanche diode: A new molecular beam epitaxial structure with a large ionization rates ratio. *in Proc. 1981 Symp. on GaAs and Related Compounds, Inst. Phys. Conf. Ser. 63*, pages 473 – 478, 1982.

[27] J. Lauter, A. Foerster, H. Lueth, K.D. Mueller, and R. Reinartz. Algaas/gaas avalanche detector array -1 gbit/s x-ray receiver for timing measurements. 1996.

[28] Herman M. A. and Sitter H. *Molecular beam epitaxy*. Springer-Verlag, 1996.

[29] Foxon C.T. and Joyce B.A. Interaction kinetics of As4 and Ga on 100 GaAs surfaces using a modulated molecular beam technique. *Surf. Science*, 50(2):434–450, 1975.

[30] Foxon C.T. and Joyce B.A. Interaction kinetics of As2 and Ga on 100 GaAs surfaces. *Surf. Scie*, 64(1):293–304, 1977.

[31] Marc J Madou. *Fundamentals of microfabrication: the science of miniturization*. CRC Press, 2nd ed edition, 2007.

[32] U. Kreibig and M. Vollmer. Optical properties of metal clusters. *Springer*, 1995.

[33] Keysight technologies. Data sheet b1500a semiconductor device analyzer, 2019.

[34] E. D. Palik. *In Handbook of Optical Constants of Solids*. Academic Press, Burlington, 1997.

[35] Spectra Physics. *Millennia V*, 2019. https://loci.wisc.edu/sites/default/files/2016-09/Millennia%20Pro%20s-Series.pdf.

[36] K. Zhukovsky. *Undulators for Short Pulse X-Ray Self-Amplified Spontaneous Emission-Free Electron Lasers*, 2019. https://www.intechopen.com/books/high-energy-and-short-pulse-lasers/undulators-for-short-pulse-x-ray-self-amplified-spontaneous\-emission-free-electron-lasers.

[37] DESY, Hamburk, Germany. *How does a synchrotron radiation source work?*, 2019. http://photon-science.desy.de/research/students__teaching/primers/synchrotron_radiation/index_eng.html.

[38] BEAR beamline Elettra synchrotrone Trieste. *BEAR - Beamline Description* , 2019. http://www.elettra.eu/lightsources/elettra/elettra-beamlines/bear/beamline-description/all.html.

[39] Elettra – Sincrotrone Trieste S.C.p.A. Xrd1, 2019.

[40] XRD2 beamline Elettra synchrotrone Trieste. *XRD2 Specifications*, 2019. http://www.elettra.eu/lightsources/elettra/elettra-beamlines/xrd2/xrd2-specifications/all.html.

[41] C. Rauch, G. Strasser, M. Kast, and E. Gornik. Mean free path of ballistic electrons in gaas/algaas superlattices. *Superlattices and Microstructures*, 25(1):47 – 51, 1999.

[42] D. L. Sato, F. J. Szalkowski, and H. P. Lee. The theory of a general quantum system interacting with a linear dissipative system. *Appl. Phys. Lett. 66*, page 1791, 1995.

[43] IOM-CNR, Trieste, Italy. *FNF*, 2019. https://fnf.iom.cnr.it/.

[44] Masanori Murakami. Development of refractory ohmic contact materials for gallium arsenide compound semiconductors. *Science and Technology of Advanced Materials*, 3(1):1–27, 2002.

[45] Anna Baranska, Anna Szerling, Piotr Karbownik, K Hejduk, Maciej Bugajski, A Laszcz, Krystyna Gołaszewska-Malec, and Wojciech Filipowski. Ohmic contacts for room-temperature algaas/gaas quantum cascade lasers (qcl). *Optica Applicata*, 43:5–15, 01 2013.

[46] Giuseppe Bertuccio and Diego Maiocchi. Electron-hole pair generation energy in gallium arsenide by x and photons. *Journal of Applied Physics*, 92:1248–1255, 08 2002.

[47] XGlab - BRUKER. *CUBE - Charge Sensitive Preamplifier for Radiation Detectors*, 2019. https://www.xglab.it/UserFiles/fly_xgc_cube_2p_en_lores.pdf.

[48] Synopsys, sentaurus^{TM}. *Device User Guide*, March, 2016.

[49] T. Steinhartova, C. Nichetti, M. Antonelli, G. Cautero, R.H. Menk, A. Pilotto, F. Driussi, P. Palestri, L. Selmi, K. Koshmak, S. Nannarone, F. Arfelli, S. Dal Zilio, and G. Biasiol. Influence of p-doping on the behaviour of AlGaAs/GaAs SAM-APDs for synchrotron radiation. *J. Instrum.*, 12:C11017, 2017.

[50] A. Pilotto, P. Palestri, L. Selmi, M. Antonelli, F. Arfelli, G. Biasiol, G. Cautero, F. Driussi, R. H. Menk, C. Nichetti, and T. Steinhartova. An improved random path length algorithm for p-i-n and staircase avalanche photodiodes. pages 26–30, 2018.

[51] E. H. Hwang and S. Das Sarma. "limit to two-dimensional mobility in modulation-doped gaas quantum structures: How to achieve a mobility of 100 million". *"Phys. Rev. B"*, 77, 2008.

[52] D.W. Winston. Physical simulation of optoelectronic semiconductor devices. *UCB*, 1996.

[53] S.M Sze. *Physics of Semiconductor Devices*. John Wiley & Sons, 1981.

[54] C. Nichetti, T. Steinhartova, M. Antonelli, G. Cautero, R.H. Menk, A. Pilotto, F. Driussi, P. Palestri, L. Selmi, K. Koshmak, S. Nannarone, F. Arfelli, S. Dal Zilio, and G. Biasiol. Gain and noise in AlGaAs/GaA avalanche photodiodes with thin multiplication regions. *J. Instrum.*, 12:C11017, 2018.

[55] A. Pilotto, P. Palestri, L. Selmi, M. Antonelli, F. Arfelli, G. Biasiol, G. Cautero, F. Driussi, R. H. Menk, C. Nichetti, and T. Steinhartova. A new expression for the gain-noise relation of single-carrier avalanche photodiodes with arbitrary staircase multiplication regions. *IEEE Transactions on Electron Devices*, 66(4):1810–1814, 2019.